Fabian Clemens Huber, BSc.

Thermal Transport in Microelectronics Packaging - An Approach of Inverse Modeling of Materials Parameters

MASTER'S THESIS

to achieve the university degree of

Diplom-Ingenieur

Master's degree programme: Technical Physics

submitted to

Graz University of Technology

Supervisor

Univ.-Prof. Ph.D. Peter Hadley

Institute of Solid State Physics

in cooperation with ams AG, 8141 Premstätten

Graz, September, 2016

AFFIDAVIT

I declare that I have authored this thesis independently, that I have not used other than the declared sources/resources, and that I have explicitly indicated all material which has been quoted either literally or by content from the sources used. The text document uploaded to TUGRAZonline is identical to the present master‘s thesis.

Date

Signature

Acknowledgements

This work would not have been possible without the aid of many people. I want to thank all of them, who helped me with their support.
Particularly I want to thank Peter Hadley, who shared his great attitude and advice. I deeply apprechiate his commitment and his open ear for ideas and concerns. I owe great thanks to Harald Etschmaier and Anderson Singulani for their guidance, for sharing their sparse time for inspiring discussions and for their great support. I want to express my gratitude to Rainer Minixhofer for making all this work possible and for his great encouragement.
I most warmly thank my friends and colleagues of ams AG. Especially Archim Wolfberger, Sonja König, Markus Weber, Elodie Le-Paih, Raffaele Coppeta, Andreas Wagner, Patrick Frieszer, Gilbert Promitzer, Peter Bliem, Federico Donati, Marco Cerchi, Martin Agu, Gerald Bogner and Martin Stermitz for their help in so many various matters.
Thanks also to Günther Leising, for providing me with his experience in temperature measurements and his equipment, as well as Natalia Bedoya, Anna Coclite, Harald Kerschbaumer and the members of the Institute of Solid State Physics.
Of course I especially want to thank my parents, my sister and my brother, who are always behind me, throughout my life.
Finally, I want to acknowledge the opportunity that ams AG offered me, to investigate this interesting topic in this very prolific environment at Premstätten.

Contents

1 Outline and Motivation 1

2 Microelectronics Packaging 2
2.1 Process Flow . . . 2
2.1.1 Die Attach . . . 2
2.1.2 Wire Bonding . . . 2
2.1.3 Encapsulation . . . 3

3 Heat Transfer Mechanisms 4
3.1 Radiation and Convection . . . 4
3.2 The Influence of Natural Convection . . . 4
3.3 Thermal Conduction . . . 6
3.3.1 Electronic Thermal Conductivity . . . 7
3.3.2 Phonon Thermal Conductivity . . . 8
3.3.3 Scattering Processes . . . 9
3.3.4 N- and U- Processes . . . 11
3.3.5 Thermal Interface Resistance . . . 13
3.3.6 Thermal Conduction in Semiconductors . . . 16
3.3.7 Thermal Conduction in Polymers . . . 17
3.3.8 Thermal Conduction in Adhesives . . . 18
3.3.9 The Heat Equation . . . 19

4 Finite Elements Simulations 20
4.1 Galerkin's Method . . . 20
4.2 Time Dependent Simulations . . . 21
4.2.1 The Backward Differentiation Formula . . . 22

5 Experimental Setup 23
5.1 Devices Under Test . . . 23
5.2 Measurement Environment . . . 24
5.2.1 Ambiance Conditions . . . 24
5.2.2 Device Preparation . . . 26
5.2.3 Infrared Camera Setup . . . 27
5.2.4 ESD Diode Measurements . . . 28
5.3 Heating Configurations . . . 28

6 Simulation Setup 31
6.1 CAD Models . . . 31
6.2 Simulation Assumptions . . . 33

7 Design of Experiment 34
7.1 Response Surface Design . . . 34

8 Results **36**
8.1 Measurement Results . . . 36
8.2 Emissivity Adjustment . . . 38
8.3 Adjustment of Thermal Conductivity . . . 39
8.3.1 Set Materials Parameters . . . 40
8.3.2 Parameter Estimation . . . 41
8.4 Adjustment of Specific Heat . . . 45
8.5 Model Adaption . . . 46
8.6 Natural Convection Considerations . . . 52
8.6.1 Vacuum Measurements . . . 53
8.6.2 Foam Embedded Device . . . 54
8.7 The Influence of Thin Films on Top of the Die Surface . . . 55
8.8 Temperature Evolution and Heat Paths . . . 56

9 Outlook **63**
9.1 Raman Measurements . . . 63
9.2 Transient Measurements . . . 65
9.3 Computational Fluid Dynamics Simulations . . . 68
9.4 Measurement Concepts . . . 68
9.5 Thermal Property Measurements . . . 68
9.6 Thermal Interface Resistances . . . 68

10 Conclusion **69**

11 Appendix **70**
11.1 Temperature Dependent Thermal Properties . . . 70
11.2 Transient Response MatLab Code . . . 71
11.3 Keithley®, Vötsch® TCP/IP Communication . . . 75

List of Figures

1 (a) SEM image of bonding wires on a dummy die surface. (b) Conducting die attach with Ag-particles. . . . 3
2 Transfer molding process [4] . . . 3
3 (a) Scattering contributions to the electronic thermal conductivity κ_e (after [7]). (b) Electrical conductivity and electronic thermal conductivity calculated using the Wiedemann-Franz law [14, 15]. . . . 10
4 Umklapp scattering. The sum of the two momenta crosses the Brillioun zone and the added reciprocal lattice vector changes the direction of the final wavevector (after [8]). . . . 11
5 Main scattering contributions to the lattice thermal conductivity (after [8]). . . . 12
6 (a) Phonon dispersion of silicon [19]. Scattering of two longitudinal acoustic phonons k_1 yields a longitudinal optical phonon k_3 with reversed group velocity, (b) phonon scattering in a linear dispersion with longitudinal and transverse acoustic branches within the Brillouin zone flips the direction of the heat flux [19]. 13
7 SEM image of silica filler particles embedded in a resin matrix. . . . 16
8 Phase transitions of amorphous polymers (after [28]). . . . 17
9 Temperature dependence of the thermal conductivity of amorphous polymers (after [28]). . . . 18
10 Ag-particles forming a conducting path through the adhesive epoxy (after [29]). . 19
11 Linear ("rooftop") basis functions with unit magnitude at the nodal points and linearly decreasing to vanish at the neighboring nodes. . . . 20
12 (a) Drawing of the AS5171 SiP (System in Package) package, (b) open package, die surface, and bonding wires. . . . 23
13 (a) Top view onto the OLGA package mounted onto a PCB, (b) top view onto the clear mold compound of the device. . . . 23
14 Vötsch® VT 4002 climate chamber used to control ambiance conditions. . . . 24
15 Temperature development inside the climate chamber, 4 cm above the DUT surface. 25
16 (a) Vötsch® internal temperature sensor temperatures in comparison to Pt100 temperature measurement after settlement time of at least 20 minutes, (b) temperature characteristic of a Pt100 class A resistor. . . . 25
17 Measurement construction for the SiP package. (a) Top view, (b) side view. . . . 26
18 Measurement construction for the OLGA package. (a) Top view: the small rectangular package in the middle soldered onto a printed circuit board, (b) side view . . . 27
19 optris® PI 160 infrared camera mounted above the devices inside the climate chamber. . . . 27
20 Measured U-T characteristic of (a) the ESD protection diodes of the SiP package and (b) the BJT temperature sensor of the OLGA package. The voltages are averaged over 5 runs. . . . 28

21 Positions of the heated ESD diodes at the interface between wire bond and die (blue). The location of the temperature sensor is marked in red. (a) OLGA package. (b) SiP package. 29
22 Power dissipation configurations of (a,b) 1 diode heating, (c,d) 2 diode heating, (e,f) 3 diode heating. For the OLGA package (left column) and for the SiP package (right column). 30
23 (a) Light microscope picture of the cross section of a cut device and (b) corresponding view of the CAD model of the OLGA package. 31
24 CAD model of the OLGA package. (a) The device mounted onto a printed circuit board (red) and connected by pins and wires. (b) The substrate (blue) and the die (gray). 32
25 Modeled substrate structure of the OLGA package. 32
26 (a) Light microscope picture of the cross section of a cut device and (b) corresponding view of the CAD model of the SiP package. 32
27 CAD model of the SiP package. (a) The device (violet) is attached onto a FR4 construction (red). A ribbon cable is soldered onto the leads (yellow). (b) The lead frame (yellow) and the die (gray) are connected by wire bonds. 33
28 (a) Central composite design (b) Box-Behnken design for a three dimensional parameter space. The cube's edge is the parameter range and the red dots mark the parameters for experimental runs. 34
29 Simulation loop to narrow down parameter ranges. 35
30 Temperature evolution for three different heat configurations: heating of one ESD diode (blue), two diodes (red) and three diodes (orange). The temperature was measured at the BJT temperature sensor. 36
31 Temperature evolution for three different heat configurations: heating of one ESD diode (blue), two diodes (red) and three diodes (orange). The temperature was measured also at an ESD diode. 36
32 Thermal impedance of the OLGA package. 37
33 Thermal impedance of the SiP package. 37
34 Emissivity estimation using attached NiCr-Ni thermocouples and an infrared camera. Top row: SiP package, Bottom row: OLGA package 38
35 Thermocouple-, black body- and emissivity adjusted surface temperature (a) of the SiP package and (b) of the OLGA package 39
36 Influence of radiative lid surface on simulation results of OLGA package 39
37 OLGA Package: Influence and parameter range estimation of thermal conductivity of materials under investigation. 41
38 SiP Package: Influence and parameter range estimation of thermal conductivity of materials under investigation. 42
39 Two dimensional projections of the three dimensional response surface. Demonstrative example with 3 diodes and 333 mW overall heat dissipation. Left column: first run. Right column: second run for finer adjustment. 44
40 Response of the SiP package to changes in the thermal conductivity of the mold compound. The arrow indicates the error. 45

41 Measured temperature evolution curve and specific heat sweep curves for the OLGA package (a) and for the SiP package (b) 46
42 The comparison factor of the specific heat of the OLGA package (substrate, clear mold, lid cap) (a) and of the SiP mold compound (b) do not show a minimum in a reasonable range. 46
43 Adapted model of the OLGA package construction. 47
44 Two dimensional projections of the three dimensional response surface. Demonstrative example with 3 diodes and 333 mW overall heat dissipation. Left column: first run. Middle column: second run. Right column: third run. 48
45 Response of the SiP package to changes in the thermal conductivity of the mold compound. Including anisotropic thermal condcutivity of FR4. The arrow indicates the error. 49
46 OLGA package: Comparison of measurement and simulation for the one, two, and three diode configuration. 49
47 SiP package: Comparison of measurement and simulation for the one, two, and three diode configuration. 50
48 Measured surface temperatures and simulation results. 50
49 SEM picture of the substrate of the OLGA package. 51
50 Measured temperature evolution curve and specific heat sweep curves for the adapted model of the OLGA package (a) and for the SiP package (b). Both models with an anisotropic thermal conductivity of FR4. 51
51 (a) The comparison factor for the specific heat of the OLGA package (substrate, clear mold compound, lid cap), for the three diode configuration, does not show a minimum in a reasonable range. (b) The comparison factors of the specific heat of the mold compound of the SiP package show a minimum close to the initial supplier value, consistent for three different heating configurations (one, two, and three diode heating). 52
52 Simulations including simplified horizontal plate and vertical wall natural convection boundary conditions. (a) OLGA package, (b) SiP package. 53
53 (a) The SiP device contacted inside a SEM vacuum chamber. (b) The three diode heat configuration with evacuated and vent chamber. 53
54 The devices were embedded in polyurethane foam to exclude the effect of natural convection. 54
55 Comparison of the heat up characteristics embedded in polyurethane foam and at ambient air. (a) OLGA package, (b) SiP package. 54
56 Device structure between die and mold compound. (a) OLGA package. (b) SiP package. 55
57 Comparison of simulations with and without passivation and protection layers. (a) OLGA package with and without SiO_2 and Si_3N_4. (b) SiP package with and without SiO_2, Si_3N_4, and polyimide. The inset shows the difference that comes from numerical noise. 56

58 Temperature distribution of a cross section of the OLGA device (a) after 10 ms, (c) after 1 s, (e) in steady state. Heat flux (b) after 10 ms, (d) after 1 s, (f) in steady state. The arrow length is scaled by $4 \cdot 10^{-9}$ and corresponds to the heat flux at the arrow's tail. 57
59 Temperature distribution of the die and lead structure of the OLGA device (a) after 10 ms, (c) after 1 s, (e) in steady state. Heat flux (b) after 10 ms, (d) after 1 s, (f) in steady state. The arrow length is scaled by 10^{-10} and corresponds to the heat flux at the arrow's tail. 58
60 Temperature distribution of a cross section of the SiP device (a) after 10 ms, (c) after 1 s, (e) in steady state. Heat flux (b) after 10 ms (d) after 1 s, (f) in steady state. The arrow length is scaled by $2 \cdot 10^{-8}$ and corresponds to the heat flux at the arrow's tail. 60
61 Temperature distribution of the die and lead structure of the SiP device (a) after 10 ms, (c) after 1 s, (e) in steady state. Heat flux (b) after 10 ms (d) after 1 s, (f) in steady state. The arrow length is scaled by $2 \cdot 10^{-10}$ and corresponds to the heat flux at the arrow's tail. 61
62 Temperature evolution at the die surface of an etched open SiP package. (a) IR measurement, (b) simulation. 62
63 The Raman peak intensity is temperature dependent [49]. 63
64 The anti-Stokes signal of the 1610 cm^{-1} band of the clear mold compound of the OLGA package varies strongly within the material itself. 64
65 The peak intensity of the anti-Stokes signal in the range of 1610 cm^{-1}. 64
66 Anti-Stokes part of the Raman spectra of the clear mold compound and the die attach adhesive of the OLGA package. 65
67 (a) Lumped circuit model (Foster network) of the thermal resistances and heat capacities of a three component system. (b) Equivalent Cauer network, assumed to represent the real heat flow structure. 65
68 Comparison of the time constants fit by a sum of 11 decaying exponentials. One, two, and three diode configuration. (a) OLGA package. (b) SiP package. 66
69 Cooldown transients for the one diode (first row), two diode (second row), and three diode heat configuration (third row). Left column: OLGA package. Right column: SiP package. 67
70 Temperature dependent thermal properties. Specific heat values out of literature and calculated values using SGTE values for the Gibbs energy [52]. (a) Cu thermal conductivity [36] (b) Cu specific heat [37] (c) Au thermal conductivity [35], (d) Au specific heat [35], (e) Si thermal conductivity [36] (f) Si specific heat [38] . . . 70

List of Tables

1 Initial materials parameters of the OLGA package 40
2 Initial materials parameters of the SiP package 41
3 Parameter estimation for the OLGA package. 43
4 Parameter estimation with confined ranges for the OLGA package. 43
5 Parameter estimation for the SiP package. 45
6 Parameter estimation with confined ranges for the adapted model of the OLGA package. 47
7 Parameter estimation with confined ranges for the adapted model of the SiP package. 49

List of Abbreviations

IC	Integrated Circuit
CTE	Coefficient of Thermal Expansion
SEM	Scanning Electron Microscope
CFD	Computational Fluid Dynamics
MEMS	MicroElectroMechanical Systems
AMM	Acoustic Mismatch Model
DMM	Diffusive Mismatch Model
MD	Molecular Dynamics
ALD	Atomic Layer Deposition
FEM	Finite Elements Method
PDE	Partial Differential Equation
FDTD	Finite Difference Time Domain
CPU	Central Processing Unit
BDF	Backwards Differentiation Formula
DUT	Device Under Test
CMOS	Complementary Metal-Oxide Semiconductor
SiP	System in Package
OLGA	Optical Land Grid Array
PCB	Printed Circuit Board
ESD	ElectroStatic Discharge (protection)
JEDEC	Joint Electron Device Engineering Council
TCP/IP	Transmission Control Protocol / Internet Protocol
BMS	Butterfly Measurement System
SMD	Surface Mount Device
FR4	Flame Retardant in compliance with the standard UL94V-0
BJT	Bipolar Junction Transistor
CAD	Computer Aided Design
I/O	Input/Output
LCP	Liquid Crystal Polymer
FFT	Fast Fourier Transform
DSC	Differential Scanning Calorimetry

List of Symbols

P	Power
A	Surface Area
ϵ	Emissivity
σ	Stefan-Boltzmann constant
$\vec{q}$	Heat flux
Q	Heat
h	Convection heat transfer coefficient
T	Temperature
T_S	Surface temperature
T_0	Ambient temperature
$u(x, y)$, $v(x, y)$	x- and y- components of the mass velocity
g	Acceleration due to gravity
ρ	Mass density
μ	Viscosity
α	Thermal diffusivity
κ	Thermal conductivity
c_p, c_v	Specific heat at constant pressure or constant volume
Nu	Nusselt number
Re	Reynolds number
Ra	Rayleigh number
L	Characteristic length
τ	Scattering mean free time
λ	Mean free path
D	Diffusion constant
u	Internal energy
n	Particle density
$\vec{i}$,$\vec{j}$	Electric current density
$D(\vec{k})$	Electron density of states
$D(\vec{K})$	Phonon density of states
$f(\vec{k})$	Electron distribution function
$N(\vec{K})$	Phonon distribution function

f_0	Fermi function
N_0	Bose-Einstein distribution
μ	Chemical potential
$\vec{F}_{ext}$	External force
$\vec{E}$	Electric field
e	elemental charge
κ_e	Electronic thermal conductivity
κ_L	Lattice thermal conductivity
L_0	Lorentz number
S	Seebeck coefficient
ω	Frequency
ω_D	Debye frequency
θ_D	Debye temperature
k_B	Boltzmann constant
ρ_i	Ideal electrical resistance
$1/\kappa_{e,i}$	Ideal electronic thermal resistance
$1/\kappa_{e,0}$	Electronic thermal resistance due to impurity scattering
$\vec{G}$	Reciprocal lattice vector
v_T, v_L	Group velocity of transversal and longitudinal phonon branch
$1/h_{bd}$	Boundary resistance
α	Phonon transmission probability
c_j	Velocity of phonon mode j
σ	Electric conductivity
Π_{mn}	Peltier coefficient
U_R	Molar sound velocity function
T_g	Glass transition temperature
u^e	Approximating function in the FEM method
N^e	Basis function in the FEM method
P_{s-1}	Lagrangian polynomial
Θ_{JA}	Junction-to-ambiance thermal impedance
I_s, I_{as}	Intensity of the Stokes and the anti-Stokes peak
$\tilde{\nu}_0$	Radiated laser frequency in Raman measurements
$\tilde{\nu}_R$	Raman frequency shift

1 Outline and Motivation

Microelectronics production nodes and package sizes are diminishing and power integration is increasing. As a consequence, heat management is becoming an increasingly important topic in packaging technology. The essence of this work is to develop a better understanding of thermal transport in microelectronics packaging. Therefore, I start by giving an overview of the packaging process flow and of theoretic models describing heat transfer in solids. Essential conduction mechanisms are explained with special focus on their temperature dependence.
The availability of precise thermal models is crucial for an optimized system design. But the necessary thermal parameters of the materials used in the industry are often confidential or not known and thus not readily available. The sparse information on materials compositions prohibits calculations of properties like phonon and electron densities of states for calculating thermal impedances or interface resistances or simulations on molecular level (MD).
Time dependent finite element simulations of simplified geometrical models of the packages were performed. I tried to extract the relevant parameters of the simulation by inversely modeling the thermal behavior of two microelectronic packages - one system in package (SiP) and one optical land grid array package (OLGA) - to experimental results. Concepts for heating and temperature measurements inside the package were restricted to electrostatic discharge protection (ESD) diodes and bipolar junction transistors (BJT) embedded in the integrated circuit (IC). Still, for a fundamental understanding of these 3-dimensional systems, temperature sensing approaches on multiple levels (sandwich die structures) would be necessary. In addition, the package surface temperature was measured using an infrared camera. All these measurements were done under controlled conditions in a climate chamber for ambient temperature stabilization.
The obtained results are biased with high inaccuracies due to high sensitivities of materials parameters to small temperature differences. Especially properties of materials that are not part of the main heat paths could not be estimated using a second order response surface design of experiment (DOE). Therefore, the main contributors to heat transport were identified and thermal conductivities were adapted to fit the simulation results to the experiments.
Temperature measurements using ESD-diodes give rise to problems in repeatability and accuracy and are therefore not an optimal concept for thermal characterization of semiconductor devices. Still, their availability all over the die surface makes them an important tool. BJT temperature references are a more suitable approach but require powering of the device and need to be implemented on purpose into the IC. Die surface temperature measurements were done using the implemented BJT sensor in the OLGA package and the most stable ESD diode for the SiP package due to non-negligible and unclear power dissipation across the die, while in test mode, required for the BJT temperature measurement.
Heat transfer in the optimized models was investigated and as an outlook further research concepts using Raman microscopy and time constant spectra are discussed and suggestions for further investigations are given.

2 Microelectronics Packaging

2.1 Process Flow

Packaging of semiconductor devices describes the process steps starting from the readily processed wafer that contains the fully functioning silicon dice (and hence the integrated circuit) to the final device ready for system assembly. For further interest a more detailed explanation of packaging technologies and semiconductor manufacturing processes may be found, for example, in [1] and [2].

2.1.1 Die Attach

After the wafer is diced usually using a diamond saw or a laser (stealth dicing), and all the passives are soldered onto the lead frame or substrate, the die needs to be attached. Therefore, a thermally and mostly also electrically conductive polymeric adhesive is used. Once thermosetting polymers are cured they do not lose their solid state even if exposed to higher temperatures. The most commonly used polymers are epoxy resins which offer high quality at low material cost. Silver flakes are added to the epoxy matrix as a filler to ensure electrical conductivity. Other additives like solvents, catalysts, and hardener are included to modify properties such as processing temperatures, curing times, elastic moduli, moisture absorption, resin bleed, stress, through put, life time, and dispensing quality. If no electrical conductivity is needed, thermally conductive fillers are used. The adhesive is typically characterized by its glass transition temperature, thixotropic index, ionic purity and coefficient of thermal expansion (CTE). The latter is important to buffer stress, which might occur due to CTE mismatch between the die and the lead frame or substrate.

2.1.2 Wire Bonding

The method of front side connection, that is important for the devices in this work, is wire bonding. The pads on top of the die need to be connected to the lead frame or substrate. Therefore, the bonder attaches a metal ball onto the die through a capillary and loops a fine wire to the lead and joins it. The ball is attached to the pad by thermosonic ($\sim 150°$C) or ultrasonic bonding (room temperature) where the capillary pushes the ball onto the pad and creates the intermetallic compound by friction. Then, the wire is looped to meet the package requirements like loop height, elongation, and breaking strength. When the wire is attached to the lead, the tail is broken off by lifting the capillary or by using a clamp. The most commonly used materials are gold, aluminum, and copper. The latter is cheap but hard and needs oxidation prevention by organic coatings [3]. The most commonly used gold wires are doped with beryllium, calcium, or rare earths to slow grain growth and increase strength.

An alternative packaging approach without wire bonding is flip-chip packaging where an array of bumps is placed onto the pads before the die is flipped and attached to the substrate. This approach offers a solution for packages with a higher number of pins.

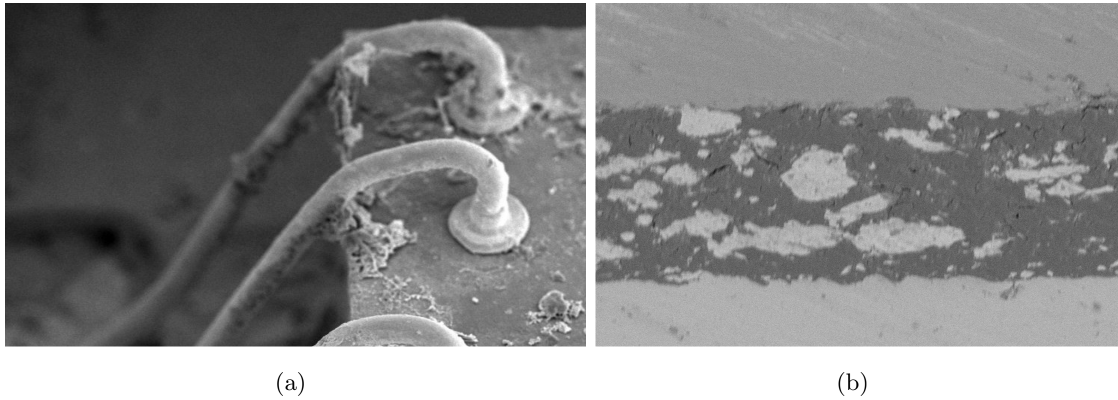

(a) (b)

Figure 1: (a) SEM image of bonding wires on a dummy die surface. (b) Conducting die attach with Ag-particles.

2.1.3 Encapsulation

High volume packaging has changed from expensive ceramic to much cheaper polymeric compounds. These are compounds basically consisting of epoxy and phenol resins filled with silica particles to adjust properties. The main task of the filler is to adjust the coefficient of thermal expansion to that of silicon to reduce stress on the die. The composition and additives are chosen to ensure flame retardance, good cure properties (low shrinkage), adhesion, and mechanical properties. The filler content can be as high as 80 wt.% and therefore also has significant influence on the thermal behavior of the compound. An alumina filler increases the overall thermal conductivity at the costs of a higher CTE. The role of interfaces between filler particles and the epoxy matrix is discussed in section 3.3.5. Effects that are crucial to reliablilty are warpage and delamination due to moisture that evaporates during the reflow soldering process, which also can cause cracking of the package ("popcorning") [1].
The encapsulation process is usually done using compression, injection or transfer molding. In the most common transfer molding process, the material is first preheated and then forced into a cavity that is loaded with the device. The pressure and temperature melt the material and the form of the cavity then gives the desired form of the package. After filling, the epoxy (thermoset) is cured by cooling of the mold. The biggest problem that can occur during the molding process is voiding. This can arise due to pressure gradients or bad adhesion properties.

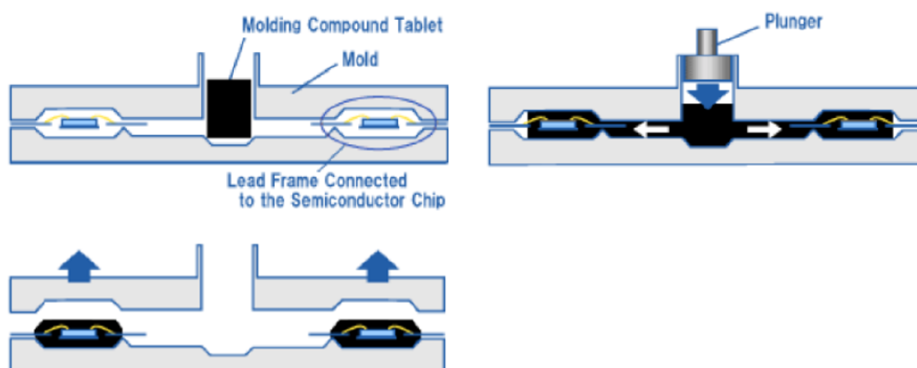

Figure 2: Transfer molding process [4]

3 Heat Transfer Mechanisms

The theory described in this chapter is oriented on various sources, particularly [5, 6, 7, 8, 9]. When investigating thermal transport, three mechanisms need to be taken into account: Heat transport via conduction, convection, and radiation.

3.1 Radiation and Convection

Radiation is described via Stefan-Boltzmann's law,

$$P = A\epsilon\sigma T^4 \tag{3.1}$$

which can be derived easily by integrating Planck's radiation law.
The emitted power is proportional to the fourth power of the body's temperature T and depends on the Stefan-Boltzmann constant $\sigma = 5.67 \cdot 10^{-8}$ $\mathrm{Wm^{-2}K^{-4}}$ and the emissivity ϵ of the body that describes how close the radiating body is to a perfect black body. Here A is the area.
Convection needs to be taken into consideration when looking at moving particles or for the case of natural convection. The velocity of fluid particles is reduced as they come into contact with a boundary layer since they are reflected off the layer. The layer velocity directly at the boundary may then be assumed to be zero. This layer then, by shear stress, retards the particles of the layer above and so on. So the velocity increases perpendicular to the surface until it reaches the free stream velocity.
The particles at the boundary achieve thermal equilibrium with the boundary surface but exchange energy with them of the layer above so that a temperature gradient establishes. The heat flux at the boundary can then be described by Newton's law of cooling [5]

$$q = h(T_S - T_0) \tag{3.2}$$

with the convection heat transfer coefficient h, which depends on the materials and the geometry of the problem, the surface temperature T_S and the ambient temperature T_0. When there is no forced particle flow, natural convection occurs. Due to temperature gradients, density gradients occur and together with gravitation they induce a flow. The density of air decreases with increasing temperature. Meaning in a setup with a heated plate, the density increases towards higher altitudes. Hot air at the plate surface will rise and cool down. This implies stronger gravitational force and therefore a descent of cool air that will be heated up. This circulation pattern will cool the plate surface. Convection and, hence, the heat transfer coefficient, strongly depends on the geometry and flow conditions of the problem.

3.2 The Influence of Natural Convection

When one includes convection, nonstationary assumptions need to be made. In addition to conservation of energy, further conservation laws need to be considered: Conservation of mass of the moving fluid (continuity equation), change of momentum by a force (Newton's second law of motion) and, if the fluid does not consist only out of one species, conservation of that composition.
These governing equations for the boundary layer in case of natural convection are stated as

follows [5]:

$$\frac{\partial u(x,y)}{\partial x} + \frac{\partial v(x,y)}{\partial y} = 0 \tag{3.3}$$

$$u(x,y)\frac{\partial u(x,y)}{\partial x} + v(x,y)\frac{\partial u(x,y)}{\partial y} = g\frac{1}{\rho}(\rho_0 - \rho) + \frac{\mu}{\rho}\frac{\partial^2 u(x,y)}{\partial y^2} \tag{3.4}$$

$$u(x,y)\frac{\partial T}{\partial x} + v(x,y)\frac{\partial T}{\partial y} = \alpha\frac{\partial^2 T}{\partial y^2} \tag{3.5}$$

for u and v the x- and y- components of the mass velocity, parallel respective normal to the surface, g the acceleration due to gravity, ρ the density, μ the viscosity and the thermal diffusivity $\alpha = \kappa/(\rho c_p)$, the ratio of the thermal conductivity κ and the product of density ρ and specific heat at constant pressure c_p.

Heat transfer from the outer device boundaries to the ambient air can be modeled in computational calculations in different ways. The physically accurate way of implementation is a full computational fluid dynamics (CFD) simulation that models laminar or turbulent air flow in a defined air domain. But already the application of a laminar volumetric flow - resulting from the difference of the gravitational force of differently hot and therefore dense air layers - leads to computational instabilities. These might be solved by sweeping the viscosity value of the air domain and using these auxiliary results for the next sweep step. But due to the enormous node number of the models this approach is computationally not affordable for this work.

To overcome this problem, two methods are mostly used to include natural convection into thermal finite element simulations. First, heat transfer by natural convection can just be implemented by defining heat transfer coefficients h that establish a heat flux following eq. 3.2. The coefficient itself is defined by

$$h = \frac{-\kappa_f \frac{\partial T}{\partial y}\Big|_{y=0}}{T_s - T_0} = \frac{\kappa_f}{L}\frac{\partial T^\star}{\partial y^\star}\Big|_{y^\star=0} \equiv \frac{\kappa_f}{L}\mathrm{Nu} \tag{3.6}$$

using dimensionless independent variables

$$y^\star \equiv \tfrac{y}{L} \quad \text{and} \quad T^\star \equiv \tfrac{T - T_s}{T_0 - T_s}$$

the thermal conductivity of air κ_f and defining the dimensionless temperature gradient at the surface, the Nusselt number Nu. The first equivalence comes from the combination of eq. 3.2 and 3.11 at the objects surface at $y = 0$.

The Nusselt number is a function of the geometry of the configuration and the Reynolds number, a measure of laminarity of the flow. It represents the ratio of the inertia to viscous forces and describes the transition from laminar to turbulent flow conditions.

$$Re_L = \frac{\rho v L}{\mu} \tag{3.7}$$

with v the maximum velocity of the fluid and L the characteristic length of the system, which will be discussed in the results section. More detailed information can be found in [5] and various fluid dynamics books.

Models for Nusselt numbers of basic geometries have been derived. To include natural convection, two cases of heat transfer coefficient estimations were used: Vertical wall and horizontal

plate conditions. The corresponding coefficients are stated in eq. 3.8 and 3.9 [5].

$$h = \begin{cases} \frac{\kappa_f}{L}\left(0.68 + \frac{0.67 Ra_L^{1/4}}{\left(1+\left(\frac{0.492k}{\mu C_p}\right)^{9/16}\right)^{4/9}}\right) & Ra_L \leqslant 10^9 \\ \frac{\kappa_f}{L}\left(0.825 + \frac{0.387 Ra_L^{1/6}}{\left(1+\left(\frac{0.492k}{\mu C_p}\right)^{9/16}\right)^{8/27}}\right)^2 & Ra_L > 10^9 \end{cases} \tag{3.8}$$

$$h = \begin{cases} \frac{\kappa_f}{L} 0.54 Ra_L^{1/4} & Ra_L \leqslant 10^7 \\ \frac{\kappa_f}{L} 0.27 Ra_L^{1/4} & Ra_L > 10^7 \end{cases} \tag{3.9}$$

with the Rayleigh number

$$Ra_L = \frac{g \left|\frac{\partial \rho}{\partial T}\right|_p \rho C_p \left|T - T_0\right| L^3}{\kappa_f \mu} \tag{3.10}$$

.

3.3 Thermal Conduction

The part of heat transfer most important for solids is thermal conduction. It is governed mainly by electrical carriers and phonons. The contributions of all carriers and excitations add up to the total thermal conductivity κ. While in metals electrons carry most of the heat, phonons dominate heat transport in insulators.
In the diffusive regime for timescales much greater than the scattering mean free time (τ) and length scales much greater than the mean free path (λ) of the energy carriers, thermal conductivity is defined by the ratio of the heat flux to a temperature gradient described by Fourier's law

$$\kappa = -\frac{\vec{q}}{\vec{\nabla} T}. \tag{3.11}$$

where $\vec{q}$ is the heat flux which is the particle current, $-D\nabla n$ times their average energy $\bar{E} = \frac{u}{n}$ with D the diffusion constant, u the internal energy, n the particle density and $c_v = \frac{du}{dT} := \frac{\kappa}{D}$.
When looking at a gas with an applied one dimensional temperature gradient, the energy flow equals the number of particles crossing one point before being scattered times their energy:

$$\vec{q} = \frac{1}{2} n (E(x-\lambda) - E(x+\lambda)) \overline{v}_x = -n \left(\frac{\partial E}{\partial T} \frac{\partial T}{\partial x} \lambda\right) \overline{v}_x$$

with $\overline{v_x} = \frac{1}{3}\overline{v}$ the Fermi velocity and the heat capacity $c_v = n\frac{\partial E}{\partial T}$ and the sum over various gas species i

$$\kappa = \frac{1}{3} \sum_i c_{v,i} \overline{v}_i \lambda_i \tag{3.12}$$

3.3.1 Electronic Thermal Conductivity

The electrical current density $\vec{j}$ is defined as the charge times the velocity, the density $D(\vec{k})$, and the occupation $f(\vec{k})$ of all states $\vec{k}$

$$\vec{j} = -\int e\vec{v}(\vec{k})D(\vec{k})f(\vec{k})d\vec{k} \tag{3.13}$$

and the heat flux

$$\vec{q} = -\int (E(\vec{k}) - \mu)\vec{v}(\vec{k})D(\vec{k})f(\vec{k})d\vec{k} \tag{3.14}$$

with only energies above the chemical potential contributing.
The distribution function $f(\vec{k})$ can be determined using the Boltzmann equation and the relaxation time approximation [10]

$$\frac{\mathrm{d}f}{\mathrm{d}t} = -\frac{\vec{F}_{ext} \cdot \nabla_{\vec{k}} f}{\hbar} - \vec{v} \cdot \nabla f + \frac{f_0(\vec{k}) - f(\vec{k})}{\tau(\vec{k})} \tag{3.15}$$

With

$$\vec{F}_{ext} = -e\vec{E} \tag{3.16}$$

and

$$\nabla f_0 = \frac{\partial f_0}{\partial T}\nabla T + \frac{\partial f_0}{\partial \mu}\nabla \mu \tag{3.17}$$

it follows in steady-state

$$\frac{f(\vec{k}) - f_0(\vec{k})}{\tau(\vec{k})} = -\vec{v}(\vec{k}) \cdot \left(-\frac{E(\vec{k}) - \mu}{T}\frac{\partial f_0}{\partial \mu}\nabla T + e\frac{\partial f_0}{\partial \mu}\left(\vec{E} - \frac{\nabla \mu}{e}\right)\right) \tag{3.18}$$

with the equilibrium distribution function for fermions, the Fermi function $f_0(\vec{k})$.
Then

$$\vec{j} = e\int \tau(\vec{k})\vec{v}(\vec{k})D(\vec{k})\vec{v}(\vec{k}) \cdot \left(-\frac{E(\vec{k}) - \mu}{T}\frac{\partial f_0}{\partial \mu}\nabla T + e\frac{\partial f_0}{\partial \mu}\left(\vec{E} - \frac{\nabla \mu}{e}\right)\right) \mathrm{d}\vec{k} \tag{3.19}$$

and

$$\vec{q} = \int \tau(\vec{k})(E(\vec{k}) - \mu)\vec{v}(\vec{k})D(\vec{k})\vec{v}(\vec{k}) \cdot \left(-\frac{E(\vec{k}) - \mu}{T}\frac{\partial f_0}{\partial \mu}\nabla T + e\frac{\partial f_0}{\partial \mu}\left(\vec{E} - \frac{\nabla \mu}{e}\right)\right) \mathrm{d}\vec{k} \tag{3.20}$$

The current is not required to flow in the direction of the electric field. But for many materials (e.g. cubic) $\vec{j} \parallel \vec{E}$ and eq. 3.19-3.20 can be simplified [8]. In the free electron model, so considering metals, and defining an effective electric field $\vec{E}_{eff} = \vec{E} - \frac{\nabla \mu}{e}$ and the integral K_n as

$$K_n = -\frac{2}{(2\pi)^3}\int \vec{v}(\vec{k})^2\tau(\vec{k})((E(\vec{k}) - \mu)^n\frac{\partial f_0}{\partial E}d\vec{k} \tag{3.21}$$

then

$$\vec{j} = e^2 K_0 \vec{E}_{eff} - \frac{e}{T}K_1\nabla T \tag{3.22}$$

and

$$\vec{q} = eK_1\vec{E}_{eff} - \frac{1}{T}K_2\nabla T \tag{3.23}$$

When $\vec{j} = 0$ eqns. 3.22 and 3.23 give the electronic contribution to the thermal conductivity

$$\kappa_e = \frac{1}{T}\left(K_2 - \frac{K_1^2}{K_0}\right) \tag{3.24}$$

Using $\sigma = e^2K_0$ from eq. 3.22 and - since the derivative of the equilibrium distribution $\frac{\partial f_0(\vec{k})}{\partial E(\vec{k})}$ is a narrow function around the chemical potential - expanding K_n around μ gives

$$K_n = [(E(\vec{k}) - \mu)^n\frac{\sigma(E(\vec{k}))}{e^2} + \frac{\pi^2}{6}(k_BT)^2 \cdot \frac{\partial^2}{\partial E^2}\left((E(\vec{k}) - \mu)^n\frac{\sigma(\vec{k})}{e^2}\right) + O(k_BT)^4]_{E(\vec{k})=\mu} \tag{3.25}$$

and therefore gives the constant ratio between the electronic contribution to thermal and the electrical conductivity, the Wiedemann-Franz law

$$\frac{\kappa_e}{\sigma T} = \frac{\pi^2}{3}\frac{k_B^2}{e^2} + O\left(\frac{k_BT}{\mu}\right)^2 \tag{3.26}$$

with the Lorentz number

$$L_0 = \frac{\kappa_e}{\sigma T} = \frac{\pi^2}{3}\frac{k_B^2}{e^2} = 2.4453 \cdot 10^{-8}\ \mathrm{W\Omega/K^2} \tag{3.27}$$

When including the Seebeck-coefficient S, which is the prefactor in the relation for the effective electric field of eq. 3.22 when setting $\vec{j} = 0$

$$E_{eff} = \frac{K_1}{K_0eT}\nabla T = ST \tag{3.28}$$

The conductivity ratio becomes:

$$\frac{\kappa_e}{\sigma T} = L_0 - S^2 \tag{3.29}$$

with a negligible small S for metals at room temperature.

3.3.2 Phonon Thermal Conductivity

The main contributors to phonon thermal transport are acoustic branches since the group velocity of optical phonons is typically small. Nevertheless, they interact with acoustic phonons and therefore also affect the thermal conductivity.
The analogon of the Boltzmann function eq. 3.18 for phonons is [8, 11]

$$\frac{N(\vec{K}) - N_0(\vec{K})}{\tau(\vec{K})} = -(\vec{v}_g \cdot \nabla T)\frac{\partial N_0(\vec{K})}{\partial T} \tag{3.30}$$

with $N(\vec{K})$ the distribution function for phonons with wavevector $\vec{K}$ and $N_0(\vec{K})$ the Bose-Einstein distribution, the equilibrium distribution for bosons. Again, in the isotropic case, and

using that the heat flux for phonons is, integrating over all phonon modes $\vec{K}$,

$$\begin{aligned}\vec{q} = &\int N(\vec{K})\hbar\omega(\vec{K})\vec{v}_g D(K)\mathrm{d}\vec{K} \\ &= -\int \hbar\omega(\vec{K})v_g^2\langle\cos^2\theta\rangle\tau(\vec{K})\frac{\partial N_0(\vec{K})}{\partial T}\nabla T D(K)\mathrm{d}\vec{K} \\ &= -\frac{1}{3}\int \hbar\omega(\vec{K})v_g^2\tau(\vec{K})\frac{\partial N_0(\vec{K})}{\partial T}\nabla T D(K)\mathrm{d}\vec{K}\end{aligned} \tag{3.31}$$

with $D(K)$ the density of phonon states, where for a cubic lattice $D(K) = 3K^2/(2\pi^2)\mathrm{d}K$ [6]. In the Debye model, a linear dispersion relation $\omega(\vec{K}) = vK$ is used. Together with eq. 3.31, this leads to the lattice contribution of the thermal conductivity [8]

$$\kappa_L = \frac{k_B}{2\pi^2 v^3}\left(\frac{k_B}{\hbar}\right)^3 T^3 \int_0^{\theta_D/T} \tau(x)\frac{x^4 e^x}{(e^x-1)^2}\mathrm{d}x \tag{3.32}$$

with $x = \frac{\hbar\omega}{k_B T}$ and the Debye temperature $\theta_D = \frac{\hbar\omega_D}{k_B}$. The Debye frequency ω_D is defined so that for the total number of phonon modes N satisfies

$$3N = \int_0^{\omega_D} D(\omega)d\omega \tag{3.33}$$

Comparing that to the Debye result of the specific heat [6]

$$C_V = 9Nk_B\left(\frac{T}{\theta}\right)^3 \int_0^{\theta_D/T} \mathrm{d}x\frac{x^4 e^x}{(e^x-1)^2} = \frac{3k_B}{2\pi^2 v^3}\left(\frac{k_B}{\hbar}\right)^3 T^3 \int_0^{\theta_D/T} \mathrm{d}x\frac{x^4 e^x}{(e^x-1)^2} \tag{3.34}$$

and using that the mean free path $\lambda(x) = v\tau(x)$, the Debye approximation for the lattice thermal conductivity eq. 3.32 can be reduced to the form of eq. 3.12

$$\kappa_L = \frac{1}{3}\int_0^{\theta_D/T} C(x)v\lambda(x)\mathrm{d}x \tag{3.35}$$

The BTE can be solved using various approaches, such as the lattice Boltzmann method, lattice dynamics calculations, and molecular dynamics approaches like the Green-Kubo method [12]. Since the thermal conductivity is directly proportional to the group velocity of the phonons, it is generally assumed that acoustic phonons carry most of the heat. Nevertheless Mittal *et al.* [13] reported a contribution of 25 % of energy transport due to optical phonons in silicon thin films at room temperature.

3.3.3 Scattering Processes

Electron transport in a material is mostly affected by three effects: Electrons scattering from phonons which is called the ideal resistance (due to the fact that it cannot be avoided), electron-defect interactions, and electron-boundary scattering. The effective relaxation time τ_e of the electrons is the reciprocal sum of that of the different scattering mechanisms, as stated in Matthiessen's rule

$$\frac{1}{\tau_e} = \frac{1}{\tau_{defect}} + \frac{1}{\tau_{boundary}} + \frac{1}{\tau_{phonon}} \tag{3.36}$$

and so the resistances due to the different mechanisms add up. Electron-electron processes can be added to that sum, especially when considering very pure metals at very low temperatures. Considering entropy production by a thermal current due to a temperature gradient, Ziman [9] states that the ideal electrical resistance is at high temperatures ($T >> \theta_D$) $\rho_i \propto T$, the ideal electronic thermal resistance $1/\kappa_{e,i}$ = const. and the Wiedemann-Franz law is obeyed. At low temperatures ($T << \theta_D$) the Wiedemann-Franz law does not hold, $\rho_i \propto T^5$ and $1/\kappa_{e,i} \propto T^2$.
Impurity scattering is considered to be purely elastic and the scattered electron does not lose energy, therefore, Fermi's golden rule gives a collision probability

$$\frac{1}{\tau_{defect}} \propto W_{kk'} = \frac{2\pi}{\hbar}\delta(E(\vec{k}) - E(\vec{k'}))|\langle\vec{k'}|V|\vec{k}\rangle|^2 \tag{3.37}$$

with a proportionality factor including $1 - \cos(\theta)$ with θ being the angle between $\vec{k}$ and $\vec{k'}$, and V e.g. an ionized impurity potential modeled by a screened Coulomb potential. Large angle scattering processes contribute stronger to the relaxation time τ but still all electrons get scattered by static lattice defects with the same effectivity and no temperature dependence in the relaxation time occurs. Then, the Wiedemann-Franz law gives a T^{-1} proportionality for the thermal analogon $1/\kappa_{e,0}$.
So since at low temperatures $\kappa_{e,i}$ increases and $\kappa_{e,0}$ decreases, impurity scattering dominates the electronic thermal conductivity in this temperature region. At higher temperatures the ideal resistance takes over, κ_e will show a maximum and then decrease towards the constant value for $1/\kappa_{e,i}$ at high temperatures. Increasing defect concentration reduces the peak size in κ_e, since impurity scattering dominates to higher temperatures. Boundary scattering must be considered for thin films or nanodevices. Its basic effect is the reduction of the mean free path of the electrons and therefore κ_e.

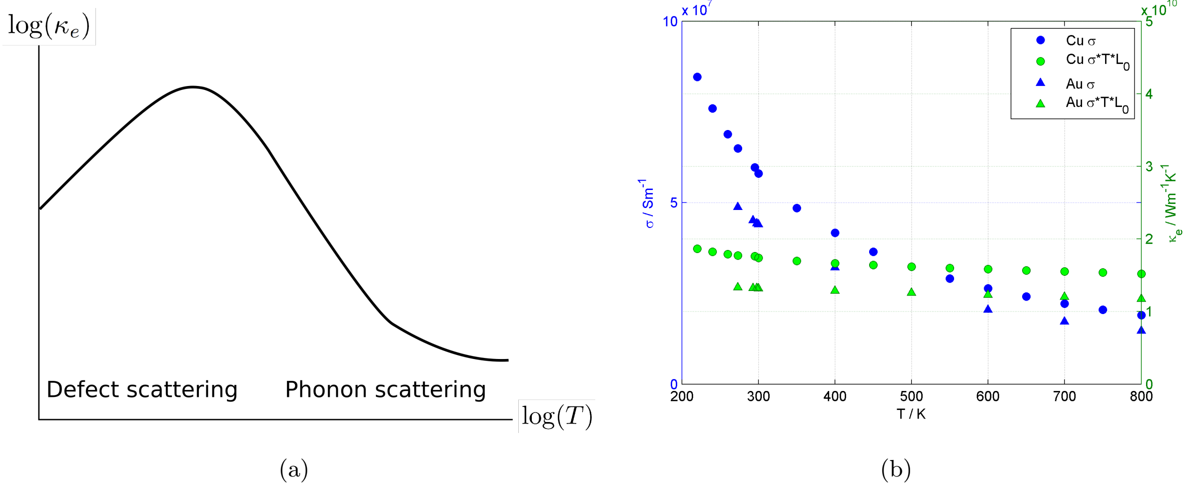

Figure 3: (a) Scattering contributions to the electronic thermal conductivity κ_e (after [7]). (b) Electrical conductivity and electronic thermal conductivity calculated using the Wiedemann-Franz law [14, 15].

3.3.4 N- and U- Processes

When an electron or a phonon scatters off another phonon the total momentum needs to be conserved. A phonon can be annihilated or created:

$$\vec{K}_1 \pm \vec{K}_2 = \vec{K}_3 \pm \vec{G} \tag{3.38}$$

with $\vec{G}$ a reciprocal lattice vector. "Normal" processes (N-processes) for which $\vec{G} = 0$ do not contribute to thermal resistance directly but are transferring energy between different phonon modes and are therefore preventing too large deviations from the equilibrium distribution. Umklapp processes (U-processes) do not conserve the total crystal momentum and give rise to thermal resistance since they can generate large changes in and almost reverse the direction of the phonon wavevector as shown in fig. 4.

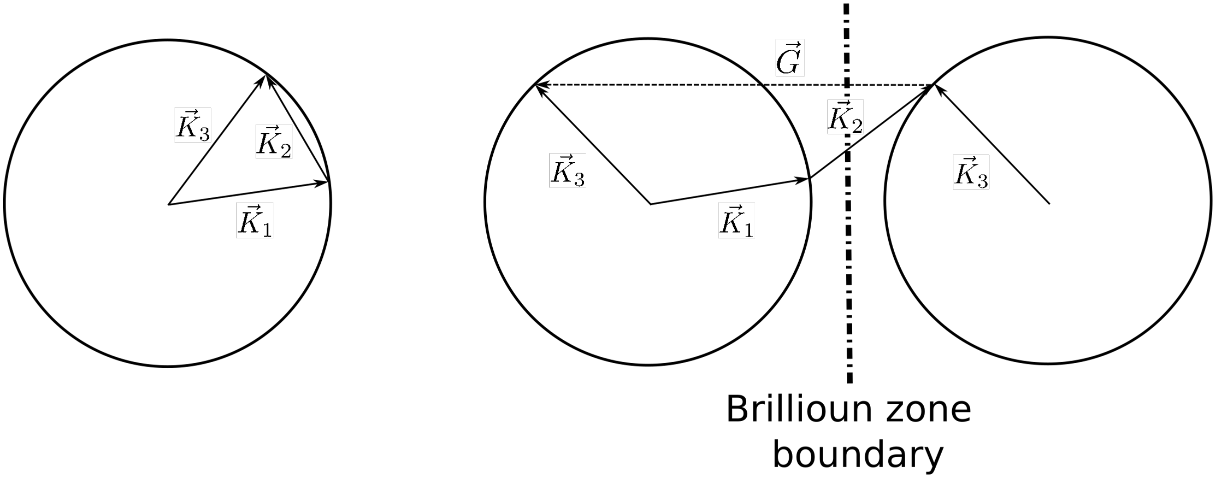

Figure 4: Umklapp scattering. The sum of the two momenta crosses the Brillioun zone and the added reciprocal lattice vector changes the direction of the final wavevector (after [8]).

Different scattering mechanisms contribute reciprocally to the total relaxation time. But since N-processes do not restore the equilibrium distribution, another model was found to include their impact on the thermal conductivity, the Callaway model [16]. The relaxation time approximation always underestimates κ and another scattering term is added to that of eq. 3.30 with $\tau_U(\vec{K})$ being the relaxation time for U- and $\tau_N(\vec{K})$ that for N-processes:

$$\frac{N(\vec{K}) - N_0(\vec{K})}{\tau_U(\vec{K})} + \frac{N(\vec{K}) - N^\star(\vec{K})}{\tau_N(\vec{K})} = -(\vec{v}_g \cdot \nabla T)\frac{\partial N_0(\vec{K})}{\partial T} \tag{3.39}$$

The N-processes relax to a displaced distribution

$$N^\star(\vec{K}) = \frac{1}{e^{\hbar\omega/k_B T + \vec{\Lambda}\cdot\vec{K}} - 1} \tag{3.40}$$

where $\vec{\Lambda}$ is linear with ∇T and can be determined using the fact that N-processes do not change the total phonon momentum.

There are different (often empirical) approaches to determine the relaxation times for different

scattering mechanisms, which will not be stated here. Besides N- and U-scattering, defect scattering, boundary scattering, and electron scattering are the main contributors to phonon thermal resistance, which dominate at different temperature regimes as one can see in fig. 5 where at high temperatures umklapp scattering takes over boundary and defect scattering that dominate at low temperatures. At high temperatures, the increase of resistance due to umklapp scattering is stronger than the conductivity increase due to additional phonons, since the scattering rate of more phonon processes increases more rapidly [17]. New anharmonic lattice dynamics calculations have shown that an inclusion of four-phonon processes (where $1/\tau$ increases like T^2) show a comparable or even higher ratio of Umklapp processes that can reduce the thermal conductivity of a less anharmonic material like silicon by about 25 % at 1000 K [18].

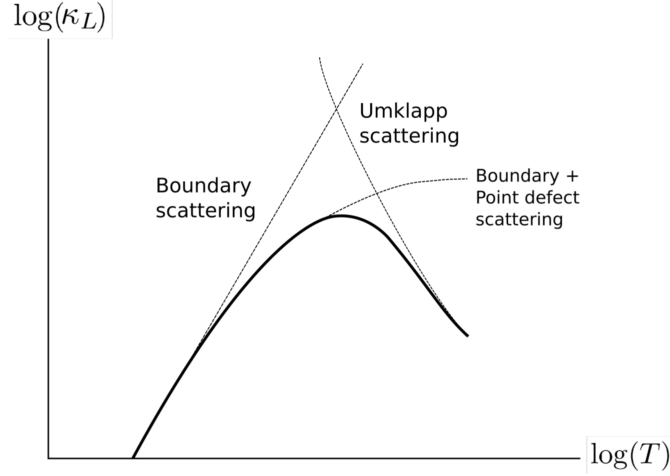

Figure 5: Main scattering contributions to the lattice thermal conductivity (after [8]).

Goldsmid [8] suggests a reduction of the thermal conductivity due to phonon-boundary scattering of

$$\Delta\kappa_{ph_b} = -\frac{2}{3}\kappa_0\sqrt{\frac{\lambda_{ph}}{3L}} \tag{3.41}$$

with κ_0 being κ without point-defect scattering and L the average grain size.
The Callaway model (3.39) usually fits best for isotropically pure crystals while the Debye model (3.32) applies to solids with an appreciable amount of impurities.

It should be mentioned that the simple picture of wave vector direction change due to momentum conservation, described above, is an oversimplification. The quantity that needs to be conserved is the quasimomentum $\hbar\vec{k}$ that is only defined modulo $\hbar\vec{G}$. There are many arguments that can not be resolved using the easy picture. For example, when looking at the phonon dispersion of silicon (figure 6a), a N-process of two longitudinal acoustic phonons $\vec{k}_1$ yields a longitudinal optical phonon $\vec{k}_3$ with reversed group velocity. This shows that the categorization of one particular scattering process into the normal or umklapp category depends on the choice of the primitive unit cell. Therefore, it is better to look at the heat flux, defined as the product of phonon energy and group velocity $\vec{v}_g$ [19]

$$\vec{q} = \frac{1}{(2\pi)^3}\int \hbar\omega\vec{v}_g n_{\vec{k}} \mathrm{d}\vec{k} \tag{3.42}$$

with $n_{\vec{k}}$ the phonon occupation in the wave vector space. Then, in the Debye model, where $\omega\vec{v} = \vec{k}v^2$, N-processes conserve and U-processes do not conserve the direction of the heat flux, since a change of direction of $\vec{k}$ gives a change of the direction of the group velocity. But already in the simplified picture of linear longitudinal and transverse acoustic branches, one can show that processes within the first Brillouin zone can flip the direction of the heat flux (figure 6b). If quasimomentum and energy are conserved for scattering of $\vec{k}_1$ and $\vec{k}_2$ yielding $\vec{k}_3$, then

$$\vec{k}_1 = -\frac{1-\frac{v_T}{v_L}}{1+\frac{v_T}{v_L}}\vec{k}_3 \text{ and } \vec{k}_2 = \frac{2}{1+\frac{v_T}{v_L}}\vec{k}_3 \tag{3.43}$$

with v_T and v_L the group velocities of the transverse and the longitudinal branch. Then, the scattering process only contributes to a flip in the direction of the heat flux, eq. 3.42, if $\frac{v_T}{v_L} < \frac{1}{2}$ [19].

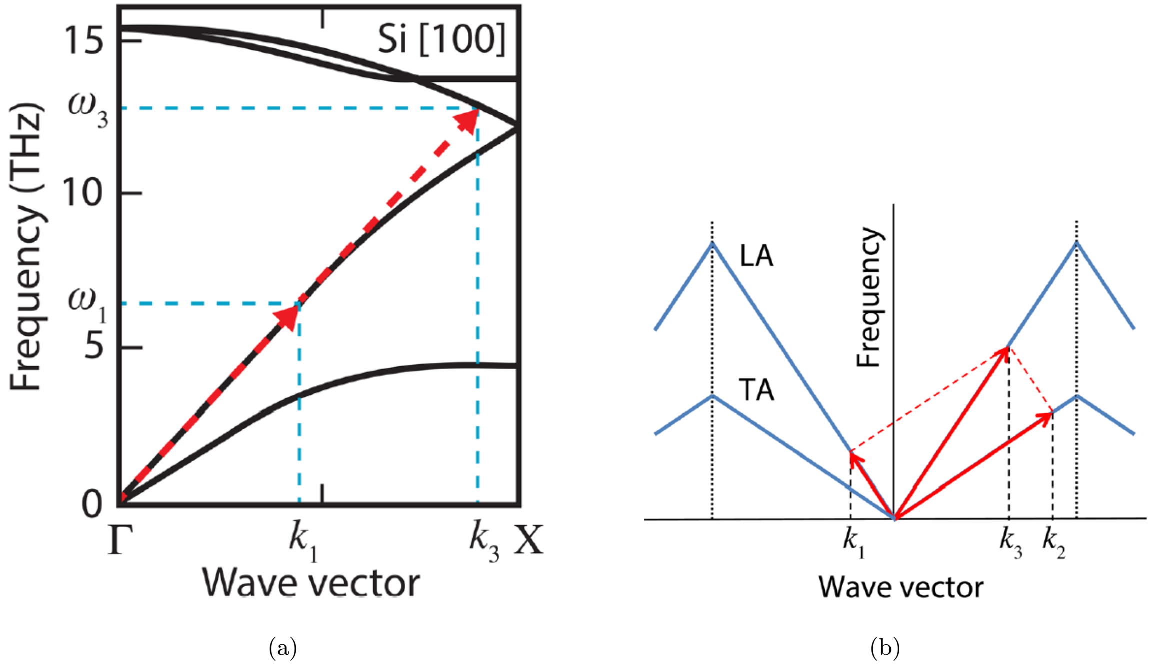

(a)

(b)

Figure 6: (a) Phonon dispersion of silicon [19]. Scattering of two longitudinal acoustic phonons k_1 yields a longitudinal optical phonon k_3 with reversed group velocity, (b) phonon scattering in a linear dispersion with longitudinal and transverse acoustic branches within the Brillouin zone flips the direction of the heat flux [19].

3.3.5 Thermal Interface Resistance

With the decrease of node sizes and semiconductor devices in general (transistors, MEMS, etc.) it is not sufficient anymore to only consider bulk effects. Interface effects need to be taken into account or at least into consideration. The investigation of heat transport phenomena shows that the thermal resistance of multilayered samples is higher than the sum of their bulk components.

Swartz *et al.* [20] explain the effect of a thermal interface resistance, which was first obtained by Kapitza in 1941, who reported a temperature drop near a helium to solid boundary, using the diffusive mismatch model (DMM). This boundary resistance (Kapitza resistance) is defined

as the ratio of the temperature discontinuity at the interface to the power per unit area flowing across that interface.

The Diffusive Mismatch Model

The most accepted explanation for this effect at elevated temperatures is the diffusive mismatch model (DMM) constructed by Swartz *et al.* [20]. Heat conducting phonons are scattered at the interface. Contrary to the acoustic mismatch model (AMM) for low temperatures below 1 K, which assumes a geometrically perfect interface and entirely elastic phonon transport (phonons treated as plane waves), the DMM assumes that all phonons that strike the interface are scattered diffusively forwards or backwards with a probability depending on the phonon density of states of the interfacing materials.
If the temperatures on both sides of the interface are the same, no net heat flow can occur and the number of phonons of one state moving from one material to the other needs to be the same as in the opposite direction. Using this principle of detailed balance, it is sufficient to calculate the net heat flow from side 1 at T_1 to side 2 at T_2 by the difference of the heat flows from side 1 to side 2 when side 1 is at T_1 and at T_2.
The heat current density $\frac{1}{A}\dot{Q}_{1\to2}(T)$ is the sum over all phonons incident on an area A times their energies $\hbar\omega = \hbar c_{1,j}k$ with j the phonon mode and k the wavevector. The number of phonons incident by angles φ and θ is

$$\frac{N_{1,j}(\omega,T)}{4\pi}d\Omega c_{1,j}\cos\theta \tag{3.44}$$

with N the density of states times the occupation probability defined by the Bose-Einstein distribution, and $d\Omega = d\varphi\sin\theta d\theta$ that gives the velocity contribution normal to the interface. Then the heat current is

$$\frac{\dot{Q}_{1\to2}(T)}{A} = \frac{1}{2}\sum_j\int_0^{\frac{\pi}{2}}\int_0^{\omega_1^{max}} N_{1,j}(\omega,T)\hbar\omega c_{1,j}\cdot\alpha_{1\to2}(\theta,j,\omega)\cdot\cos\theta\sin\theta d\theta d\omega \tag{3.45}$$

with the transmission probability α, ω^{max} the maximum phonon frequency and the integral over φ giving a factor of 2π.
For small temperature differences, the boundary resistance is then just

$$\frac{1}{h_{bd}} = \frac{A(T_2-T_1)}{\dot{Q}_{1\to2}(T_2)-\dot{Q}_{1\to2}(T_1)} \tag{3.46}$$

The transmission probability $\alpha_{1\to2}$ can then be calculated using the assumption that all phonons scatter and that the transmission probability does not depend on the wavevector and mode of the phonon by

$$\alpha_1(\omega) = 1-\alpha_2(\omega) \tag{3.47}$$

The number of phonons leaving one side of the interface per unit time is

$$\sum_j\int_0^{2\pi}\int_0^{\frac{\pi}{2}} d\theta\cos\theta d\varphi c_{i,j}N_{1,j}(\omega,T)\alpha_i(\omega) \tag{3.48}$$

which, including that the transmission probability is independent of the incident angle, together with eq. 3.47, gives

$$\sum_j c_{i,j} N_{i,j}(\omega, T)\alpha_i(\omega) = \sum_j c_{3-i,j} N_{3-i,j}(\omega, T)(1 - \alpha_i(\omega)) \tag{3.49}$$

and

$$\alpha_i(\omega) = \frac{\sum_j c_{3-i,j} N_{3-i,j}(\omega, T)}{\sum_j c_{i,j} N_{i,j}(\omega, T)} \tag{3.50}$$

Duda *et al.* [21] describe a model that distinguishes between completely diffuse scattering - like described above - and partially diffuse scattering. In the latter case, the scattered carriers lose their memory of their initial direction, but maintain their polarization. Then the principle of detailed balance needs to be applied to the flux per polarization. Further it can be applied per wavevector, so that the amount of inelasticity in the scattering process is included. Then both sides in eq. 3.49 are multiplied by $E(k)$ and integrated over all k-values for each material, which may underpredict the interface resistance since it does not account for the lower probability of higher-order phonon processes. Elasticity is included by integrating on both sides only up to the lower cutoff frequency of the two materials. Therefore, considerable phonon flux towards the boundary is neglected and the boundary resistance will be overestimated. They suggest as a best compromise the completely diffuse model but using the lower dispersion relation of the two materials for both of them.

Thermal interface resistance has appreciable influence in the ballistic regime at length scales smaller than the phonon mean free path. Molecular dynamics (MD) simulations [22] suggest an inverse power law dependence on the system length and no influence of dimensions perpendicular to that of the heat flux. MD simulations and time-dependent thermoreflectance measurements for silicon-germanium and silicon-aluminum interfaces give resistance values in the range of (1-3)$\cdot 10^{-9}$ m^2KW^{-1} [22, 23]. But also for interfaces between materials with highly dissimilar Debye temperatures the interface resistance does not exceed values of 1.25 $\cdot 10^{-7}$ m^2KW^{-1} [24].

A more considerable influcence of thermal interface resistance was found in organic-inorganic superlattice thin films deposited by atomic layer deposition (ALD) [25]. The thermal conductivity of TiO_2 and ZnO superlattices was heavily reduced by periodically including hydroquinone ($C_6H_4(OH)_2$) layers. This reduction by a factor of about 10 also surpasses the theoretical minimal thermal conductivity based on a model of a lowest conductivity limit when the phonon mean free path in the amorphous state reaches the atomic spacing. Fukushima *et al.* report a thermal resistance of $1 \cdot 10^{-6}$ m^2KW^{-1} corresponding to the AlN-epoxy resin interface in a sandwich structure [26]. This effect is of notable importance to composite materials like the mold compound that is a combination of resins and silica filler particles. In the SiP package, described in section 5.1, the thickness of the mold compound above the die consists of 31 ± 5 organic/inorganic matrix-filler interfaces which is equivalent to a 55 μm thick pure silica layer with a thermal conductivity of κ = 1.8 $Wm^{-1}K^{-1}$ at room temperature. Reliability criteria like a coefficient of thermal expansion close to that of silicon to reduce stress, low moisture sensitivity, and adhesion properties are in the main focus of mold composition selection, filler content, and particle size. But still, from the view of thermal optimization a lower filler content with a bigger particle size could be advantageous.

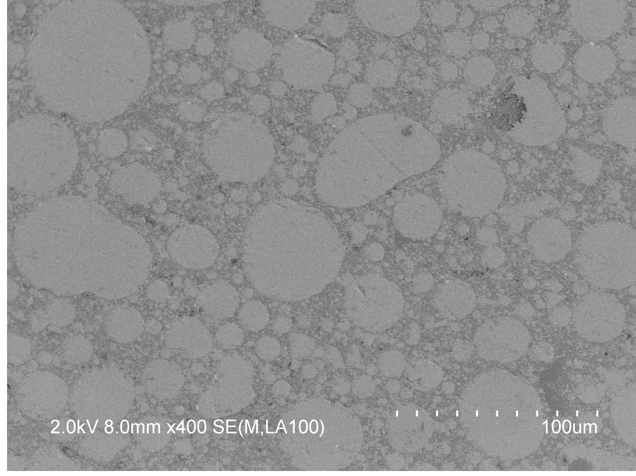

Figure 7: SEM image of silica filler particles embedded in a resin matrix.

3.3.6 Thermal Conduction in Semiconductors

For semiconductors, one cannot generalize that heat transport is mainly governed by electrons or phonons. Also, the range of thermal conductivities is large. For instance, the thermal conductivity of diamond is higher than that of metals. Another feature of semiconductors is that heat transport is not only restricted to electronic and phononic thermal conduction. Due to conduction of electrons and holes, bipolar heat conduction may govern heat transfer characteristics of a semiconducting material.

If there are two types of carriers, their current densities are defined by the sums of their electrical conductivities and the contribution of the electromotive field of the Seebeck effect [27, 8]:

$$i_l = \sigma_l \left(E - S_l \frac{\partial T}{\partial X} \right) \tag{3.51}$$

with $l = 1, 2$ for electrons and holes.

If there is no current, so $i = i_1 + i_2 = 0$ and considering one dimension, then

$$(\sigma_1 + \sigma_2)E = (S_1\sigma_1 + S_2\sigma_2)\frac{\partial T}{\partial x} \tag{3.52}$$

and

$$S = \frac{S_1\sigma_1 + S_2\sigma_2}{\sigma_1 + \sigma_2} \tag{3.53}$$

Considering the heat flux, not only the Fourier component from eq. 3.11 but also the Peltier effect needs to be taken into consideration:

$$\vec{q} = (\Pi_A - \Pi_B) \cdot \vec{i} \tag{3.54}$$

with

$$\Pi_{mn} = \frac{q_m}{i_n} = T \cdot S_{mn} \tag{3.55}$$

gives

$$\vec{q_l} = S_l T i_l - \kappa_{e,l} \frac{\partial T}{\partial x} \tag{3.56}$$

And again with

$$i_1 = -i_2 = \frac{\sigma_1 \sigma_2}{\sigma_1 + \sigma_2}(S_1 - S_2)\frac{\partial T}{\partial x} \tag{3.57}$$

$$\vec{q} = \vec{q}_1 + \vec{q}_2 = -\left(\kappa_{e,1} + \kappa_{e,2} + \frac{\sigma_1 \sigma_2}{\sigma_1 + \sigma_2}(S_1 - S_2)^2 T\right)\frac{\partial T}{\partial x} \tag{3.58}$$

So the total electronic thermal conductivity (inside the brackets of eq. 3.58) does not only consist of the electronic thermal conductivity contributions from electrons and holes but also out of a bipolar contribution. This depends on the difference in the Seebeck coefficients which should be largest for intrinsic semiconductors with a wide band gap. Still, for large band gap semiconductors the bipolar contribution is often so small that it is overshadowed by lattice thermal conduction.

3.3.7 Thermal Conduction in Polymers

The thermal conductivity of a polymer is mainly governed by its phase and therefore by the glass transition temperature T_g. Amorphous polymers do not undergo a phase transition from solid to liquid to gaseous like simple molecules. For example they decompose before boiling and so cannot be evaporated. Polymers are classified via the thermodynamically metastable glassy, rubbery and semi-crystalline state. The glassy-rubbery transition is a kinetically controlled transition characterized by T_g. Figure 8 shows the phases depending on molar mass and temperature.

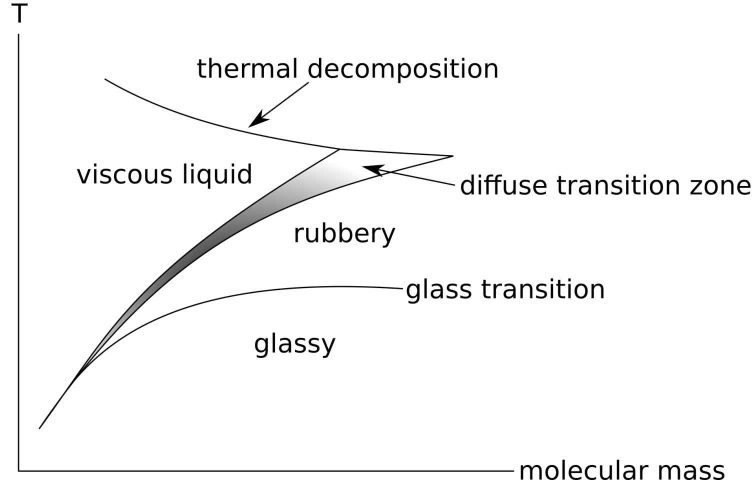

Figure 8: Phase transitions of amorphous polymers (after [28]).

Van Krevelen [28] states the thermal conductivity in polymers

$$\kappa = L\frac{C_p}{V}\left(\frac{U_R}{V}\right)^3\left[\frac{3(1-v)}{1+v}\right]^{1/2} \tag{3.59}$$

with a constant L, V the volume, C_p the specific heat at constant pressure, $v = 1/2$ for liquids and U_R the molar sound velocity function. By fitting experimental results, Bicerano [28] suggested an approximated temperature dependence of the thermal conductivity of amorphous polymers of

$$\frac{\kappa(T)}{\kappa(T_g)} = \left(\frac{T}{T_g}\right)^{0.22} \tag{3.60}$$

with an ascending behavior below the glass temperature T_g as can be seen in figure 9 while κ increases with an increase of crystallinity [28].

$$\frac{\kappa_c}{\kappa_a} - 1 = 5.8 \left(\frac{\rho_c}{\rho_a} - 1 \right) \tag{3.61}$$

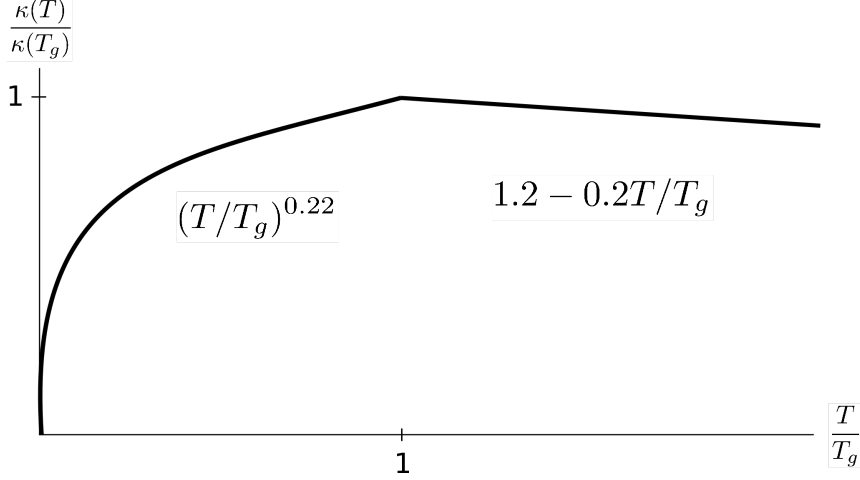

Figure 9: Temperature dependence of the thermal conductivity of amorphous polymers (after [28]).

Typical room temperature values of the thermal conductivity of a phenolic resin or epoxy resin are stated as $\kappa = 0.176$ J/(m · K) and $\kappa = 0.180$ J/(m · K) [28], respectively.

3.3.8 Thermal Conduction in Adhesives

Adhesives used for die attaching often consist of an epoxy resin with electrically conducting filler particles, for example Ag-flakes. Heat transport through the adhesive is then mainly governed by the formation of conductive paths through the merely conducting epoxy. The thermal resistance between two surfaces attached together by an adhesive is then the sum of all bulk resistances in a heat path and the thermal interface resistance between the particles. Meaning less contact between particles and therefore larger particles of a filler increase its thermal conductivity. The thermal conductivity of an adhesive with 50 wt% alumina filler was increased by a factor of 1.7 when increasing average filler particle size from <10 μm to <149 μm [29].
Still, dispensing technology and packaging sizes restrict the possibilities of increasing filler particle size. Therefore, higher conductivity is mainly achieved by increasing filler contents.
The influence of non-perfect interfaces can be taken into account by a so-called constriction resistance, which then depends on the actual contact area and the distance of interfacing materials. This resistance governs the total resistance of the thermal path [29].

Figure 10: Ag-particles forming a conducting path through the adhesive epoxy (after [29]).

3.3.9 The Heat Equation

If the thermal properties of the materials are known, the temperature distribution can be calculated numerically. The equation that describes heat conduction is the heat equation.
Within a volume the energy needs to be conserved, so the time derivative of the heat needs to equal the spatial derivative of the heat flux. Hence, the heat equation is the continuity equation

$$\frac{\mathrm{d}Q}{\mathrm{d}t} = -\nabla\vec{q} = \nabla \cdot (\kappa \nabla T) \tag{3.62}$$

The heat $\mathrm{d}Q$ will create a temperature change that is given by

$$\mathrm{d}Q = \rho c_p \mathrm{d}T \tag{3.63}$$

When including heat generation inside the volume Q and heat change due to convection with flow velocity $\vec{u}$ (with $\vec{u} = 0$ inside the package), the whole equation can be stated as

$$\rho c_p \frac{\partial T}{\partial t} + \rho c_p \vec{u} \cdot \nabla T = \nabla \cdot (\kappa \nabla T) + Q \tag{3.64}$$

4 Finite Elements Simulations

Finite elements simulations (FEM) are today's standard approach for solving (partial) differential equations (PDEs). They are used in many disciplines like electromagnetics, solid and structural mechanics, fluid dynamics, acoustics, and thermal conduction. The main concept is to divide the domain of the function into elements of finite size and to solve the PDE at this elements' vertices or edges. The main advantage of this method is the ability to deal with complex PDE domain geometries by solving the equations on unstructured grids like tetrahedrons in 3D. Especially curved objects are hard to represent on Cartesian grids of finite difference methods (FDTD). Still, in comparison to these methods, solving a system of higher order elements with the same number of cells using FEM requires more resources (CPU time, memory), since a linear system of equations needs to be solved in order to update the solution.

4.1 Galerkin's Method

In the finite elements method the form of the sought function is controlled by function values at nodal points (node-based) or edges of the cell (edge-based basis functions, which are used for vector fields, since they can overcome obstacles in continuity requirements and boundary conditions more easily for these problems). The approximating function is expressed as a linear combination of basis functions $N_i^e(x)$ weighted by nodal coefficients u_i^e [30]:

$$u^e(x) = \sum_{i=1}^{p} u_i^e N_i^e(x) \tag{4.1}$$

i numbers the node and p the number of nodes of the element e.
For eq. 4.1 to be valid for any node, the basis functions need to be orthonormal. These functions can be linear, polynomials of any order (polynomial basis functions), or even functions of any shape. But the computational cost will strongly depend on their choice.

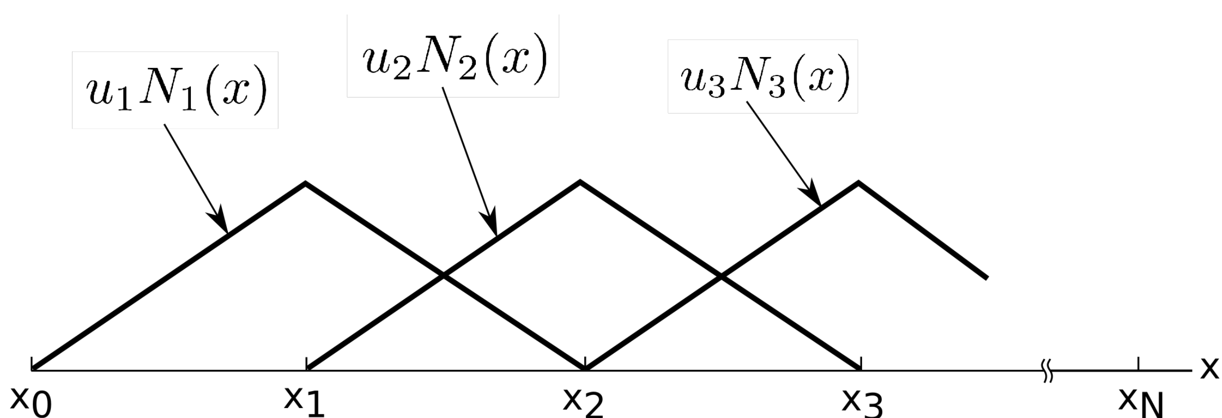

Figure 11: Linear ("rooftop") basis functions with unit magnitude at the nodal points and linearly decreasing to vanish at the neighboring nodes.

In so called weighted residual methods not the PDE itself is solved at every node (Point matching method), but the integral of a weighted residual $R(x) = u(x) - f(x)$ (of a PDE $u(x) = f(x)$ with known $f(x)$) over the domain m of the weighting function:

$$\int_m W_m(x)R(x)\mathrm{d}x = 0 \tag{4.2}$$

In Galerkin's method these weighting functions equal the basis functions $N^e(x)$ used in eq. 4.1 and as a consequence the PDE separates into a system of linear equations, one for each basis function. This system then can be cast into matrix form

$$\left[A^e_{ij}\right]\left[u^e_j\right] = \left[b^e_i\right] \tag{4.3}$$

with

$$A^e_{ij} = \int N^e_i(x)N^e_j(x)\mathrm{d}x \tag{4.4}$$

and

$$b^e_i = \int f(x)N^e_i(x)\mathrm{d}x \tag{4.5}$$

which can be solved for u by inversion.
The computational cost and quality of the approximate solution depends on the quality and number of elements. The discretization of the geometry - also known as meshing - is a difficult task and its control is an important feature of FEM programs and pre-processors.

4.2 Time Dependent Simulations

When time dependent PDEs need to be solved, the equations are solved at every defined time step. Still, the solution can be calculated explicitly for each step (eq. 4.8) or implicitly using the previous time step (eq. 4.9). This is possible using a discrete approximation for the time derivative

$$\frac{\mathrm{d}}{\mathrm{d}t}f(t) \approx \frac{f(t+\Delta t) - f(t)}{\Delta t} \tag{4.6}$$

and the substitution

$$\frac{\mathrm{d}}{\mathrm{d}t}f(t) = g(t, f(t)) \tag{4.7}$$

Then for the explicit case the so-called Euler method is defined as

$$f(t+\Delta t) \approx f(t) + \Delta t g(t, f(t)) \tag{4.8}$$

and for the implicit case (Backward Euler method)

$$f(t) \approx f(t-\Delta t) + \Delta t g(t, f(t)) \tag{4.9}$$

where $f(t)$ depends on itself.

Explicit methods are not as stable as implicit ones. But they offer easy parallelization and, hence, high performance for large models, non-linear effects, and short time frames, since small time stepping is necessary for stable solutions.

4.2.1 The Backward Differentiation Formula

Equation 4.9 is a special case (order 1) of the so-called Backward Differentiation Formula (BDF). The BDF is an implicit method that approximates the function $f(t)$ by a polynomial in the Lagrangian basis [31]

$$p_j(t) = \prod_{k=0,k\neq j}^{s-1} \frac{t - t_k}{t_j - t_k} \qquad j = 0, 1, ..., s-1 \tag{4.10}$$

which has the property

$$p_j(t_l) = \delta_{jl} \tag{4.11}$$

Then $f(t)$ is approximated as

$$f(t) \approx P_{s-1}(t) = \sum_{j=0}^{s-1} p_j(t) f(t_j) \tag{4.12}$$

s defines the order of the algorithm and as a consequence the quality of the approximation at the cost of computational resources. It can be shown that BDF6 is the highest order algorithm that is still stable. For time dependent simulations conducted in this work, the Backward Differentiation Formula using second order Lagrangians was applied. The function at position $n+2$ is then defined via

$$3y_{n+2} - 4y_{n+1} + y_n = 2hf(t_{n+2}, y_{n+2}) \tag{4.13}$$

with step size h and y_n the solution at time t_n. The usage of the Lagrange basis reduces the computational effort. Still, BDF algorithms are not the fastest to choose but are very commonly used due to their high numerical stability.

The non-linear implicit formula, eq. 4.13, is then solved using, for example, Newton's method. More information on the finite elements method can be found in references [32] and [33].

5 Experimental Setup

5.1 Devices Under Test

In this work two devices under test (DUT) were investigated: A position sensor and an infrared spectrometer.
The AS5171 is a high-resolution on-axis magnetic angular position sensor based on a Hall sensor technology (CMOS) and is already on market. The magnetic field component perpendicular to the Hall sensor array is converted into a voltage. It exhibits a 14-bit resolution and is built for automotive applications like sensing of brake and gas pedal position, steering angle, fuel-level, etc. The device is an integrated solution provided in a SiP package (System in Package).

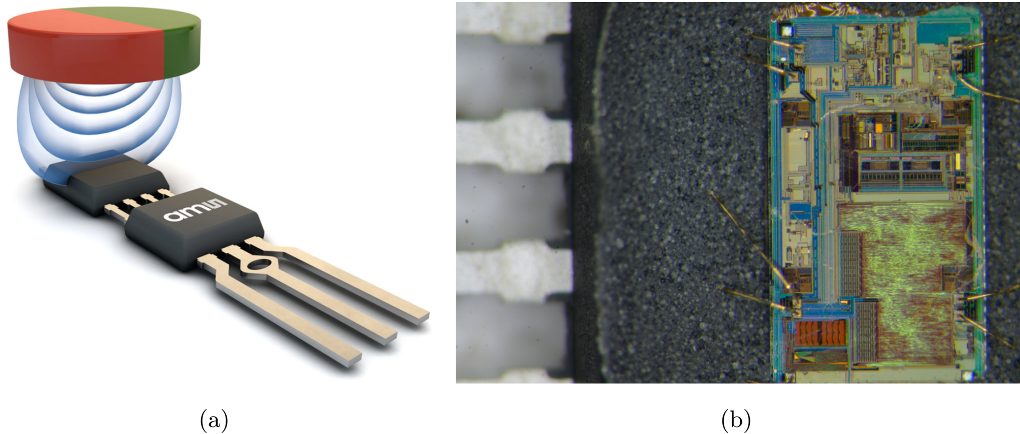

(a) (b)

Figure 12: (a) Drawing of the AS5171 SiP (System in Package) package, (b) open package, die surface, and bonding wires.

The second device is a 6-channel near infrared spectrometer for wavelength from 600 to 1000 nm. The six diodes are covered with a multilayered interference filter. It may be used for multiple purposes like LED light illumination trimming. It is provided in a 20-pin optical land grid array (OLGA) package.

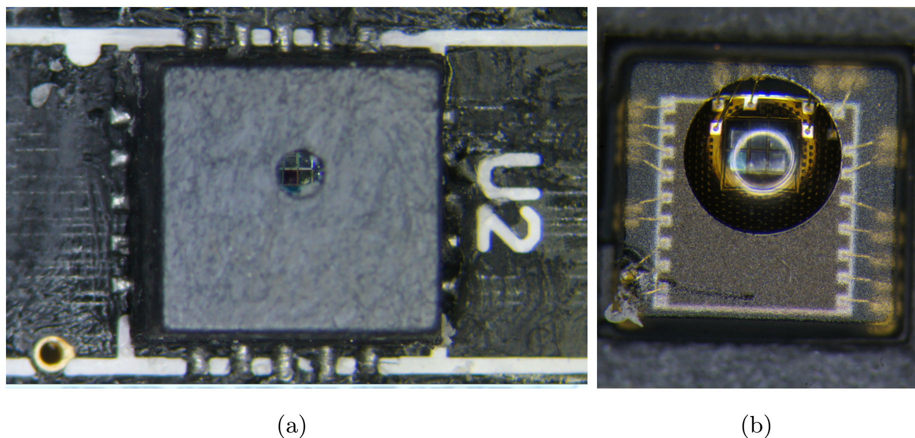

(a) (b)

Figure 13: (a) Top view onto the OLGA package mounted onto a PCB, (b) top view onto the clear mold compound of the device.

Further details of the structure of the packages are described in section 6.1.

5.2 Measurement Environment

The concept of the experiments is to heat up the devices by powering electrostatic discharge protection (ESD) diodes at different positions on the die surface and to measure the temperature. The temperature measurement was done using the linear temperature characteristic of the voltage of a pn-junction while driving a constant current. This is explained in more detail in section 5.2.4. To measure the temperature in the SiP package also an ESD diode was used, while for the OLGA package the temperature was measured using a bipolar junction transistor. Although the more accurate measurement with a bipolar transistor would also be possible in the SiP package, its usage requires the chip to run in a special test mode, where the power dissipation across the die is not exactly known. It should be mentioned that inaccurate modeling of this effect, falsified many simulation results and was a major drawback of this work.
Both temperature measurement concepts are implemented in the integrated circuit, meaning at the die surface, therefore, no temperature sensing in further device layers is possible. This problem of a lack of three dimensional sensing possibilities will be discussed in the conclusion section (section 10).

5.2.1 Ambiance Conditions

To perform reliable measurements, a controlled environment is necessary. This is a challenge for thermal measurements, since it is impossible to create a system that is isolated from the environment. Temperature stabilization can be achieved using a climate chamber. In our experiments the Vötsch® VT 4002 climate chamber was used, which is depicted in figure 14.

Figure 14: Vötsch® VT 4002 climate chamber used to control ambiance conditions.

In this tool the temperature is stabilized by constant fan rotation to distribute the temperature-controlled air all over the measurement chamber. This approach cannot achieve a perfect tem-

perature distribution and creates temperature differences as high as 1 K also after 20 minutes of tempering. Furthermore, the forced convection created by the fan causes turbulent air flow that can only be modeled in finite element simulations at very high computational costs. And of course, the initial air flow at the fan needs to be known, which is not the case. The JEDEC standard for thermal impedance measurements suggests a closed case inside the climate chamber with dimensions bigger then the chamber available for our measurements. A smaller case would result in heating up of the whole case and hence biased results. To overcome this contradiction the climate chamber was turned off during the actual measuring time and the temperature evolution was recorded at a position 4 cm above the device surface. Such a temperature profile can be seen in figure 15.

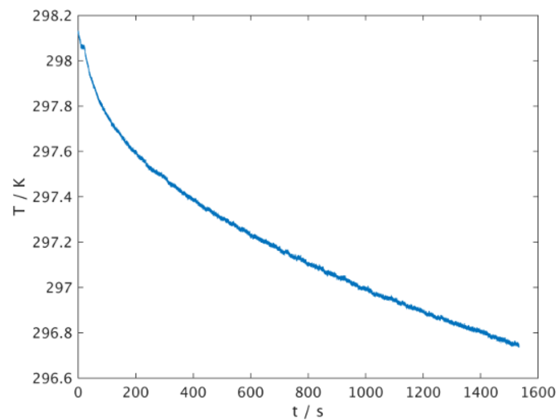

Figure 15: Temperature development inside the climate chamber, 4 cm above the DUT surface.

One further root cause for errors is the internal temperature sensor of the climate chamber, that gives differences to Pt100 temperature measurements as high as ±0.7 K (fig. 16a).

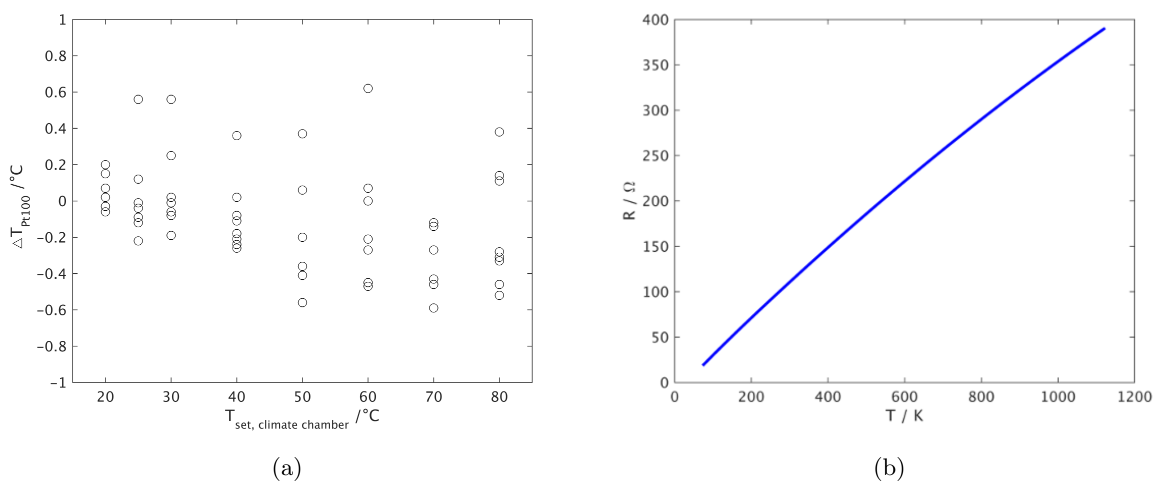

Figure 16: (a) Vötsch® internal temperature sensor temperatures in comparison to Pt100 temperature measurement after settlement time of at least 20 minutes, (b) temperature characteristic of a Pt100 class A resistor.

Knowing the exact ambiant temperature is crucial for thermal experiments. Approaches using

type K thermocouples resulted in diode temperature characteristics with error margins too high for a reasonable inverse modeling approach. Temperature measurement using Pt100 class A resistors on the other hand is a very reliable method. The measurement temperature is calibrated using the temperature dependent resistivity of platinum (fig. 16b) which gives a very small measurement error of 0.15°C + 0.002 T/°C compared to that of a type K thermocouple ($\geqslant \pm 1.5$°C). When using Pt100 resistors for temperature measurement, Joule-heating of the resistor needs to be considered. Therefore, a voltage measurement, while driving a current of 100 μA was used. The voltage on the Pt100 resistors was measured by four-terminal sensing (Kelvin sensing) where the current carriage and voltage sensing is done on separate pairs of wires to eliminate the resistance of the leads. The wires to the voltmeter hardly carry any current, resulting in very accurate resistance measurements. The Kelvin measurements were done using a KEITHLEY 2601B SYSTEM SourceMeter®.
Both, the SourceMeter and the climate chamber, were controlled using a Python code that addresses the devices per TCP/IP. The code is attached in the appendix.

5.2.2 Device Preparation

The SiP package is a package that can be mounted to its final location just by soldering wires to its leads. No printed circuit board is needed and the package can be suspended by its leads. The device was attached onto a 4.5 mm high FR4 frame that fixed the device on the leads and left the molded parts with direct contact to ambient air. The construction can be seen in figure 17. A ribbon cable was soldered onto the 8 leads to connect the device to a custom measurement system for device testing (BMS).

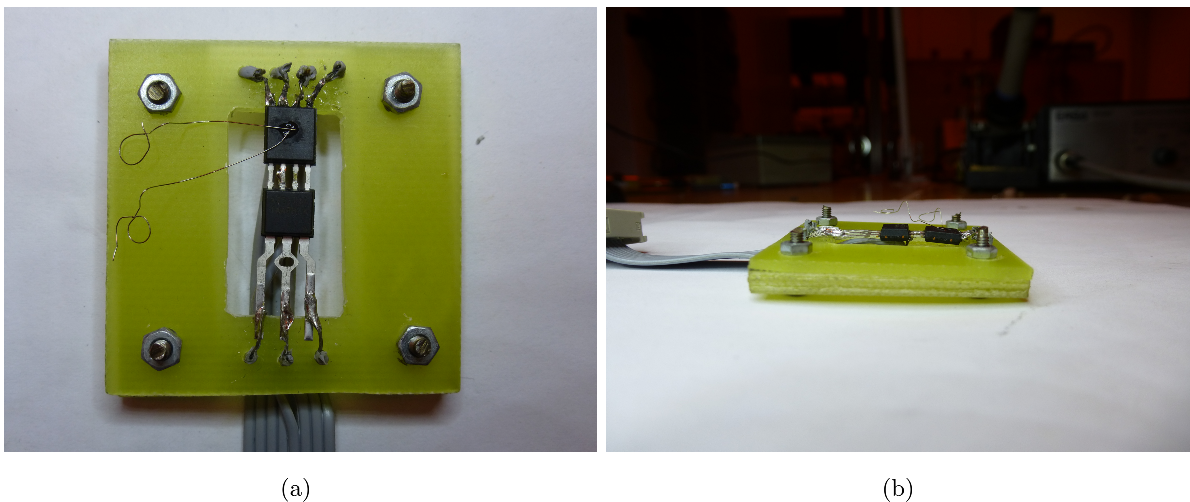

(a) (b)

Figure 17: Measurement construction for the SiP package. (a) Top view, (b) side view.

The OLGA package is a surface mounted device (SMD) that has all its contact pads on the bottom side of the substrate. It therefore needs to be mounted onto a printed circuit board and a ribbon cable was attached to its 20 pins. The device can be seen in figure 18.

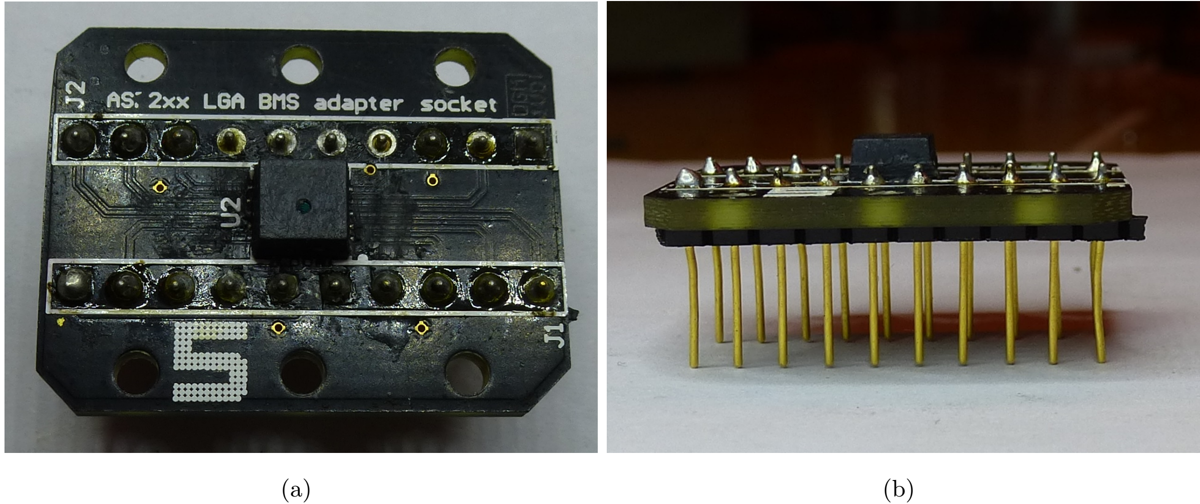

(a) (b)

Figure 18: Measurement construction for the OLGA package. (a) Top view: the small rectangular package in the middle soldered onto a printed circuit board, (b) side view

For isolation both device constructions were put onto a FR4 board that was lifted by 1.5 cm above the climate chamber ground.

5.2.3 Infrared Camera Setup

To obtain information on the devices' surface temperature, an optris® PI 160 infrared camera was mounted above the devices (figure 19). The camera offers a 25 x 25 μm 160 x 120 pixel focal-plane array with a frame rate of 120 Hz. Each of these pixels contains a microbolometer, which is an uncooled silicon temperature sensor: A readout IC on a silicon substrate measures the temperature change of an IR absorbing material (that is thermally isolated from the IC). The spectral range of the camera reaches from 7.5 to 13 μm and gives a temperature accuracy of $\pm$2 K. The used 23° x 17° FOV optic with a focal length of 10 mm reaches a thermal sensitivity of 0.08 K.

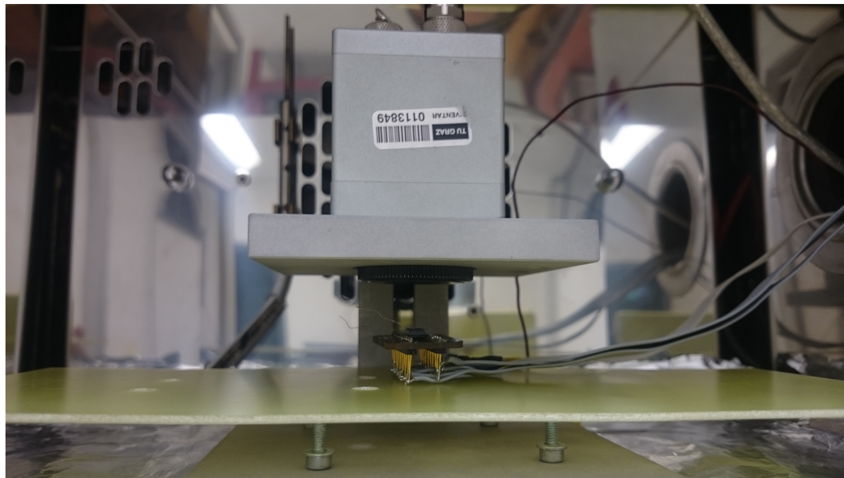

Figure 19: optris® PI 160 infrared camera mounted above the devices inside the climate chamber.

5.2.4 ESD Diode Measurements

5.2.4.1 The temperature dependence of forward biased pn-junctions

The current of a diode follows the characteristic [34]

$$I = eA\left(\frac{p_{n0}D_p}{L_p} + \frac{n_{p0}D_n}{L_n}\right)\left(\exp\left(\frac{eV}{k_BT}\right) - 1\right) \tag{5.1}$$

with e the elemental charge, p_{n0} the temperature dependent concentration of holes on the n-side far away from the junction, n_{p0} that of electrons on the p-side and L the corresponding diffusion lengths. This relationship shows an almost linear voltage dependence on temperature at a constant current for a specific temperature range. This measured behavior can be seen in figure 20 for the two devices under test.

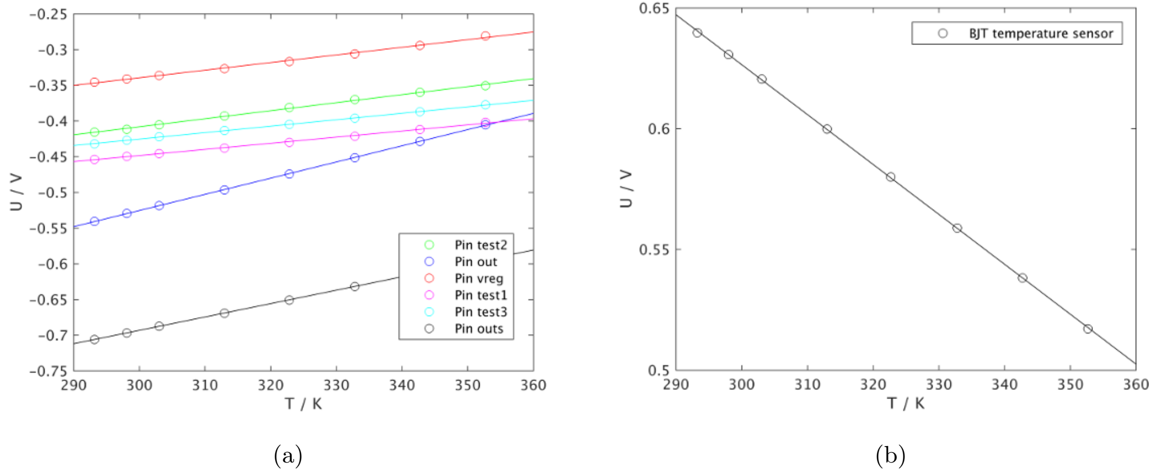

(a) (b)

Figure 20: Measured U-T characteristic of (a) the ESD protection diodes of the SiP package and (b) the BJT temperature sensor of the OLGA package. The voltages are averaged over 5 runs.

The resulting characteristic fits of the diodes used are as followed. The positions of the junctions can be seen in figure 21a for the OLGA and figure 21b for the SiP package.

$$T_{OLGA}/K = (U/V - 0.6815)/(-0.0021) + 273.15 \tag{5.2}$$

$$T_{SiP}/K = (U/V + 0.5901)/0.0023 + 273.15 \tag{5.3}$$

5.3 Heating Configurations

The experiments were conducted using the most stable ESD diodes for heating. The maximum current through one diode was limited to 90 mA. To gain diverse information, five different experimental approaches were used:

- Heating of 1 ESD diode (D1) @ 90 mA.
- Heating of 2 ESD diodes (D1, D2) @ 90 mA.
- Heating of 3 ESD diodes (D1, D2, D3) @ 90 mA.

- Heating of 3 ESD diodes (D1, D2, D3) @ 70 mA.
- Heating of 3 ESD diodes (D1, D2, D3) @ 50 mA.

The positions of the heated diodes of the OLGA device, referred to as D1, D2, and D3, can be seen in figure 21a. The diodes are located in close proximity around the pads. In the model, the heated boundaries are set on the wire-bond-to-die interface.
The BJT temperature sensor is located at the red marked spot.

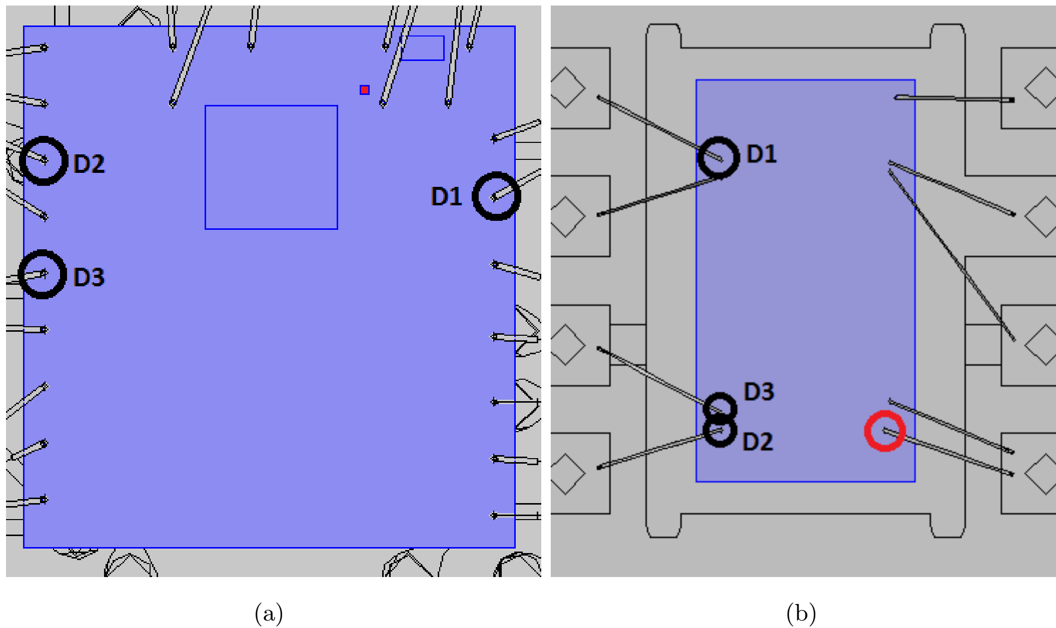

(a) (b)

Figure 21: Positions of the heated ESD diodes at the interface between wire bond and die (blue). The location of the temperature sensor is marked in red. (a) OLGA package. (b) SiP package.

Figure 21b shows the three diode positions as well as the position of the diode used for temperature measurement for the SiP package experiments.
The diodes were heated to achieve constant power dissipation. The different step functions can be seen in figure 22.

The concepts described in this chapter - the heating of ESD protection diodes and the temperature measurements at the dice and packages' surfaces - were the basis for finite elements simulations that attempted to reproduce experimental results. The corresponding concept will be described in the following chapters.

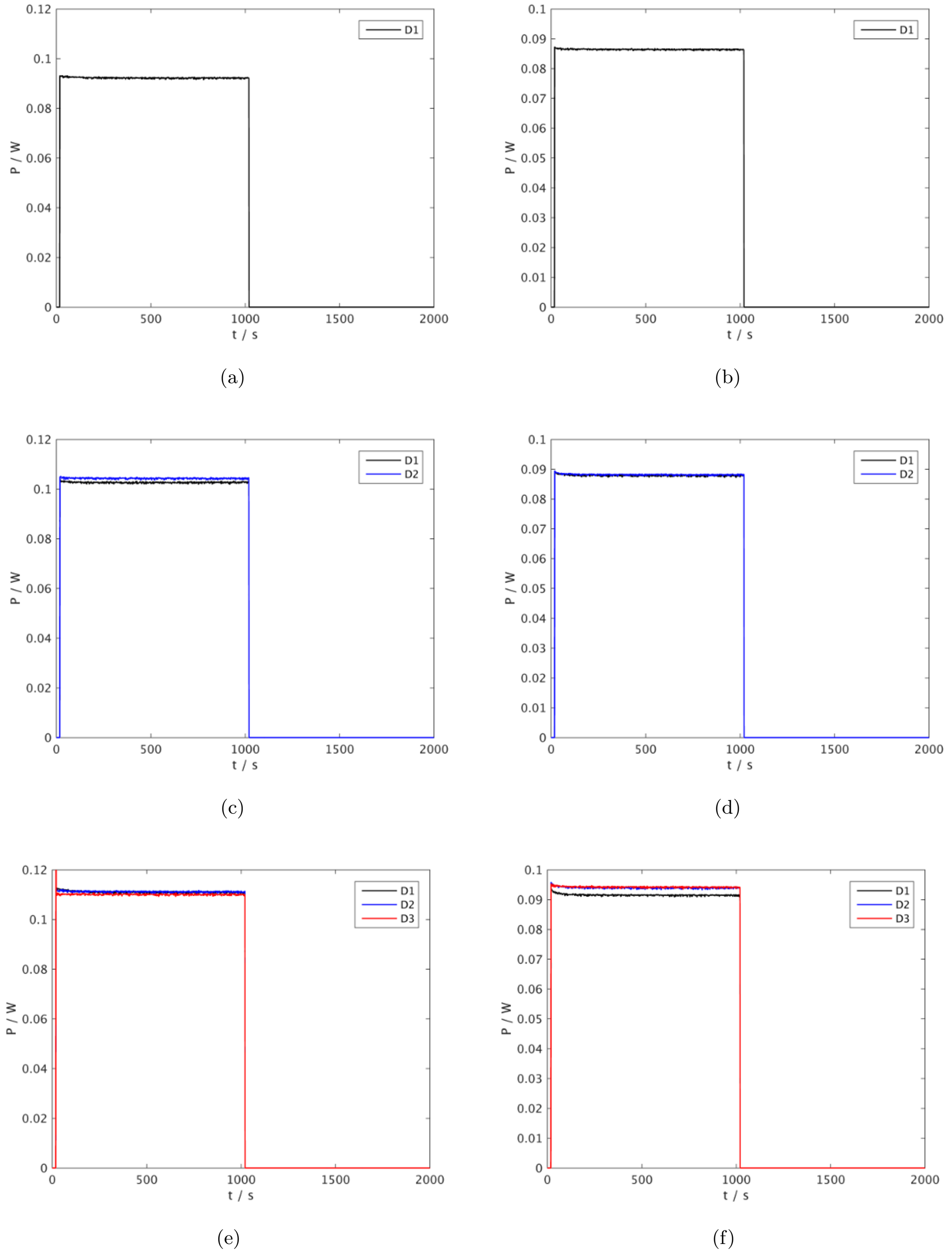

Figure 22: Power dissipation configurations of (a,b) 1 diode heating, (c,d) 2 diode heating, (e,f) 3 diode heating. For the OLGA package (left column) and for the SiP package (right column).

6 Simulation Setup

6.1 CAD Models

The simulation models were set up using the software SolidWorks 2015 from Dassault Systèmes. In a first step the existing basic device models were extended by bonding wires, substrate drills, fingers, and leads. Then the whole model was extended to fit the experimental setup.
Figure 23 shows the comparison between the OLGA package cross section of the real device (a) and of the simulation model (b). The package consists of a die (light gray) with the integrated circuit processed at the die surface. This multilayer IC is passivized by a SiO_2 and a Si_3N_4 layer. These leave direct contact for the I/O contact pads that are connected to the substrate (blue) by Au wire bonds. The sensing diode structure is overmolded by a lens shaped compound, mainly consisting of epoxy resin and acid anhydride (beige). The whole structure is protected by a liquid crystal polymer (LCP) cap (dark gray) that leaves a cavity above the clear mold. The die attach consists of epoxy filled with silver particles and connects the die with the substrate.

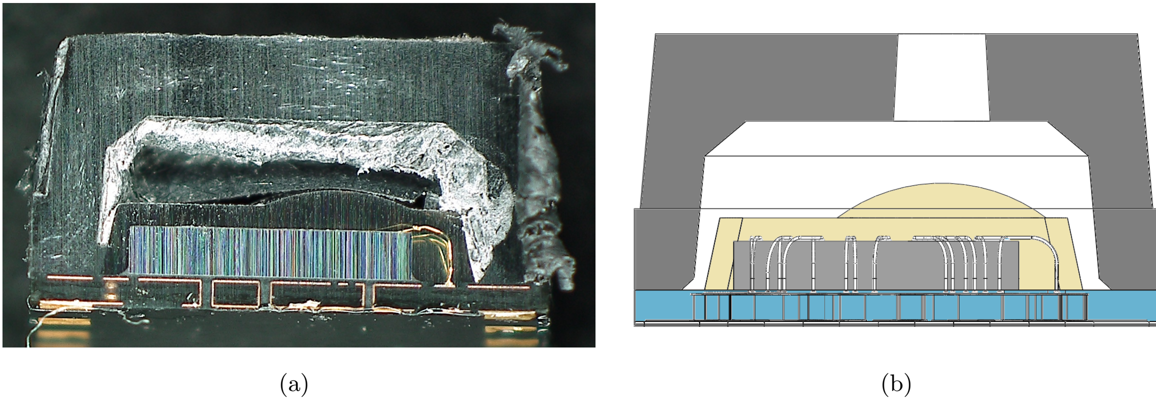

(a) (b)

Figure 23: (a) Light microscope picture of the cross section of a cut device and (b) corresponding view of the CAD model of the OLGA package.

In the first try, the measurement construction (figure 18) was modeled using a simplified geometry where the PCB was modeled uniformly without conducting paths through the PCB to the pin positions. The paths were implemented as direct connection from the leads on the bottom side of the substrate vertically through the PCB. There, the copper domain was extended by the length of the pins which were then extended horizontally to form the soldered ribbon cable (figure 24a).
Figure 25 shows the added substrate structure that connects the wire bonds to the leads on the device bottom side. This very accurate model is at the cost of higher computational effort, but is necessary to include proper dimensions of the metallic fraction of the substrate that forms its main heat conduction path.

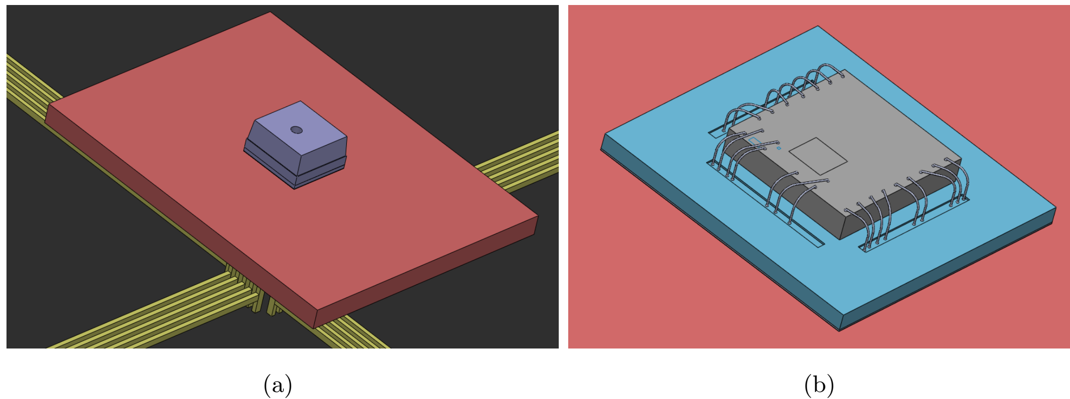

(a) (b)

Figure 24: CAD model of the OLGA package. (a) The device mounted onto a printed circuit board (red) and connected by pins and wires. (b) The substrate (blue) and the die (gray).

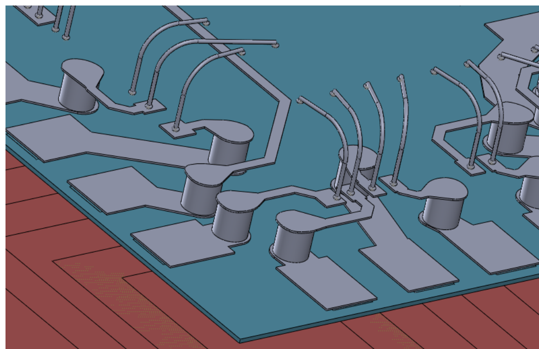

Figure 25: Modeled substrate structure of the OLGA package.

In figure 26 the comparison between the cross section of the real SiP package and of the simulation model is shown. The SiP package is a system solution that consists of two package bodies. One covers the die with the actual IC, the second encloses three capacitors that work as filters. The package itself is a custom solution where the die (light gray) is attached with a conductive adhesive (with Ag-particles) to the lead frame (yellow). The latter connects both packages and makes the devices mountable into its final position without the need of a PCB. The mold compound (dark gray) surrounds both parts, the IC part and the filter part, completely and the I/O pads on the die surface are wire bonded to the leads. The die is passivized by a SiO_2 and a Si_3N_4 layer and additionally protected by a polyimide layer.

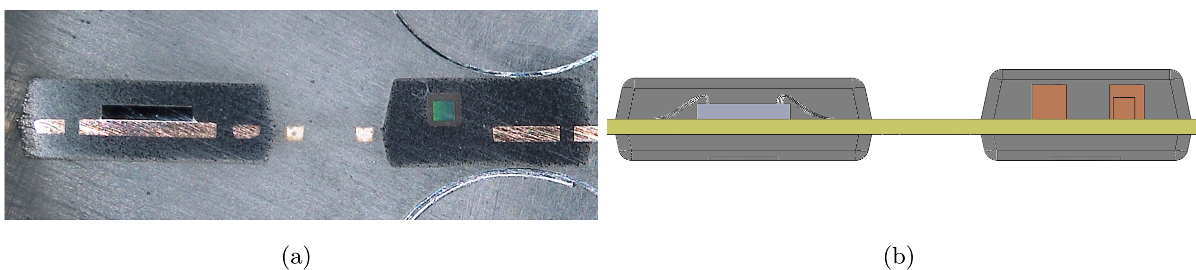

(a) (b)

Figure 26: (a) Light microscope picture of the cross section of a cut device and (b) corresponding view of the CAD model of the SiP package.

The construction explained in figure 17 realized as a CAD model is shown in figure 27a.

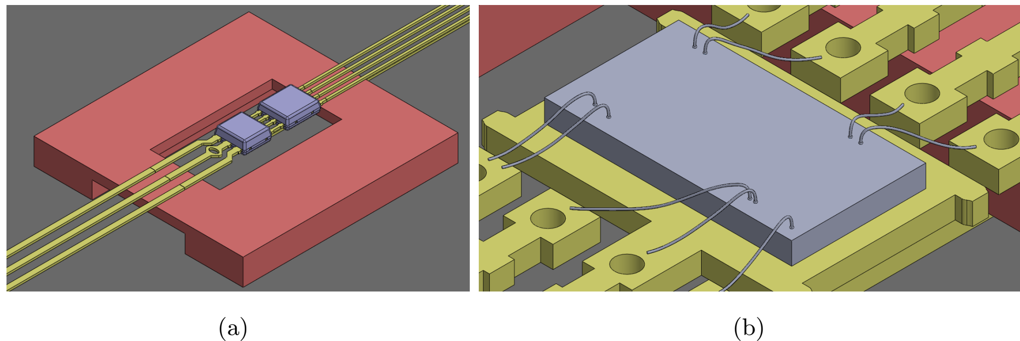

(a) (b)

Figure 27: CAD model of the SiP package. (a) The device (violet) is attached onto a FR4 construction (red). A ribbon cable is soldered onto the leads (yellow). (b) The lead frame (yellow) and the die (gray) are connected by wire bonds.

6.2 Simulation Assumptions

The finite elements simulations were performed using COMSOL Multiphysics® software (v5.2) including the Heat Transfer Module by MathWorks, Inc.
The CAD models were meshed using a free tetrahedral mesh. Due to the fine geometry of the wire bonds and the conducting path in the OLGA substrate, both devices consist of about one million nodes. The size of the air domain was defined as the size of the climate chamber and the measured ambient temperature was set as a fixed temperature boundary condition to the air domain boundaries. To reduce the overall domain size, a sweep of the size of the air domain was done. The model size was reduced in order to not influence the results of simulations of the experiments.
Since it eases meshing, the models include geometric simplifications, like the cross section of the soldered cables that follows that of the leads or pads. Therefore, the thermal conductivity was adapted correspondingly. The die attach, capacitor solder, and passivation layers are all modeled as two dimensional thin films that do not have heat capacity.
For thermal simulations, the heat equation (eq. 3.64) is solved. Mass density, specific heat at constant pressure, and thermal conductivity are assigned to the used materials. The used materials and their initial properties can be seen in table 1 and 2 of the results section. Most of the material properties that are used as parameters to optimize the simulations were provided by the subcontractor. It is not known how these properties were measured and how they are influenced when the materials are actually processed. Also, company internal measurements on various materials properties show the potential of large deviations from provided supplier values.

7 Design of Experiment

7.1 Response Surface Design

The approach of inverse modeling of materials parameters in order to fit simulation results to experiments requires a quantification of the quality of the results. Since the parameters influence each other, the optimization needs to be qualified by a suitable design of experiment. A common approach is to define a parameter space of the dimension of the number of parameters to optimize and to perform experiments at specific points in this space. The result creates a response at each of these points that is fit using a second order polynomial. The minimum of this resulting response surface gives the optimal parameters. Depending on the available resources different designs are used. The most common ones are a central composite design or a Box-Behnken design. In both, a range for all parameters is defined. The first option requires experiments at all corners of the parameter space, at the parameter space center, and at axial points where one parameter is out of the defined range while all the others are set to their central values.
The Box-Behnken design only uses response values at the edge centers and does, therefore, need less experimental runs.

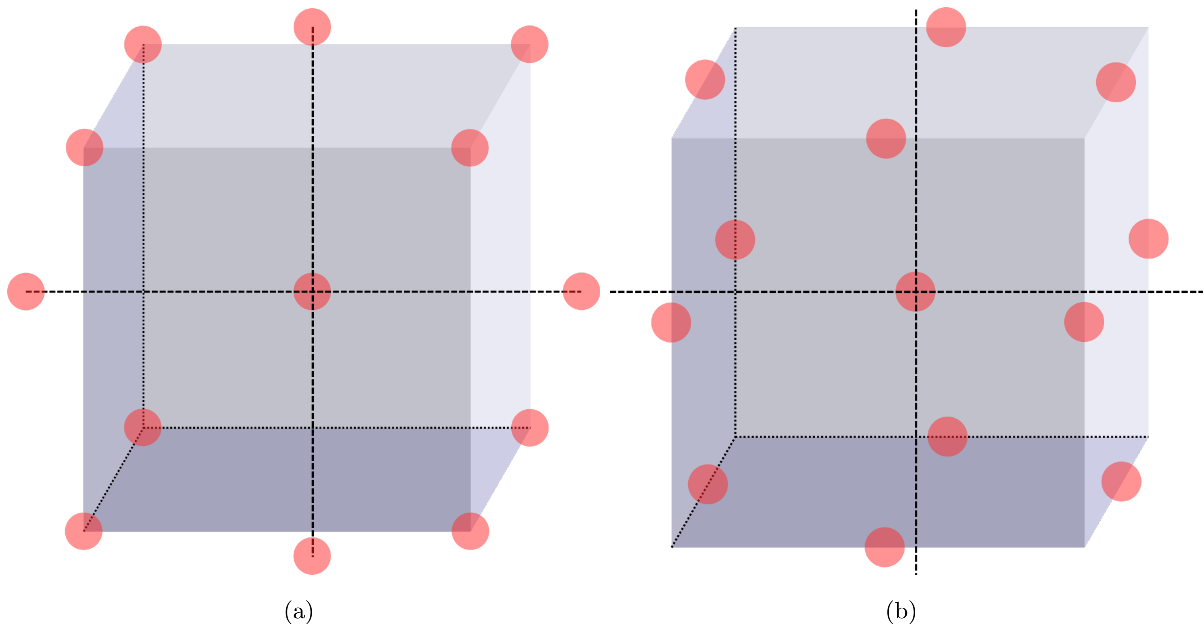

Figure 28: (a) Central composite design (b) Box-Behnken design for a three dimensional parameter space. The cube's edge is the parameter range and the red dots mark the parameters for experimental runs.

For the simulations done in this work, the Box-Behnken design was chosen due to the lower computational cost and sparse access to simulation licenses. The analysis of the design was done using Minitab 16 Statistical Software.

To be able to define parameter ranges, the response was minimized by optimizing every parameter separately while the remaining parameters were held at their initial values. Then, one Box-Behnken optimization run was performed. The response surface results were used to narrow

the parameter ranges down. Then, the simulation loop was repeated.

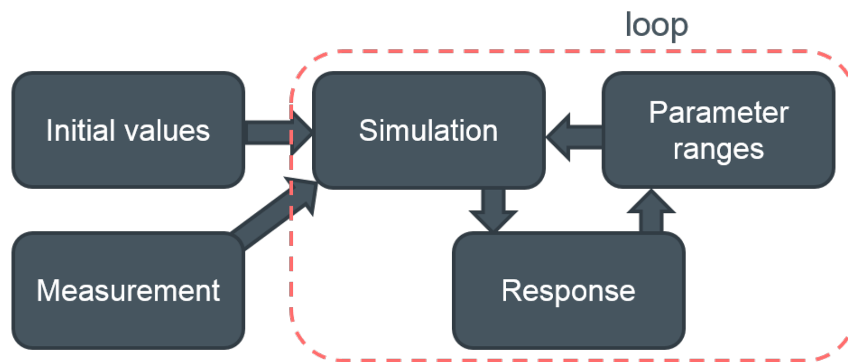

Figure 29: Simulation loop to narrow down parameter ranges.

8 Results

8.1 Measurement Results

The measured temperature evolution of the first three measurement setups described in section 5.3 is plotted in figure 30 for the OLGA package and in figure 31 for the SiP package. The diodes were heated for 1000 seconds so that the final temperature could be assumed to represent steady state conditions. The ambient temperature was set to (25 ± 0.2)°C. This was measured using a Pt100 resistor located 10 cm away from the device and using the devices' ESD diodes itself. The data was averaged over 5 runs per heat configuration.

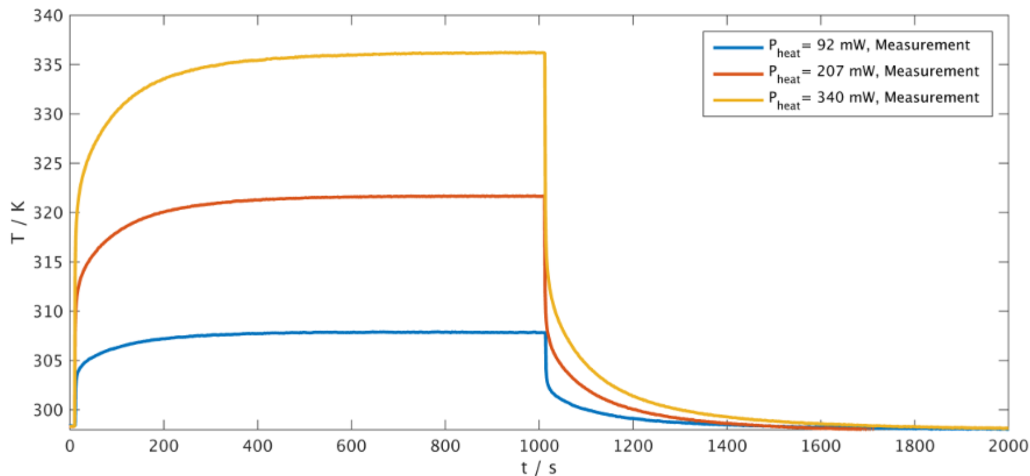

Figure 30: Temperature evolution for three different heat configurations: heating of one ESD diode (blue), two diodes (red) and three diodes (orange). The temperature was measured at the BJT temperature sensor.

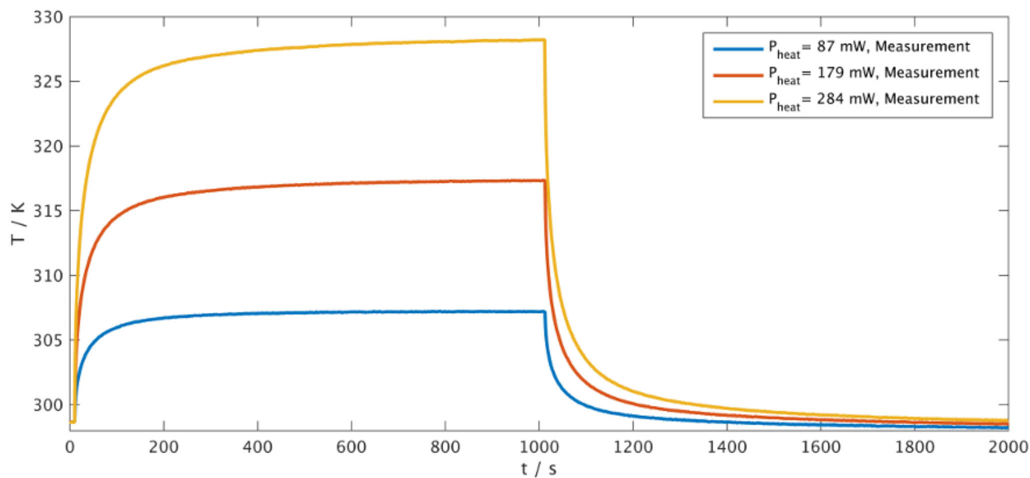

Figure 31: Temperature evolution for three different heat configurations: heating of one ESD diode (blue), two diodes (red) and three diodes (orange). The temperature was measured also at an ESD diode.

A common way to describe heat evolution in microelectronics packaging is to determine the

thermal impedance θ_{JA} between the junction and the ambient environment. It is defined as

$$\theta_{JA} = \frac{T_A - T_J}{P_{diss}} \tag{8.1}$$

with T_J the temperature at the junction, T_A the ambient temperature and P_{diss} the dissipated power.

One can see in figures 32 and 33 that in both cases the thermal impedance deviates for the one diode heat configuration. This can be due to the fact that the location of D1 (see figure 21) is separated from D2 and D3 which are located close to each other. Therefore, the heat path is different and, hence, the thermal impedance. A temperature dependence of the thermal impedance could not be verified in our approaches. It is important to mention that the actual thermal resistance is θ_{JA} in steady state.

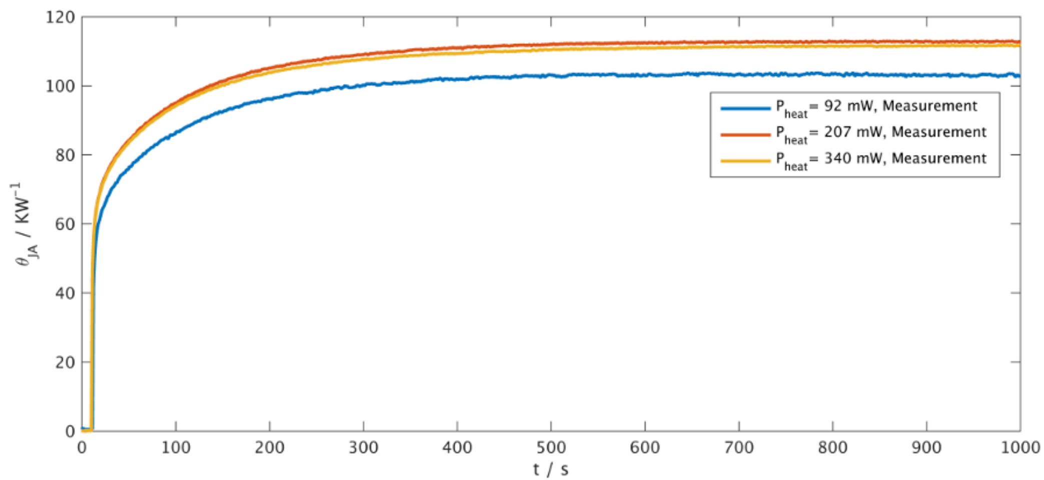

Figure 32: Thermal impedance of the OLGA package.

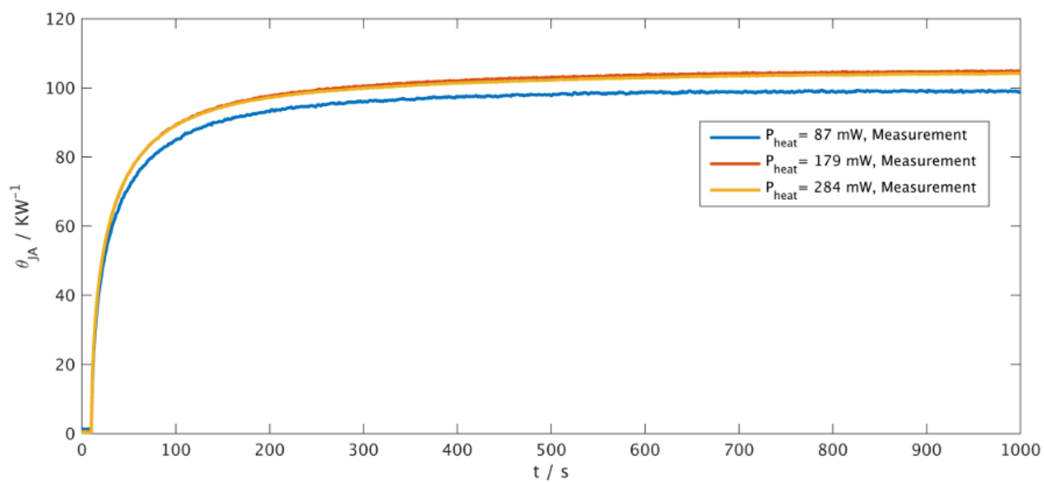

Figure 33: Thermal impedance of the SiP package.

8.2 Emissivity Adjustment

To include radiation into the finite element simulation, the emissivity ϵ of the gray body needs to be known, since it defines the radiated power following eq. 3.1. Therefore the surface temperature of the mold compound and the lid cap were measured by attaching a NiCr-Ni thermocouple onto the top of the device package and by an infrared camera at the same time. The first attempts at measuring surface temperatures using Pt100 resistors failed, since the resistor conducted too much heat. As a consequence, a repetition of the experiment without the attached resistor resulted in too high temperature values at the IR camera read out while having the emissivity already set to the maximum black body value of 1. The NiCr-Ni thermocouple was calibrated using a 0°C reference, realized by a Dewar vessel filled with pure ice water. The temperature of the reference was measured using a Pt100 resistor.

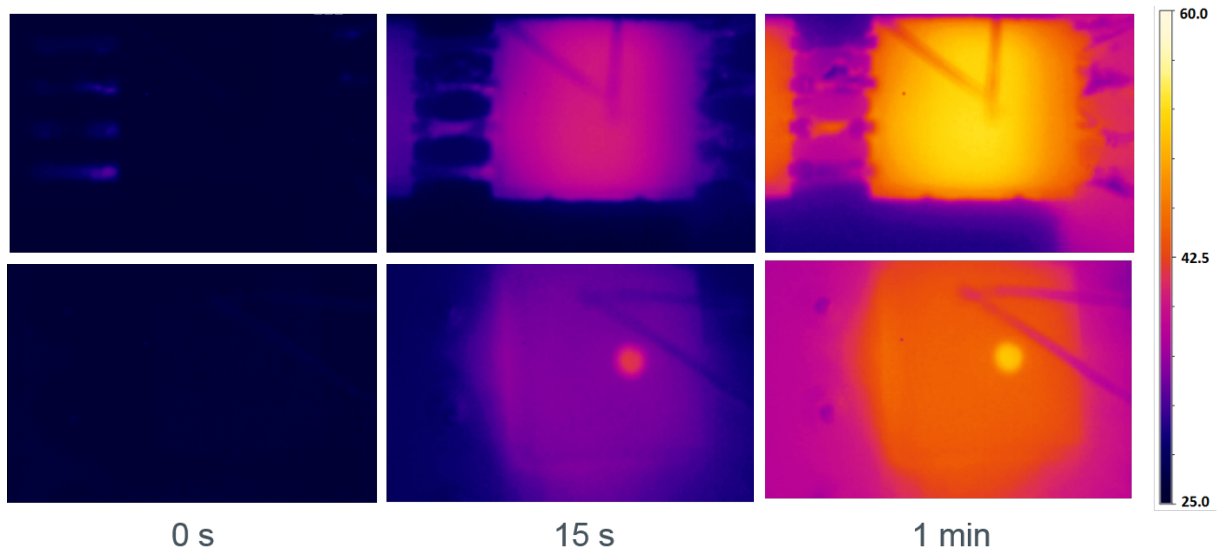

Figure 34: Emissivity estimation using attached NiCr-Ni thermocouples and an infrared camera. Top row: SiP package, Bottom row: OLGA package

The measurement was done using the same heat dissipation setup as described in section 8.4, measuring the temperature over a time window of 1000 seconds. The results are shown in fig. 8.2a and 8.2b. The emissivity values of $\epsilon = 0.85 \pm 0.05$ resp. $\epsilon = 0.84 \pm 0.05$ are fit using a least-squares approximation.

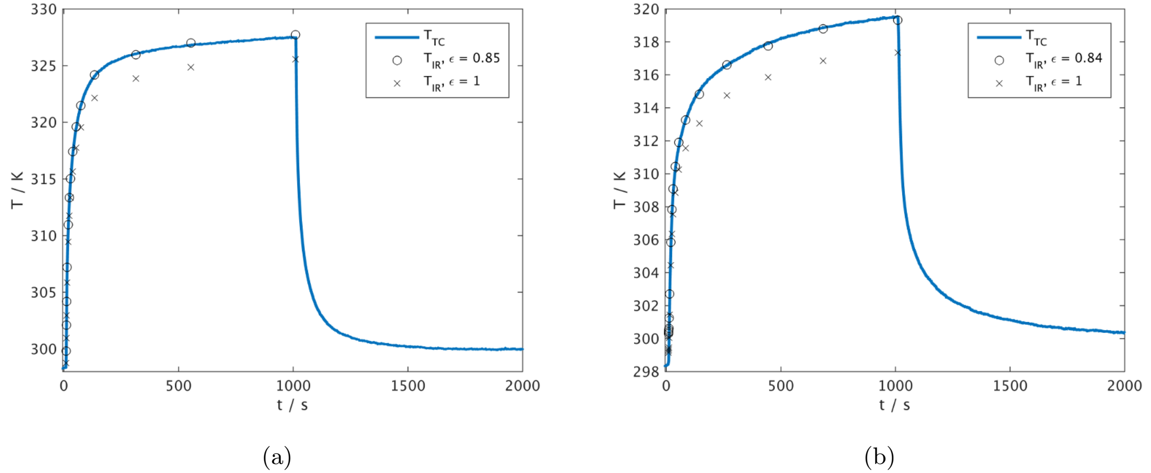

Figure 35: Thermocouple-, black body- and emissivity adjusted surface temperature (a) of the SiP package and (b) of the OLGA package

The Stefan-Boltzmann law was applied onto the top boundaries of the mold compound of the SiP and on top of the lid cap of the OLGA package using the "diffusive surface" feature.
Figure 36 shows that the influence of radiation in the simulation is small and small deviations in the emissivity are even negligible. The temperature difference between the simulation with radiation ($\epsilon = 0.84$) and without radiation is as small as 0.4°C after 1000 seconds of overall 340 mW power dissipation on the die surface. Still, this temperature difference can account for a difference in optimized thermal conductivities as high as one magnitude of the initial parameters, as will be shown in section 8.3.2.

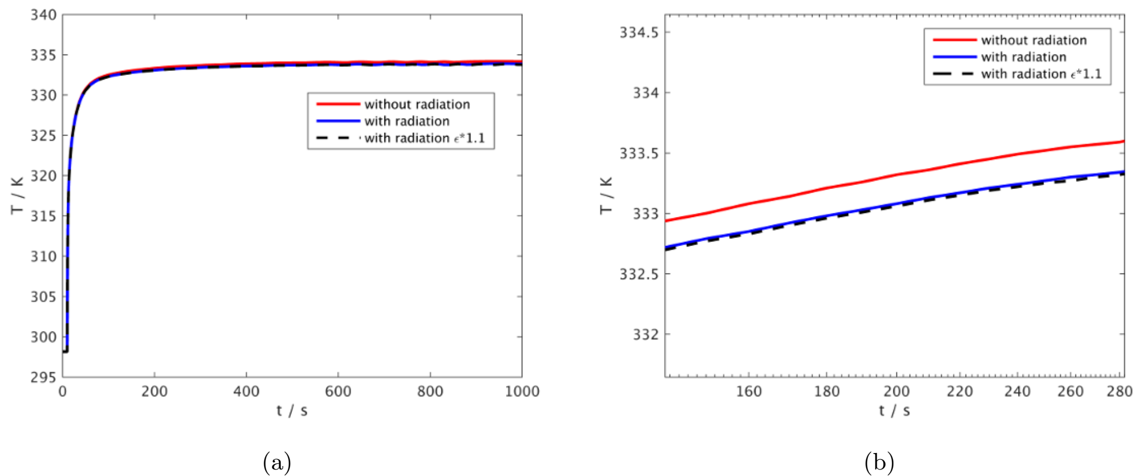

Figure 36: Influence of radiative lid surface on simulation results of OLGA package

8.3 Adjustment of Thermal Conductivity

Initially, an attempt was made to simultaneously optimize values for the specific heat and the thermal conductivity in one time dependent simulation. But to fit the resulting seven dimensional parameter space proved impractical.
As a consequence, to determine the thermal conductivity of the different materials, steady state

simulations were used. In this case, equation 3.64 becomes

$$Q = -\nabla \cdot (\kappa \nabla T) \tag{8.2}$$

and the heat capacities do not contribute to the temperature distribution.

8.3.1 Set Materials Parameters

The materials included in the model as well as their thermal properties are listed in table 1 and 2. When available, temperature dependent properties were used. The properties of the unknown materials are the values provided by the supplier. If a value range was given the initial value was chosen as the mean value.

Table 1: Initial materials parameters of the OLGA package

Component	Material	$\rho/\mathrm{kg \cdot m^{-3}}$	$c_p/\mathrm{J \cdot kg^{-1}K^{-1}}$	$\kappa/\mathrm{W \cdot m^{-1}K^{-1}}$
Leads	Copper	8700 [35]	$c_{p,Cu}(T)$ [36]	$\kappa_{Cu}(T)$ [37]
Wire bonds	Gold	19280 [35]	$c_{p,Au}(T)$ [35]	$\kappa_{Au}(T)$ [35]
Die	Silicon	2329 [35]	$c_{p,Si}(T)$ [36]	$\kappa_{Si}(T)$ [38]
PCB	FR4	1900 [35]	1369 [35]	0.3 [35]
Substrate	Copper clad laminate	1900-2200	1020-1200 [39]	0.8
Clear mold	Epoxy resin, acid anhydride	1170-1230	830-1130	0.2
Die attach	Epoxy resin, Ag particles	1400	950	0.4
Lid cap	Liquid crystal polymer	1590-1630	1000	0.35-0.5

Table 2: Initial materials parameters of the SiP package

Component	Material	ρ/kg · m^{-3}	c_p/J · kg^{-1}K^{-1}	κ/W · m^{-1}K^{-1}
Lead frame	Tin plated copper	8700 [35]	$c_{p,Cu}(T)$ [36]	$\kappa_{Cu}(T)$ [37]
Solder paste	Sn95Sb5	7270 [40]	222.1 [40]	28 [41]
Wire bonds	Gold	19280 [35]	$c_{p,Au}(T)$ [35]	$\kappa_{Au}(T)$ [35]
Die	Silicon	2329 [35]	$c_{p,Si}(T)$ [36]	$\kappa_{Si}(T)$ [38]
Mold	Epoxy resin, phenolic resin, fused silica	1950	810	0.96
Die attach	Epoxy resin, Ag particles	3400	510	2
Construction	FR4	1900 [35]	1369 [35]	0.3 [35]

Plots of the temperature dependent functions can be found in the appendix. Values without reference are supplier values.

8.3.2 Parameter Estimation

First an estimation on the influence of the materials parameters on the measured steady state temperature was done. Therefore a materials parameter sweep of every material whose properties were provided by the supplier was done separately, to get information about

- the influence of a change of the thermal conductivity of the material on the measured steady state temperature
- the parameter range that would be necessary to fit the simulated steady state temperatures to the measured one by adapting just one material's thermal conductivity

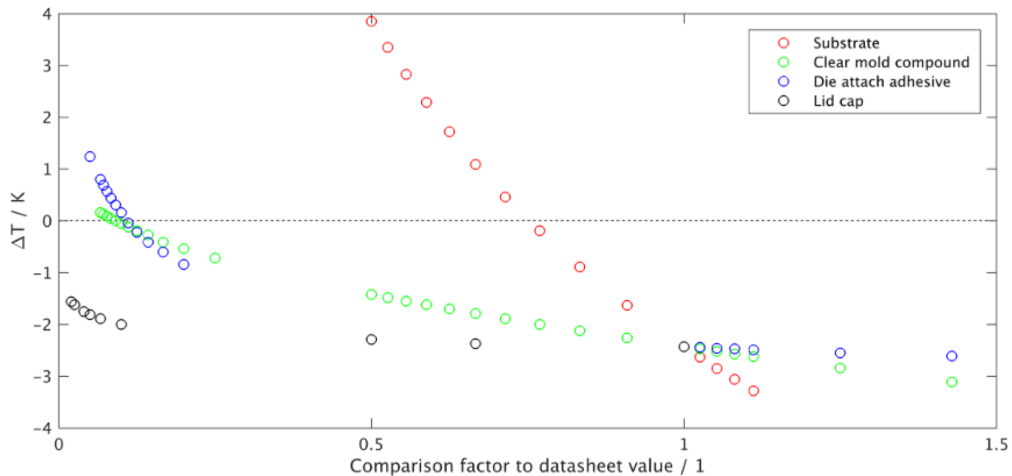

Figure 37: OLGA Package: Influence and parameter range estimation of thermal conductivity of materials under investigation.

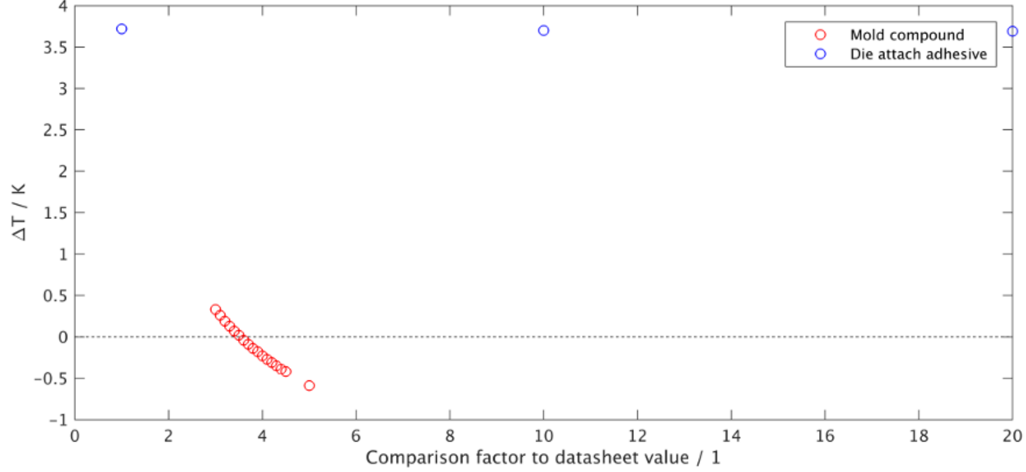

Figure 38: SiP Package: Influence and parameter range estimation of thermal conductivity of materials under investigation.

Figure 37 shows the four components under consideration for the OLGA package: The substrate, the clear mold compound, the die attach epoxy and the LCP lid cap. The comparison factor describes the factor by that the supplier provided datasheet values were multiplied. One can see that the thermal conductivity of the substrate is the governing property that achieves the largest deviations in steady state temperature. The influence of the lid cap is negligible for thermal conductivity adaption.
The System in Package consists basically of four materials in the main heat path. The mold compound, the die, the die attach adhesive and the lead frame. The lead frame consists of tinned copper with well known thermal properties. For both devices it is assumed that the die can be modeled as pure silicon which leaves two parameters for the SiP package: the mold compound and the die attach epoxy. As can bee seen in figure 38, the influence of the adhesive can be neglected.

For the optimization of the thermal conductivity, the response was defined as the difference between the simulated and the experimentally obtained temperature in steady state. It was assumed that the experimental steady state temperature was reached when the change in measured temperature was below 0.2 K within 10 minutes.
The first simulation runs of the OLGA package were started using a parameter range of $0.1k_{init} \leqslant k_{test} \leqslant 10k_{init}$ for the clear mold compound and for the die attach epoxy and a range of $0.5k_{init} \leqslant k_{test} \leqslant 2k_{init}$ for the substrate. A Box-Behnken design of experiment with 13 runs per configuration was done for the five heating configurations described above. The resulting response surfaces do not show a unique parameter combination that fits the simulation to the experiment. Therefore the combination that is closest to the initial values was chosen (green dot). This is indicated by the black line. Figure 39 shows contour plots of the response surface exemplary for heat dissipation from 3 ESD diodes with a current of 90 mA through each diode (333 mW total power dissipation).
This first run gave a rough parameter estimation that can be seen in table 3.

Table 3: Parameter estimation for the OLGA package.

Package	Parameter	Comparison factor
OLGA	Substrate κ	0.64
OLGA	Clear mold compound κ	1.07
OLGA	Die attach adhesive κ	0.99

As a consequence a finer adjustment was done confining the parameter ranges to $\pm25\%$ of the found optimum values. For the substrate $0.49k_{init} \leqslant k_{test} \leqslant 0.81k_{init}$, for the clear mold compound $0.80k_{init} \leqslant k_{test} \leqslant 1.34k_{init}$ and for the die attach epoxy $0.74k_{init} \leqslant k_{test} \leqslant 1.24k_{init}$. The response surfaces are plotted in figure 39b,d,f. The resulting comparison factors can be seen in table 4. The errors result out of measurement and response surface regression errors.

Table 4: Parameter estimation with confined ranges for the OLGA package.

Package	Parameter	Comparison factor
OLGA	Substrate κ	0.7 ± 0.3
OLGA	Clear mold compound κ	0.9 ± 0.1
OLGA	Die attach adhesive κ	1.0 ± 0.2

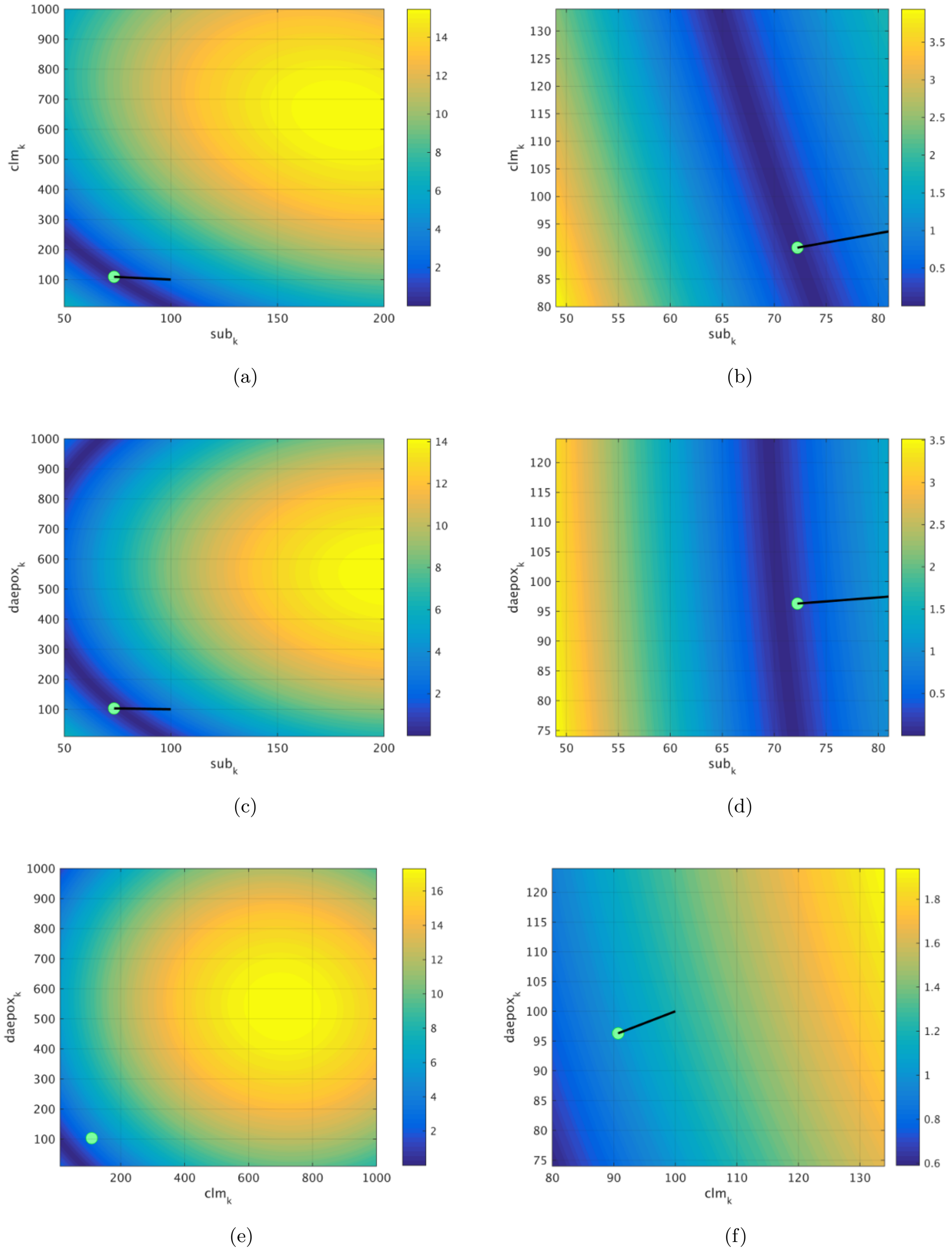

Figure 39: Two dimensional projections of the three dimensional response surface. Demonstrative example with 3 diodes and 333 mW overall heat dissipation. Left column: first run. Right column: second run for finer adjustment.

The steady state temperature deviation of the SiP package was reduced to only the influence of the thermal conductivity of the mold compound. The results of the sweep can be seen in figure 40.

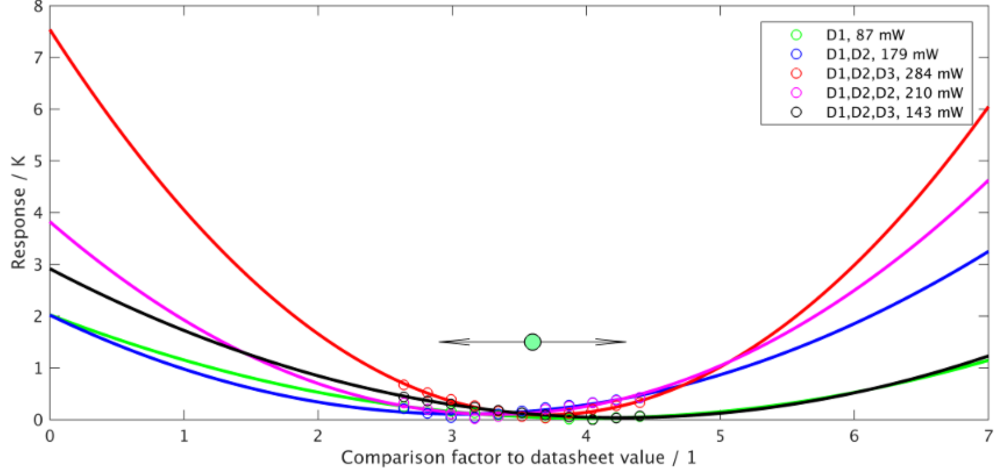

Figure 40: Response of the SiP package to changes in the thermal conductivity of the mold compound. The arrow indicates the error.

The minimum was found again by second order polynomial fitting of the five heating configurations and averaging their minima. The resulting comparison factor is stated in table 5.

Table 5: Parameter estimation for the SiP package.

Package	Parameter	Comparison factor
SiP	Mold compound κ	3.6 ± 0.7

8.4 Adjustment of Specific Heat

Using these optimized thermal conductivity values, the complete heat equation, eq. 3.64, was solved in time dependent FEM simulations to adjust the heat capacities of the materials under investigation. Since the die attach adhesive is modeled as two-dimensional thin film, the remaining components for the specific heat optimization are the substrate, the clear mold compound and the LCP lid cap for OLGA and the mold compound for the SiP package. The defined response is the difference of the integrals in a range of 10 to 900 seconds. The MatLab code for this evaluation is appended.

Figure 41 shows the measured curve for the three diode - 90 mA - heating setup and the sweep of the specific heat of the materials. For the OLGA package for all materials the value was changed to the same extent.

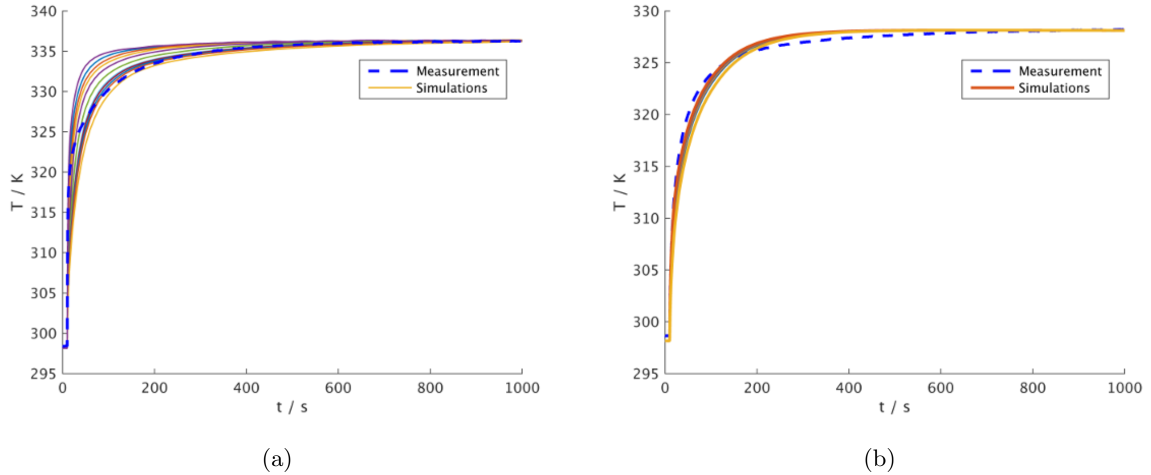

Figure 41: Measured temperature evolution curve and specific heat sweep curves for the OLGA package (a) and for the SiP package (b)

The resulting responses are plotted in figure 42. One can see that there is no minimum of the specific heat in a reasonable range. The specific heat values of the OLGA package (substrate, clear mold, lid cap) were all changed by the same factor. The comparison between measurement and simulation of the OLGA package shows large deviations in the range of the largest derivative, that can only be compensated with unreasonable high specific heat values. This suggested that the model was too simple.

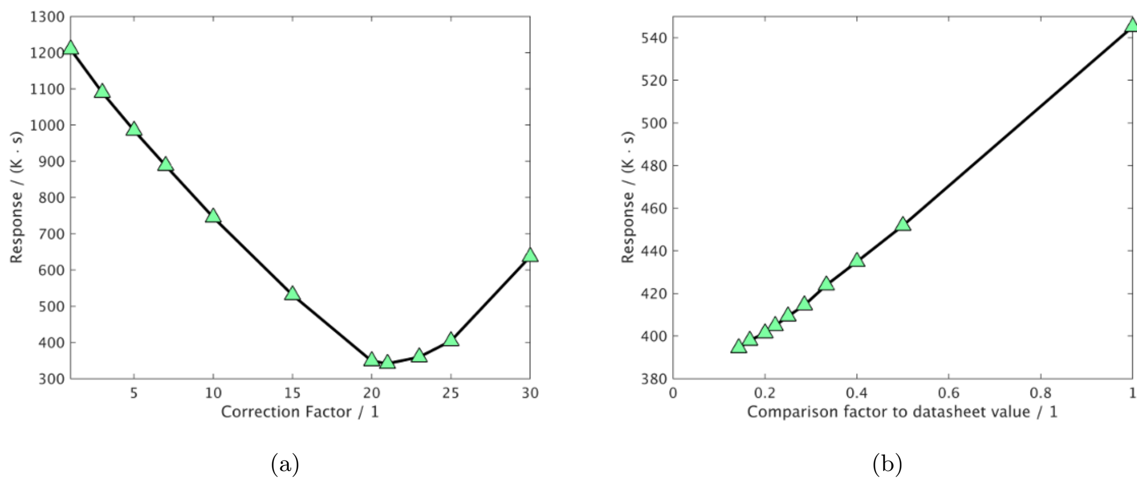

Figure 42: The comparison factor of the specific heat of the OLGA package (substrate, clear mold, lid cap) (a) and of the SiP mold compound (b) do not show a minimum in a reasonable range.

8.5 Model Adaption

Adaptions of the models were done throughout this work. But the large deviation in the range of the largest derivative suggests that the model simplifications still do not suit the goal of this work. As a consequence, the conducting path inside the printed circuit board was modeled using the average thickness of the copper lines to connect the the OLGA package's leads to the true

positions of the PCB's pins. Again, the thermal conductivities were adapted to compensate the wrong diameters.
In addition, the thermal conductivity of the PCB (fire resistant glass-reinforced epoxy laminate (FR4)), for which the implemented COMSOL value was taken, was defined to be anisotropic ($\kappa_{inplane} = 0.29$ Wm^{-1}K^{-1}, $\kappa_{\perp} = 0.81$ Wm^{-1}K^{-1} [42]). The refined model of the OLGA package construction can be seen in figure 43.

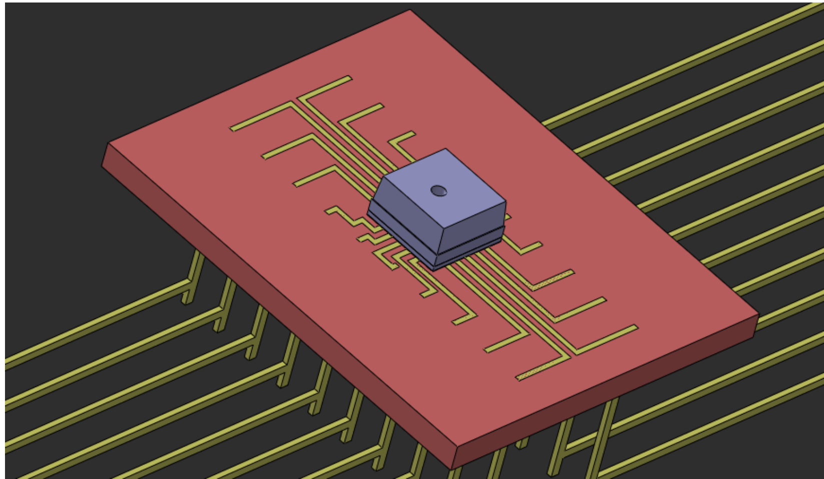

Figure 43: Adapted model of the OLGA package construction.

The optimized parameter set for the thermal conductivity for the model adaption is listed in table 6 after three runs of narrowing down the parameter ranges. The response surfaces for the case of largest power dissipation are plotted in figure 44.

Table 6: Parameter estimation with confined ranges for the adapted model of the OLGA package.

Package	Parameter	Comparison factor
OLGA	Substrate κ	0.4 ± 0.3
OLGA	Clear mold compound κ	0.9 ± 0.1
OLGA	Die attach adhesive κ	1.0 ± 0.1

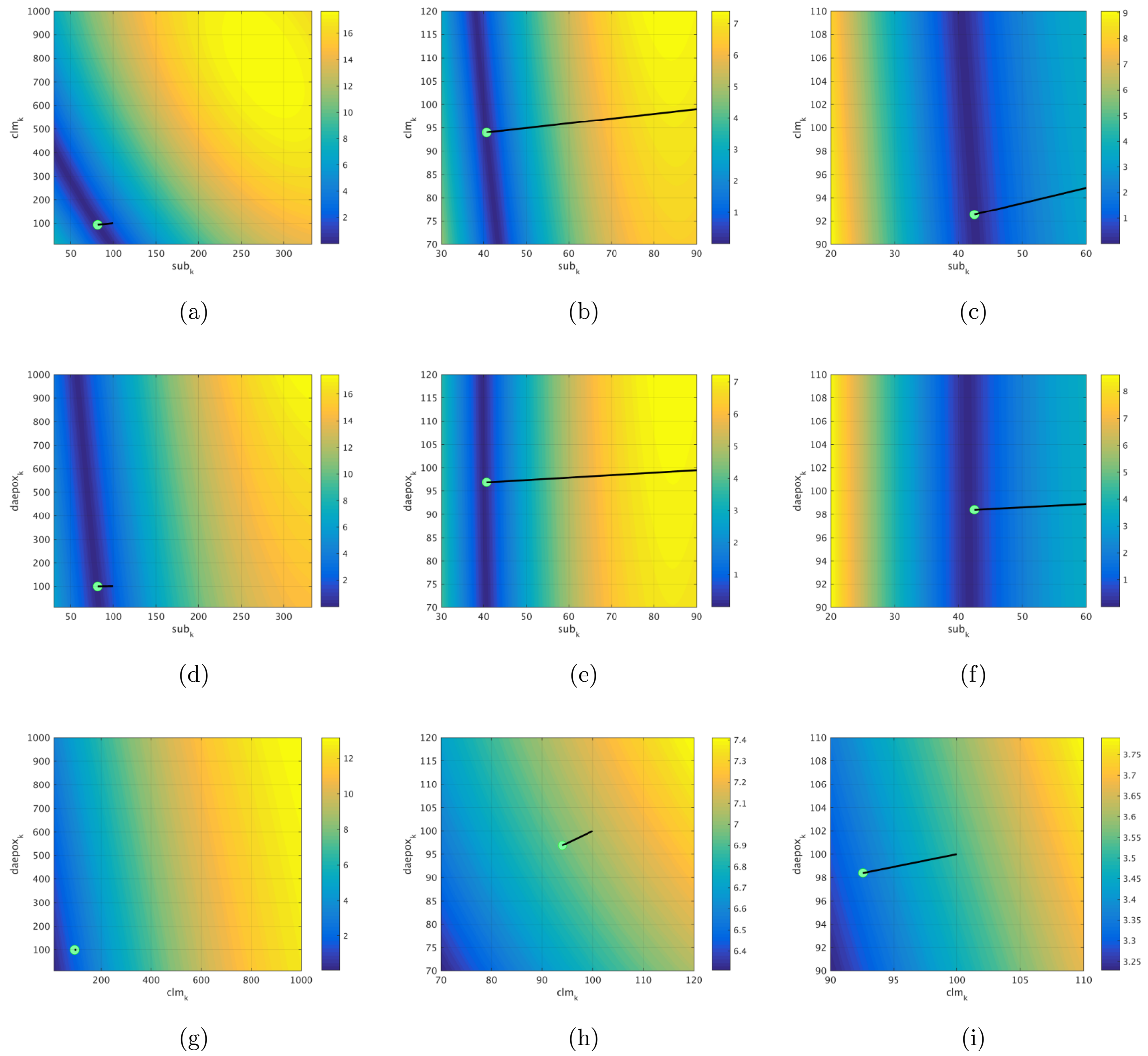

Figure 44: Two dimensional projections of the three dimensional response surface. Demonstrative example with 3 diodes and 333 mW overall heat dissipation. Left column: first run. Middle column: second run. Right column: third run.

The SiP package results including anisotropic FR4 are plotted in figure 45, the resulting comparison factor to the datasheet value is given in table 7.

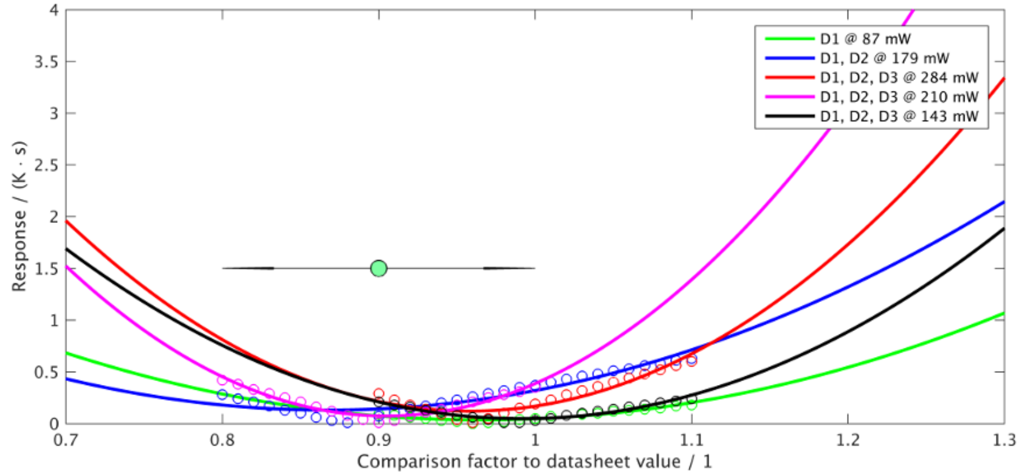

Figure 45: Response of the SiP package to changes in the thermal conductivity of the mold compound. Including anisotropic thermal condcutivity of FR4. The arrow indicates the error.

Table 7: Parameter estimation with confined ranges for the adapted model of the SiP package.

Package	Parameter	Comparison factor
SiP	Mold compound κ	0.9 ± 0.1

Figure 46 and 47 show the comparison of the one, two, and three diode heat configuration between measurement and κ optimized simulations.

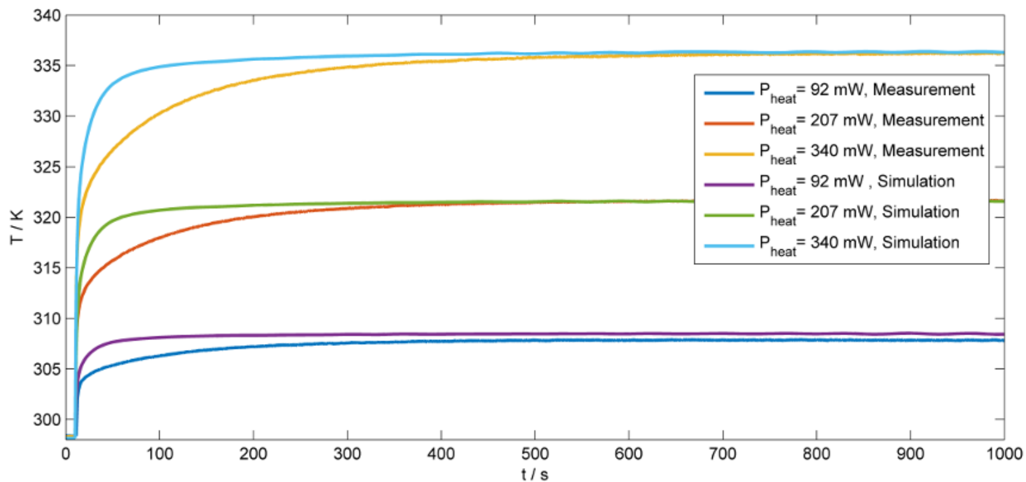

Figure 46: OLGA package: Comparison of measurement and simulation for the one, two, and three diode configuration.

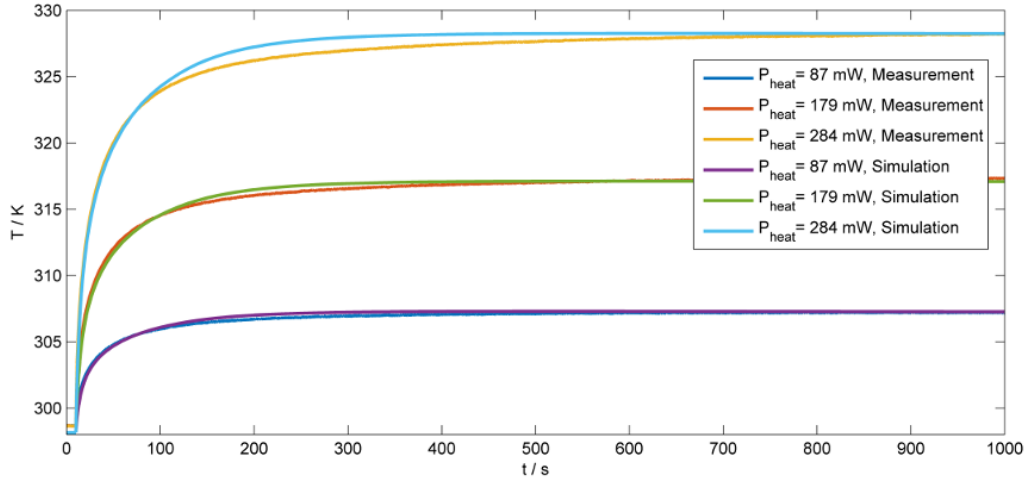

Figure 47: SiP package: Comparison of measurement and simulation for the one, two, and three diode configuration.

The comparison of measured surface temperatures, using the IR camera, and the simulated temperature evolution on the SiP package top boundary, are shown in figure 48. The OLGA package surfaces temperature simulations are far off the experiment, which could be due to the cavity structure of the package. One can see that for the SiP package also the surface temperatures are, with respect to the rather wide error margin of 2 K, in good agreement with the simulations.

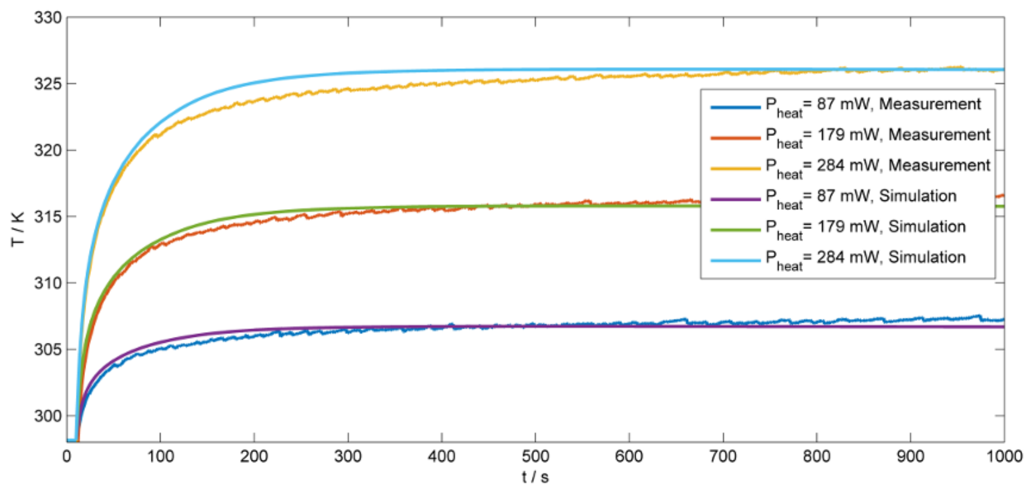

Figure 48: Measured surface temperatures and simulation results.

One can conclude that the influence of the anisotropy of the thermal conductivity of FR4 is significant and the optimized parameters for the materials that are governing the thermal behavior - namely the SiP mold compound and the OLGA substrate - are in a region close to the supplier information. The optima plotted in figure 44 are in a narrow range of the substrate's thermal conductivity. As a consequence, since we were using the optima closest to the initial values, the optimized thermal conductivities of the die attach adhesive and the clear mold compound are not representative. Still, this result is very nice, considering the large simplifications in the design

of the model and the experimental conditions and the simple implementation of air as a solid domain, which simplifies the effects of natural convection (see section 8.6). For the deviation of the thermal conductivity of the OLGA package substrate, two reasons appear likely: First, the substrate consists of many small features. These, we tried to model as accurately as possible, but small deviations in the structure already have non-negligible influence on the result. Also the refinement of the finite elements mesh influences the results considerably. These effects are not included in the error of the comparison factor. The second reason is the laminar glass fiber structure of the substrate (figure 49). For a more detailed study, the thermal conductivity of the substrate needs to be modeled anisotropically as well. Still, this would demand a more versatile temperature measurement approach.

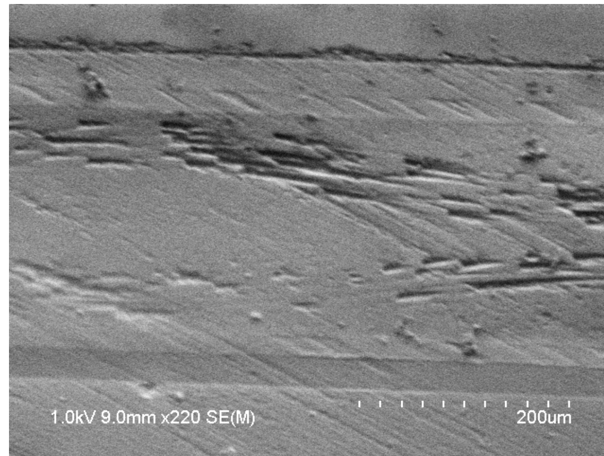

Figure 49: SEM picture of the substrate of the OLGA package.

Although the above results suggest reasonable agreement with the simulations, the adaption of the specific heat, by using the integral difference between measurement and simulation does not seem to be a valuable approach.

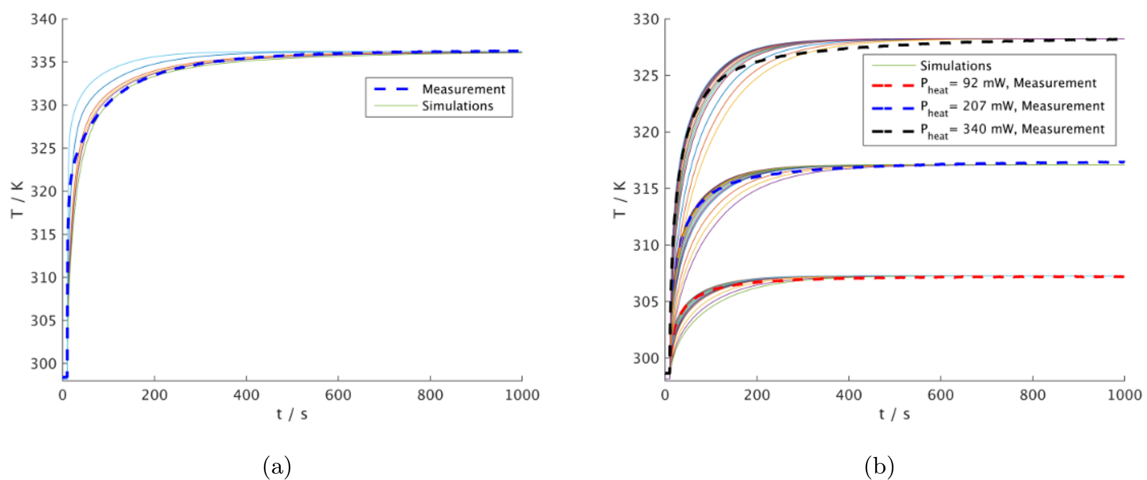

(a) (b)

Figure 50: Measured temperature evolution curve and specific heat sweep curves for the adapted model of the OLGA package (a) and for the SiP package (b). Both models with an anisotropic thermal conductivity of FR4.

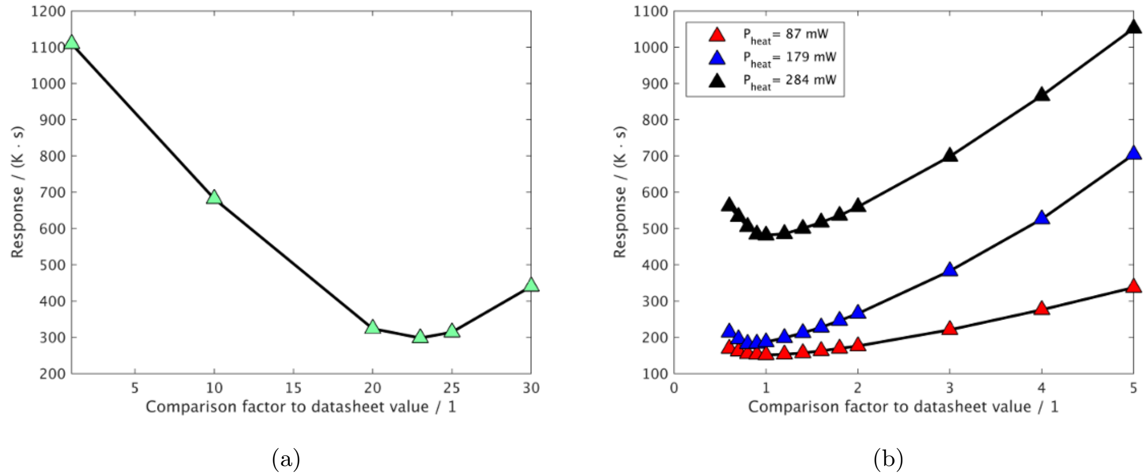

Figure 51: (a) The comparison factor for the specific heat of the OLGA package (substrate, clear mold compound, lid cap), for the three diode configuration, does not show a minimum in a reasonable range. (b) The comparison factors of the specific heat of the mold compound of the SiP package show a minimum close to the initial supplier value, consistent for three different heating configurations (one, two, and three diode heating).

The SiP package simulations show a consistent optimum close to the initial supplier value, but the optimization due to the adaption of the mold compound specific heat takes place in the wrong time region of the temperature evolution. The measurement shows a faster temperature rise within the first time period while it takes longer to reach steady state. This suggests that the components with small time constants may be underrepresented in the simulations. More discussion on the interpretation of time constants can be found in section 9.2. The simulations of the OLGA package, with swept specific heat of substrate, clear mold compound, and lid cap, do not show a minimum in the integral difference in a reasonable range.

It needs to be mentioned that the load boards used for contacting the devices were unstable and continuity problems were pretty common. Also, information on the power dissipation while using test modes, needed to contact the BJT temperature sensors, were partly wrong or missing. This led to futile usage of the generally very sparsely available simulation license access.

8.6 Natural Convection Considerations

One reason for the discrepancy of the above results could be that the climate chamber was modeled as a solid air domain. Therefore, convection effects are not explicitly implemented. Since the chamber fan rotation was turned off, only natural convection occured. Due to the large models, computational fluid dynamics simulations did not converge. Figure 52 shows the approach to include natural convection boundary conditions using eq. 3.8 and 3.9 for the not-adapted model. These equations are simplifications derived for single vertical walls and horizontal plates. Hence, the characteristic length L cannot be clearly defined, although, as simulations showed, it has a significant influence on the results. Therefore, the air flow does not model reality sufficiently well. As a consequence, the optimized range estimations for the thermal conductivity vary by more than a factor of six for the OLGA package substrate and

the SiP package mold compound, between different heat configurations. Still, one can see that the inclusion of these simplified conditions affects the time range of the largest curvature of the temperature rise so that it resembles that of the experiment.

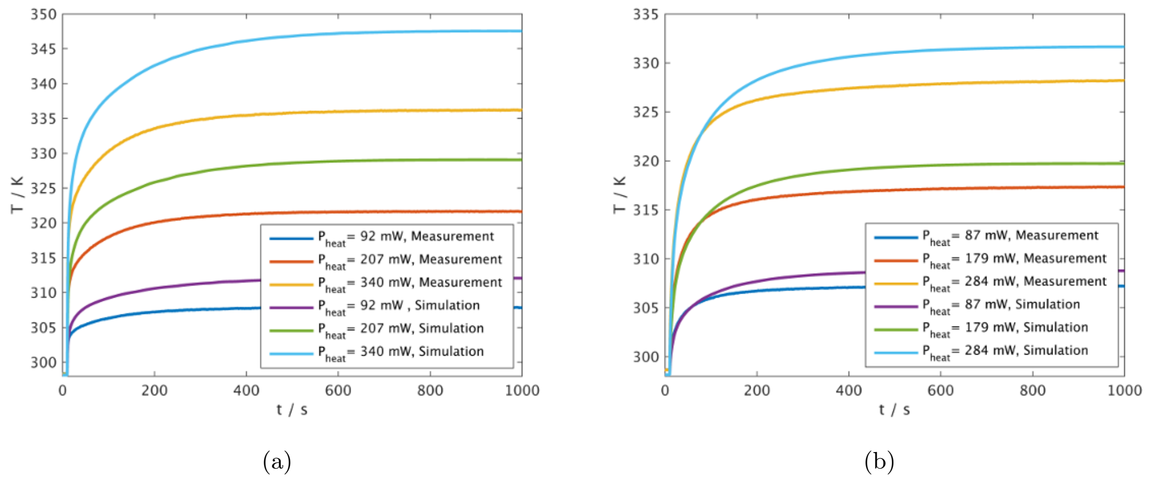

(a) (b)

Figure 52: Simulations including simplified horizontal plate and vertical wall natural convection boundary conditions. (a) OLGA package, (b) SiP package.

8.6.1 Vacuum Measurements

To exclude the influence of natural convection, experimental runs under vacuum conditions were done. These were conducted in the vacuum chamber of a scanning electron microscope. Since this is not a temperature controlled environment, simulations could not reconstruct the thermal behavior. Still, although most of the heat is assumed to be conducted downwards through the die to the leads, one can see in figure 53 that convection has a major impact to the overall heat transfer.

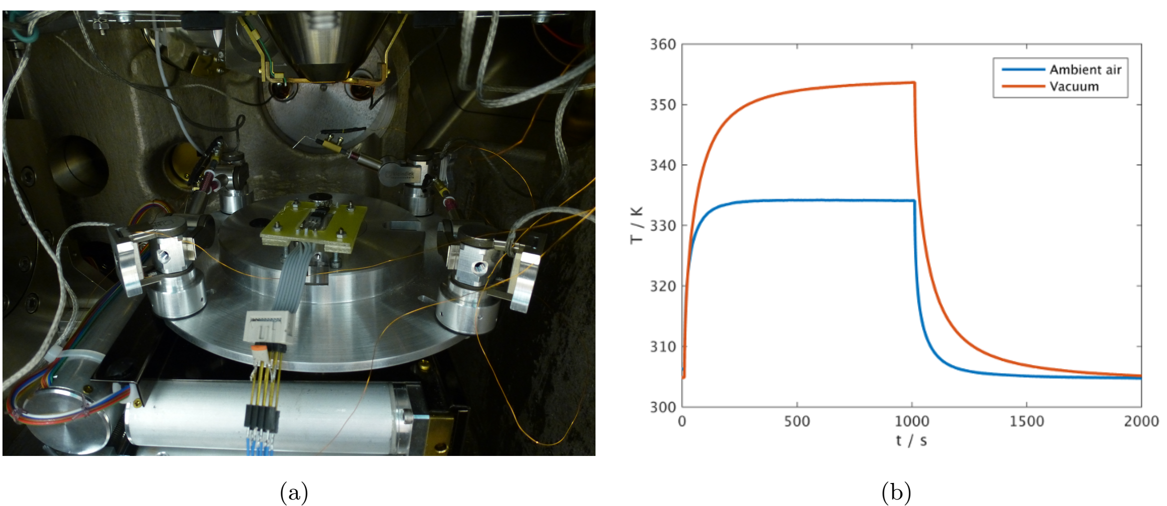

(a) (b)

Figure 53: (a) The SiP device contacted inside a SEM vacuum chamber. (b) The three diode heat configuration with evacuated and vent chamber.

8.6.2 Foam Embedded Device

To be able to estimate the influence of natural convection on the quality of the optimized parameter values one last approach was conducted. It is stated [43, 44] that polyurethane foam has a thermal conductivity close to that of air ($\kappa \approx (0.025 - 0.03)$ Wm^{-1}K^{-1}), hence, it should have low effect on the steady state temperature if there was no convection effects. Therefore, the devices were embedded in a 20 x 15 x 15 cm box, filled with polyurethane foam. The devices were located in the center of the box. The whole system was cured for two hours at 60°C (see figure 54).

Figure 54: The devices were embedded in polyurethane foam to exclude the effect of natural convection.

Figure 55 shows the difference of the temperature evolution with and without polyurethane environment. The steady state temperatures of the foam embedded devices lie consistently (31 ± 2) % for the OLGA package and (26 ± 4) % for the SiP package, above that of the devices in ambient air.

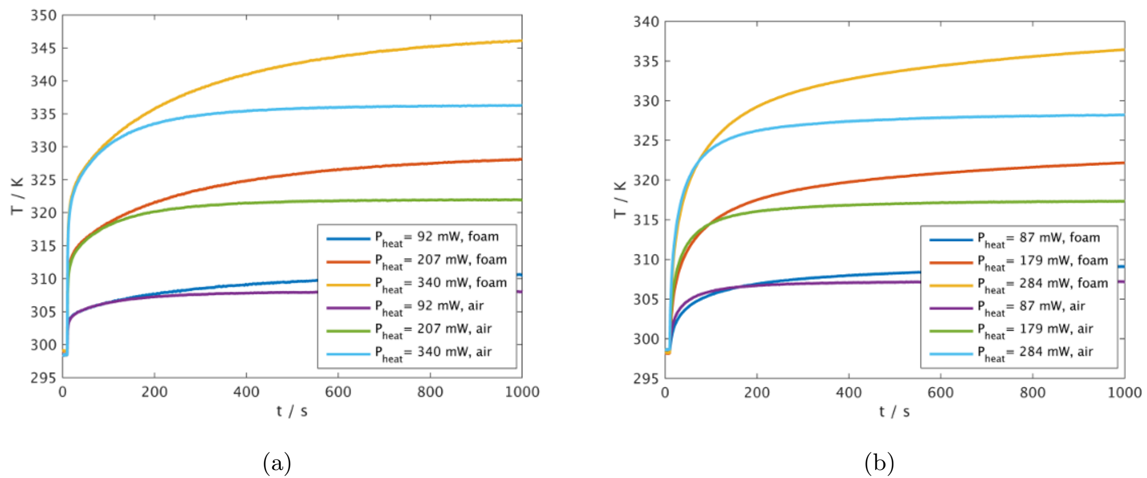

Figure 55: Comparison of the heat up characteristics embedded in polyurethane foam and at ambient air. (a) OLGA package, (b) SiP package.

A simulation was set up, using the materials parameters optimized above. The foam was modeled

as uniform solid domain with $\rho = 30\ \mathrm{kg\,m^{-3}}$ and $c_p = 1500\ \mathrm{J\,kg^{-1}K^{-1}}$ [43]. Optimizing package materials parameters, while using literature values for thermal conductivity of the foam (0.03 $\mathrm{Wm^{-1}K^{-1}}$), yields results that do not compare to the range of the parameters optimized above. A fit of the foam properties resulted in a thermal conductivity of (0.063 ± 0.006) $\mathrm{Wm^{-1}K^{-1}}$ for both models, averaged over simulations for the one, two, and three diode configuration. Since this value is consistent for both models, it is a reasonable assumption that the thermal conductivity value from literature does not represent the reality conditions. Foam geometry, density and cell size depends on its composition and the way it is deposited. Its contact to the device boundaries cannot be assumed to be perfect. This affects the thermal resistance within the foam. Murphy [45] and Thirumal *et al.* [46] also showed that moisture inside the foam can have appreciable influence on its density and thermal conductivity. As a consequence, a perfect foam environment can have higher thermal resistance, which would result in higher steady state temperatures. This can explain the high thermal conductivity values of the foam in the simulations, necessary to fit steady state temperatures of the experiment. As a consequence, the difference between the measurements in figure 55 could be related to natural convection (and a small part of radiation). Still, without knowing the foam's exact thermal properties, no valuable statement can be made.
As a conclusion, natural convection is not negligible, but an estimation of its influence on above results will not be possible without mathematically correct implementation. This involves computational fluid dynamics simulations that are computationally very expensive for models with this number of elements.

8.7 The Influence of Thin Films on Top of the Die Surface

During the progress of this work, it turned out that the actual structure of the die's surface is not as initially assumed. The SiP package's passivation also includes a polyimide layer above the silicon nitride protection layer and the OLGA package has, due to the sensing diode concept, a thin film structure above the passivation as can bee seen in the scanning electron microscope pictures in figure 56.

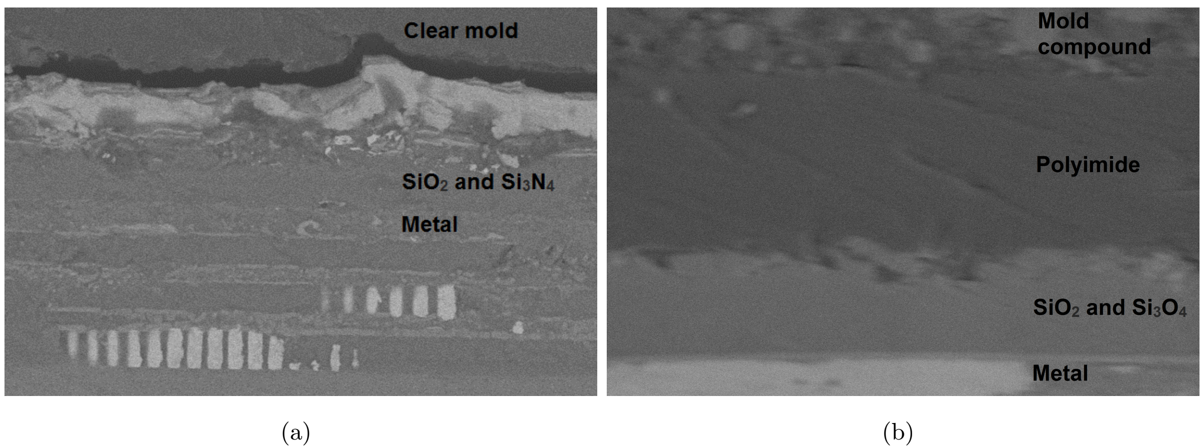

(a) (b)

Figure 56: Device structure between die and mold compound. (a) OLGA package. (b) SiP package.

On top of the top metal line (fourth metal line in figure 56a and bottom line in 56b), one can

see the SiO_2 and Si_3N_4 passivation and protection layer. The SiP package has additionally a polyimide layer on top to absorb mechanical stress. The OLGA package also shows some additional layers on top of the silicon nitride that consist of interference filters for the sensing diodes and blackening layers as irradiation protection.
Not all these materials' properties are known, but figure 57 shows, that an exclusion of the passivation and protection layers does not result in a change of the results. Of course, still, due to the lack of exact materials composition, no thermal interface resistance is included in the models, which could have appreciable influence on the results.

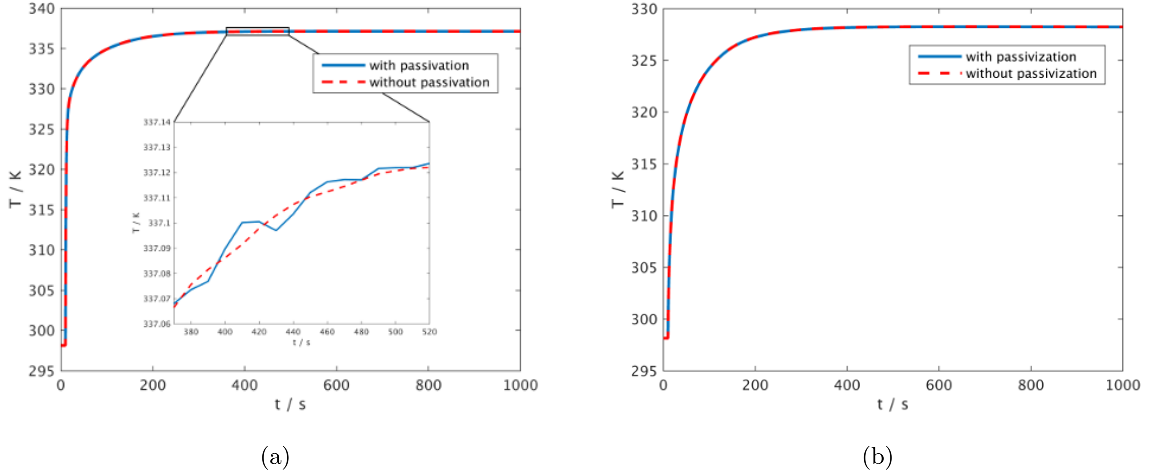

Figure 57: Comparison of simulations with and without passivation and protection layers. (a) OLGA package with and without SiO_2 and Si_3N_4. (b) SiP package with and without SiO_2, Si_3N_4, and polyimide. The inset shows the difference that comes from numerical noise.

8.8 Temperature Evolution and Heat Paths

The following figures show the temperature evolutions and heat paths within the packages. In the OLGA package, most of the heat flows either downwards through the die and the die attach, or through the wire bonds (right side of the die). Then, the conducting path in the substrate dominates the heat path. The heat is transported off through the leads and the copper lines of the printed circuit board. Almost no heat flows upwards through the lid attach into the lid. The lid mostly warms up because of the air inside the cavity. The heat sources are defined directly at the wire bond-to-die interface. This leaves the three bonding wires having by far the highest temperature in steady state, due to the low heat capacity and low cross section of the bonds. As a consequence, the heat path in this region is dominated by the vertical path, as indicated by the three biggest arrows in the right column of figure 59 (mind that the top arrow in fig. 59b indicates the downwards flux while the flux through the wire bond is represented by a smaller arrow beneath). Still, when reaching the substrate, the heat flux is strongly dominated by the substrate drills, fingers, and leads, which makes exact modeling a crucial requirement for thermal simulations. This shows also that measurements on the anisotropic thermal conductivity of the substrate will be important for future developments of inverse modeling approaches.

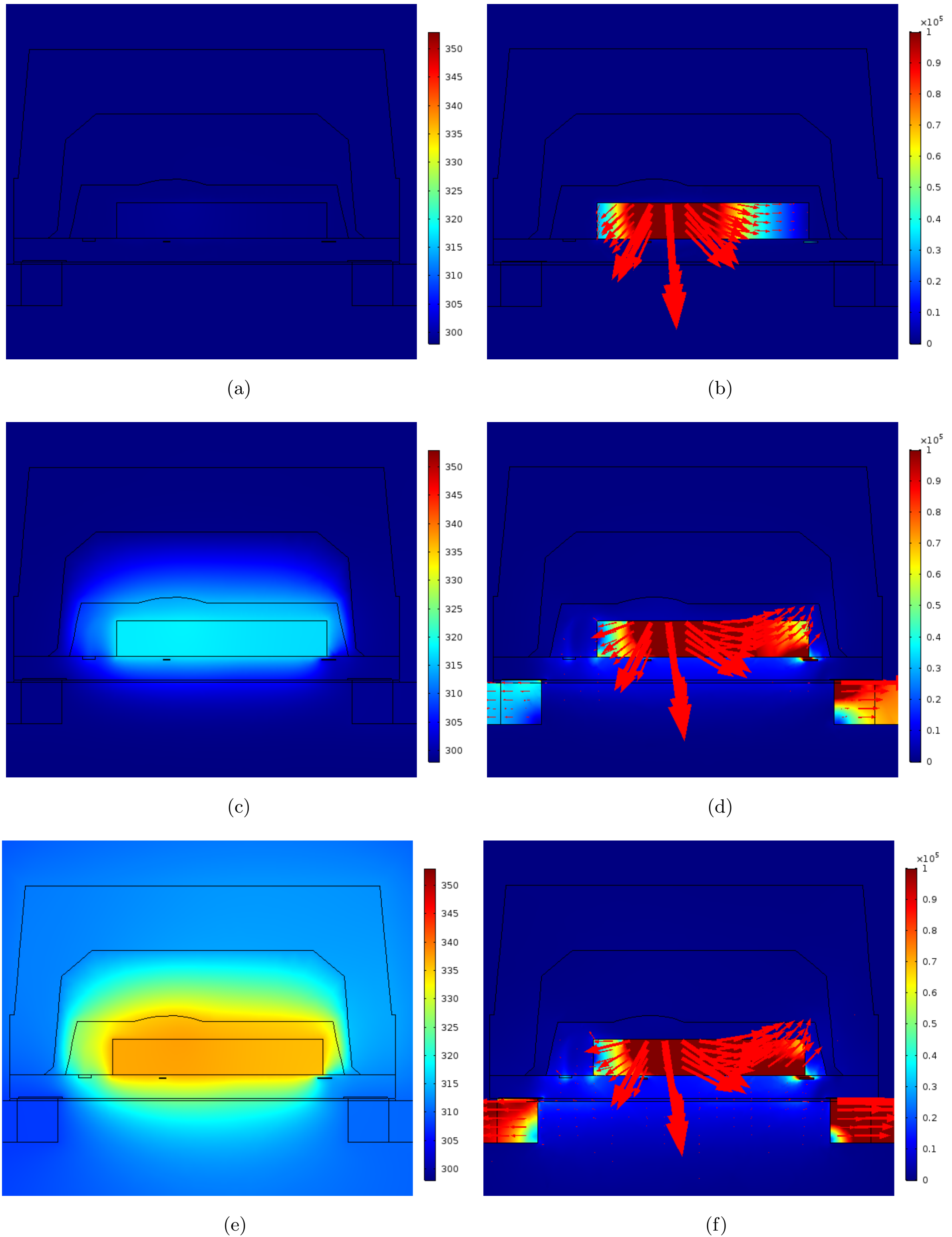

Figure 58: Temperature distribution of a cross section of the OLGA device (a) after 10 ms, (c) after 1 s, (e) in steady state. Heat flux (b) after 10 ms, (d) after 1 s, (f) in steady state. The arrow length is scaled by $4 \cdot 10^{-9}$ and corresponds to the heat flux at the arrow's tail.

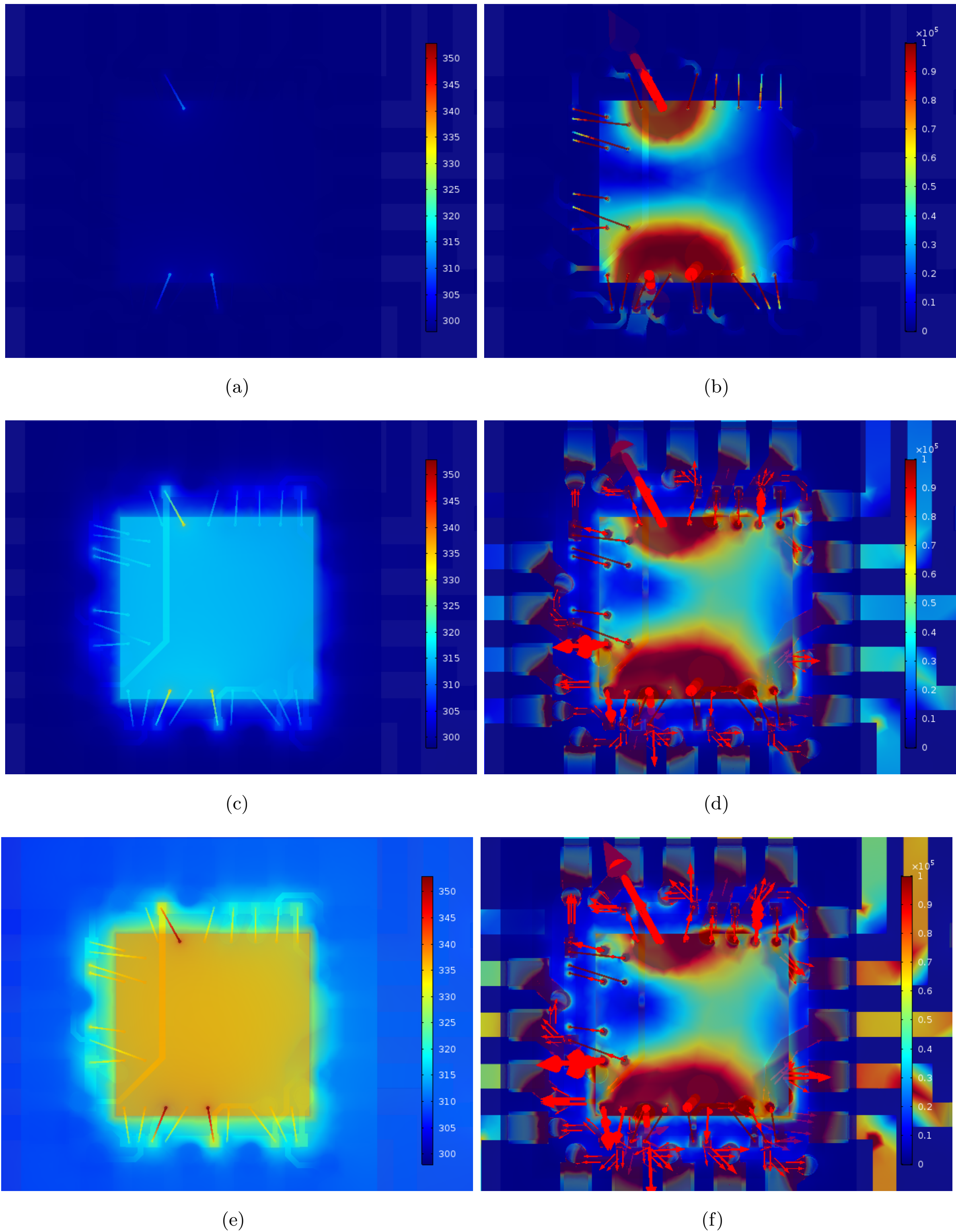

Figure 59: Temperature distribution of the die and lead structure of the OLGA device (a) after 10 ms, (c) after 1 s, (e) in steady state. Heat flux (b) after 10 ms, (d) after 1 s, (f) in steady state. The arrow length is scaled by 10^{-10} and corresponds to the heat flux at the arrow's tail.

In the SiP package, the leads are only connected to the die via the bonding wires or the highly thermal resistive mold compound. Only the ground lead is a direct extension of the ground plate where the die is attached onto. Therefore, although all three powered diodes are on the left side of the die, the heat flux is heavily dominated by the path vertical to the lead frame and then, horizontal through the ground lead on the right side. In comparison to the OLGA package, here the alternative paths through the bonding wires are almost negligible for the steady state temperature measured on the die surface, as simulations with and without wire bonds showed. Figure 62a shows infrared thermal images of a SiP device that was etched open using nitric acid and sulfuric acid. The passivation layer on the die surfaces protected the die, and the IC was still fully functional. Due to the high thermal conductivity of silicon, almost no temperature gradients within the die can be seen. The heat from the powered diode in the top left corner is distributed all over the die and the temperature of the mold compound, that surrounds die, only rises slowly. The simulation in figure 62b reproduces the qualitative behavior well.

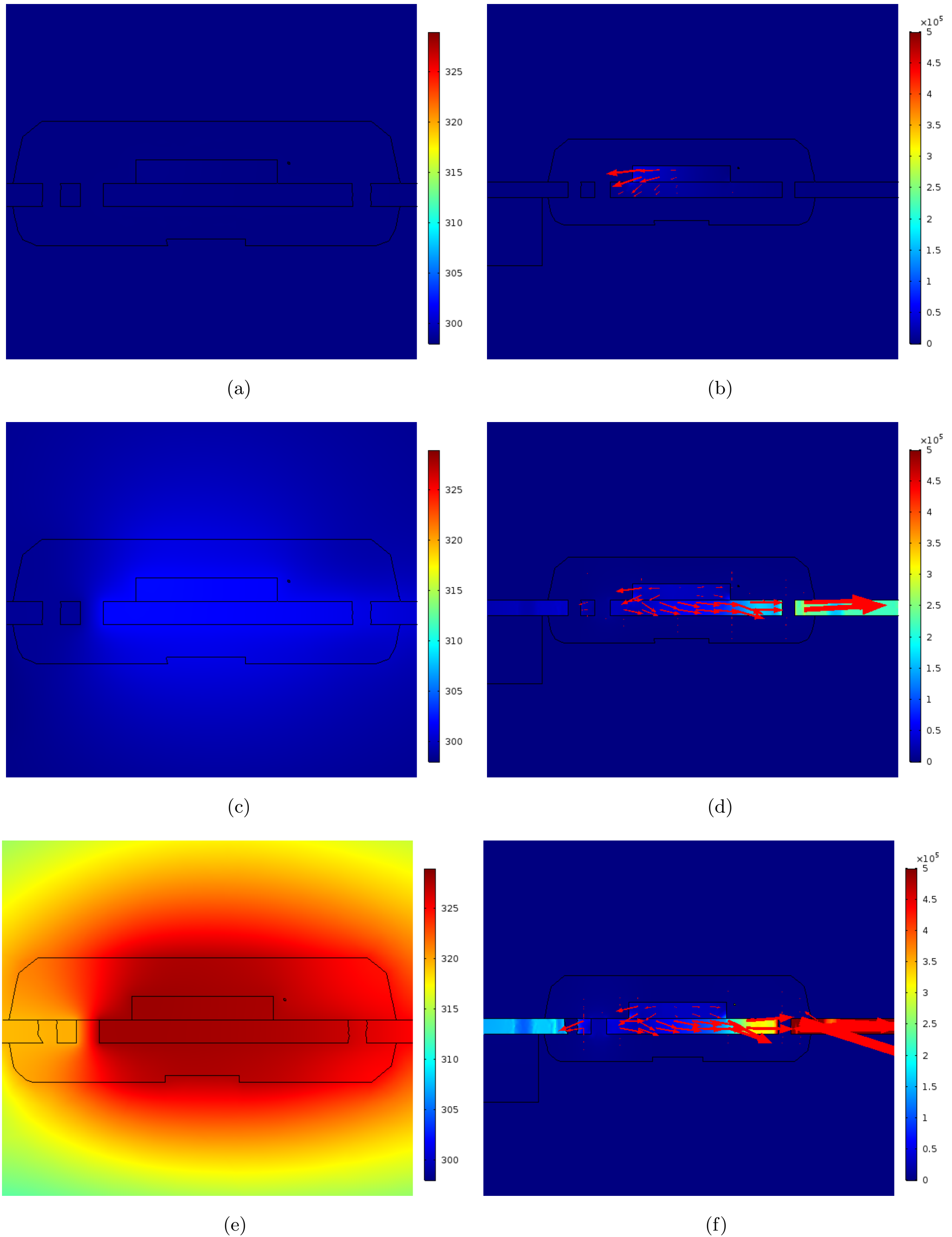

(a) (b)

(c) (d)

(e) (f)

Figure 60: Temperature distribution of a cross section of the SiP device (a) after 10 ms, (c) after 1 s, (e) in steady state. Heat flux (b) after 10 ms (d) after 1 s, (f) in steady state. The arrow length is scaled by $2 \cdot 10^{-8}$ and corresponds to the heat flux at the arrow's tail.

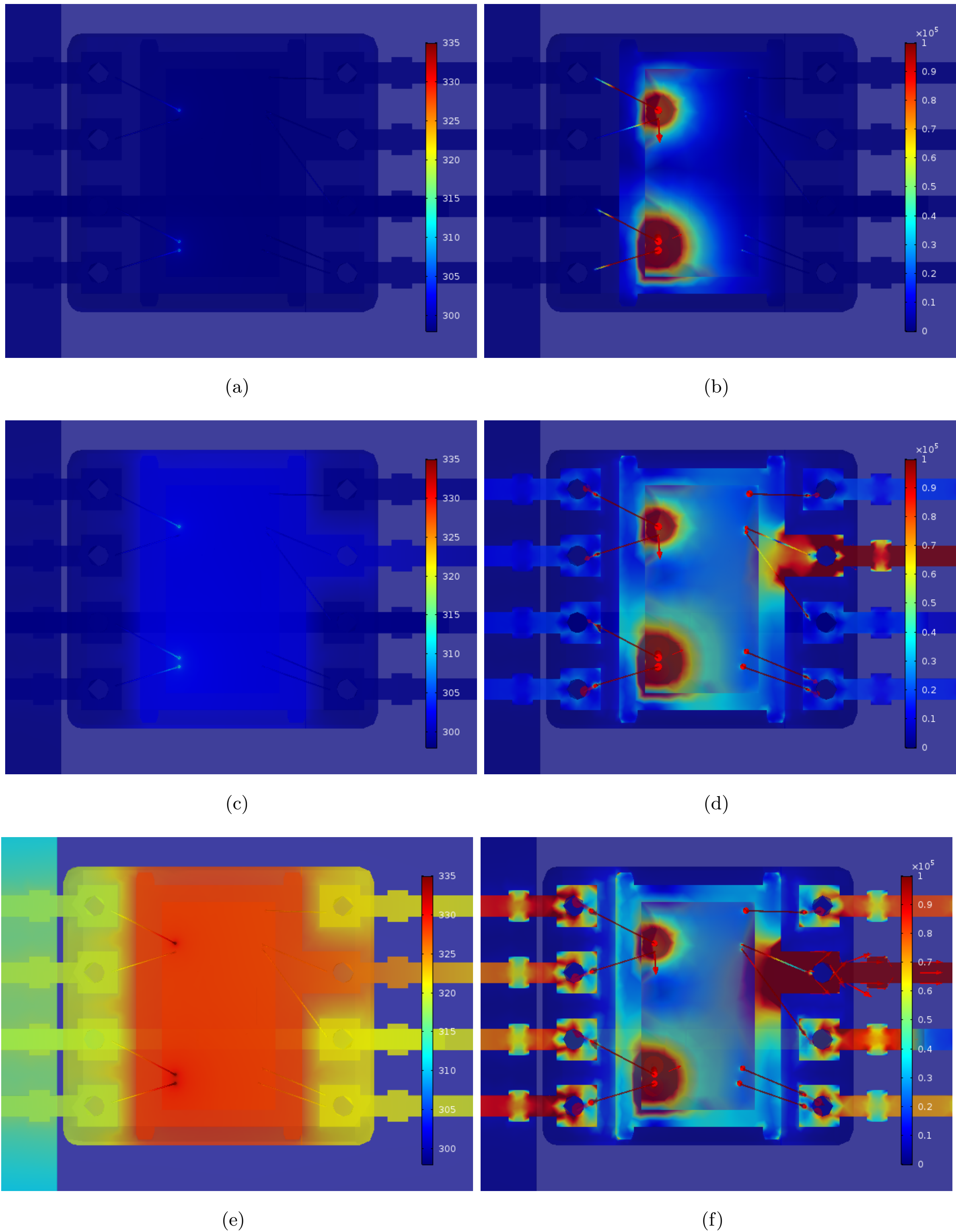

Figure 61: Temperature distribution of the die and lead structure of the SiP device (a) after 10 ms, (c) after 1 s, (e) in steady state. Heat flux (b) after 10 ms (d) after 1 s, (f) in steady state. The arrow length is scaled by $2 \cdot 10^{-10}$ and corresponds to the heat flux at the arrow's tail.

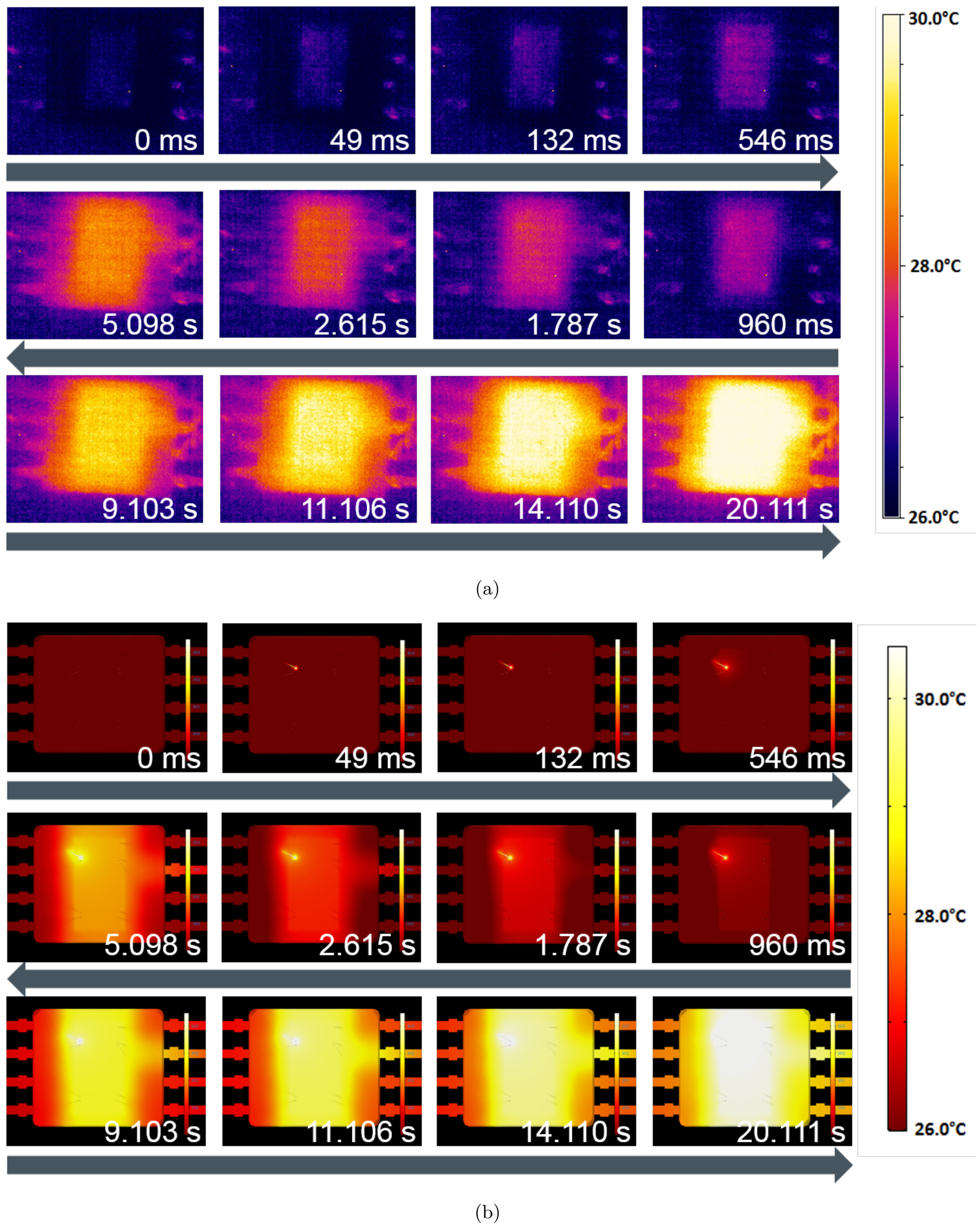

Figure 62: Temperature evolution at the die surface of an etched open SiP package. (a) IR measurement, (b) simulation.

9 Outlook

9.1 Raman Measurements

The problem of the experimental setup, used for above results, is, that within the device structure only temperature measurements at the die surface, hence, at one level could be made. Raman signals are temperature dependent and are often used for temperature measurements using the ratio of the vibrational Stokes- and the anti-Stokes peaks [47, 48, 49].
The ratio is given as

$$\frac{I_s}{I_{as}} = \frac{(\tilde{\nu}_0 - \tilde{\nu}_R)^4}{(\tilde{\nu}_0 + \tilde{\nu}_R)^4} \cdot \exp\left(\frac{hc\tilde{\nu}_R}{k_B T}\right) \tag{9.1}$$

with $\tilde{\nu}_0$ being the radiated laser frequency and $\tilde{\nu}_R$ the Raman shift. This ratio can be calculated at every point on the half side of the spectrum, which reduces errors drastically and makes it a widely used approach.

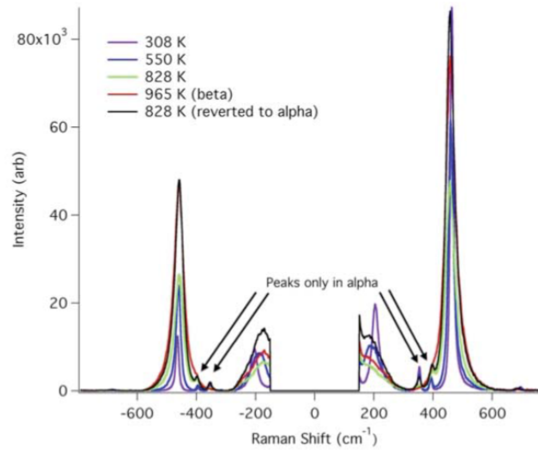

Figure 63: The Raman peak intensity is temperature dependent [49].

Nevertheless, for this method, it is necessary to obtain both sides of the spectrum, and a notch filter is needed. These filters degrade, are very expensive, and were not available. Therefore, this method could not be used for temperature mapping in our devices.
Still, the anti-Stokes peak itself suffers from amplitude change and change in Raman shift due to a change in temperature depending on the rotational quantum number [47]. It can be a usable approach to choose specific bands of the spectrum of the different materials of the device, and calibrate their temperature dependence. Then, two temperature controlled plates can be attached to both ends of the device to create a known heat flux. By using the known thermal conductivity of silicon and the temperature mapping, an estimation of the thermal conductivity of the different materials within the heat path can then be made.
The devices were embedded in epoxy resin and ground with eight different grain sizes to obtain a polished cross-section of the device. Still, as can be seen in figure 64, the Raman intensity varies strongly within the same material. The intensity map is plotted for the 1610 cm^{-1} band of the clear mold compound of the OLGA device.

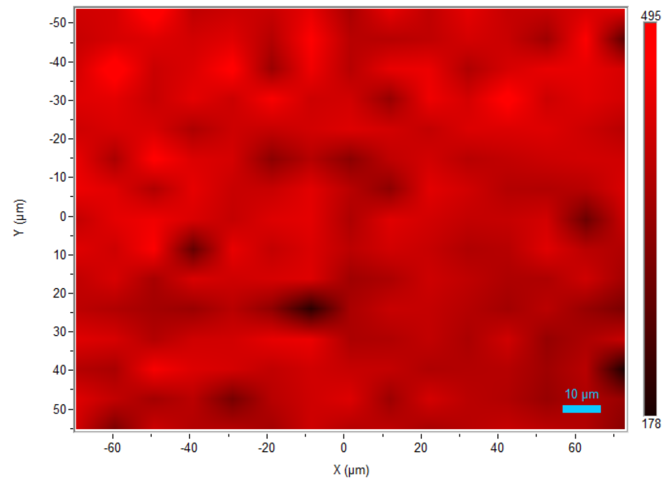

Figure 64: The anti-Stokes signal of the 1610 cm^{-1} band of the clear mold compound of the OLGA package varies strongly within the material itself.

This is most probably a result of the grinding process of the device. Also, the Raman intensity does not show strong temperature dependence as measurements for the same band at room temperature and at 50°C show (figure 65).

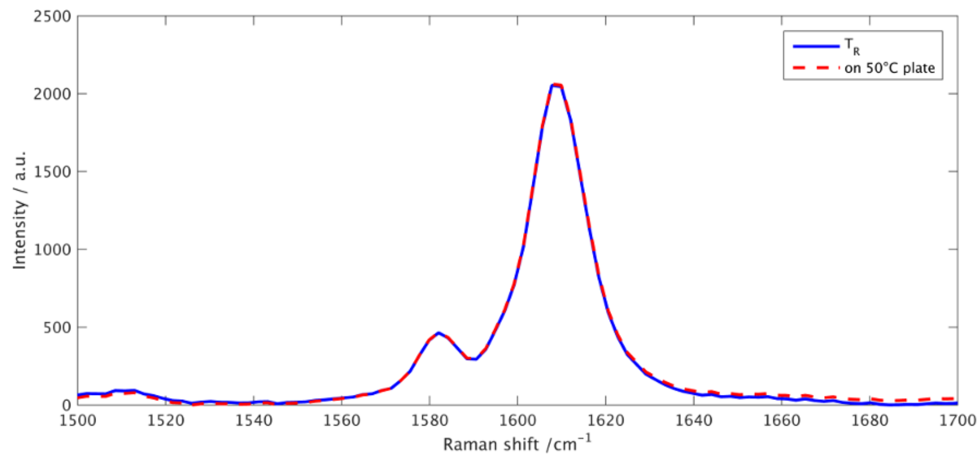

Figure 65: The peak intensity of the anti-Stokes signal in the range of 1610 cm^{-1}.

Finally, only for the clear mold compound and the die attach adhesive a Raman spectrum could be obtained at all. These are plotted in figure 66.

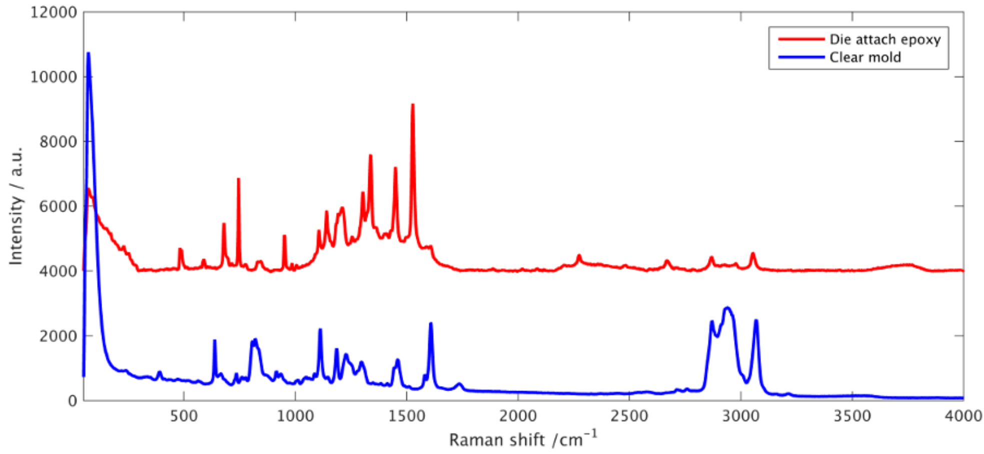

Figure 66: Anti-Stokes part of the Raman spectra of the clear mold compound and the die attach adhesive of the OLGA package.

The interpretation of the spectra is out of the scope of this work. Still, some of the bands show typical characteristics. The bands at 3000 cm^{-1} are typical for C-H-streching of aryl (aromatic carbon rings) and methyl, and the 1610 cm^{-1} band is typical for C-C-streching between methyl and quarternary carbon.
Temperature measurements using only anti-Stokes measurements still could be a reasonable approach if no notch filter for the standard Stokes-anti-Stokes-ratio method is available. Then, alternative approaches for device preparation, like breaking or cutting, need to be considered. Also, the calibration needs to be done for multiple bands to reduce the error margin to a reasonable range. Still, this would require extensive measurement time using expensive equipment, which is out of the cost range of this project.

9.2 Transient Measurements

Another concept are lumped networks. When heat flows through a multilayered system, the response of the system to a temperature step function depends on the thermal conductivities and heat capacities of the materials within the path. A one-dimensional heat path can be modeled as a lumped RC network that represents the thermal resistances and heat capacitances of the materials included in the path [50].

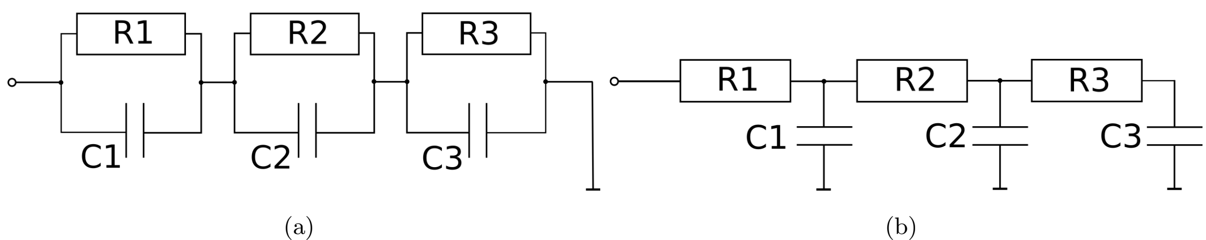

Figure 67: (a) Lumped circuit model (Foster network) of the thermal resistances and heat capacities of a three component system. (b) Equivalent Cauer network, assumed to represent the real heat flow structure.

The different components of the system need different amounts of time until they reach steady state temperature. Therefore, to each component a time constant can be associated and the response of the lumped circuit to a unit-step excitation can be written as

$$a(t) = \sum_i R_i \cdot (1 - \exp(\frac{-t}{\tau_i})) \tag{9.2}$$

with the time-constant $\tau_i = R_i C_i$. For a continuous resistance spectrum and using the substitutions $z = \ln t$ and $\zeta = \ln \tau$, the resistance spectrum can be obtained by deconvolving the known function $w(z) = \exp(z - \exp(z))$ out of the equation [51]:

$$\frac{\mathrm{d}}{\mathrm{d}z} a(z) = R(z) \ast w(z) \tag{9.3}$$

This lumped network can then be transformed into a so-called Cauer network, that is assumed to represent to real heat flow structure, since the capacitances are related to ground (figure 67b).

This approach was tried measuring the cooldown transient for 10 seconds with a measurement rate of 100 KHz at a A/D conversion of 18 bit. Longer measurements at higher frequency were not possible due to memory restrictions of the company internal test system used to contact the devices. The transients are shown in figure 69. Still, the approach using basic FFT could not resolve a time constant spectrum. Reasons for this could be the too low measurement frequency that creates numerical problems in the derivative and deconvolution. Also the low signal-to-noise ratio of approaches with external 12 bit digital oscilloscopes resulted in no valuable outcome. Although test probes with high attenuation and, hence, high input resistance ($10\ M\Omega$) and low input capacitance ($13\ pF$) were attached, it changed the measured voltage on the analog pins. These problems could maybe be solved by re-calibrating the temperature measurement while using an external oscilloscope with a high enough resolution and by using more sophisticated numerical deconvolution approaches.
In figure 68 one can see the time constants resulting out of a fit consisting of a sum of decaying exponentials.

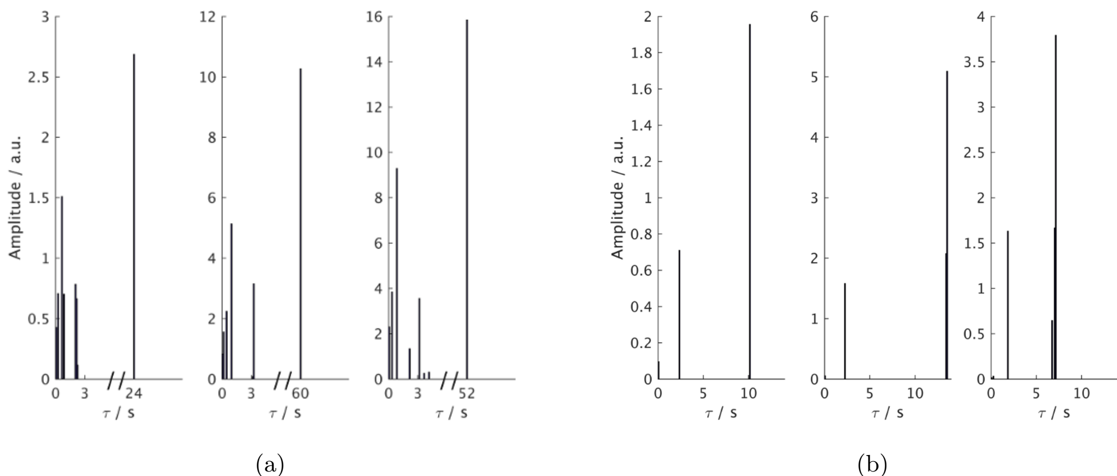

Figure 68: Comparison of the time constants fit by a sum of 11 decaying exponentials. One, two, and three diode configuration. (a) OLGA package. (b) SiP package.

The forms of the figures for the one, two, and three diode heat configuration resemble each other, and, therefore, illustrate that the time constants are characteristics of the heat flow. But these results cannot be associated to distinct components.

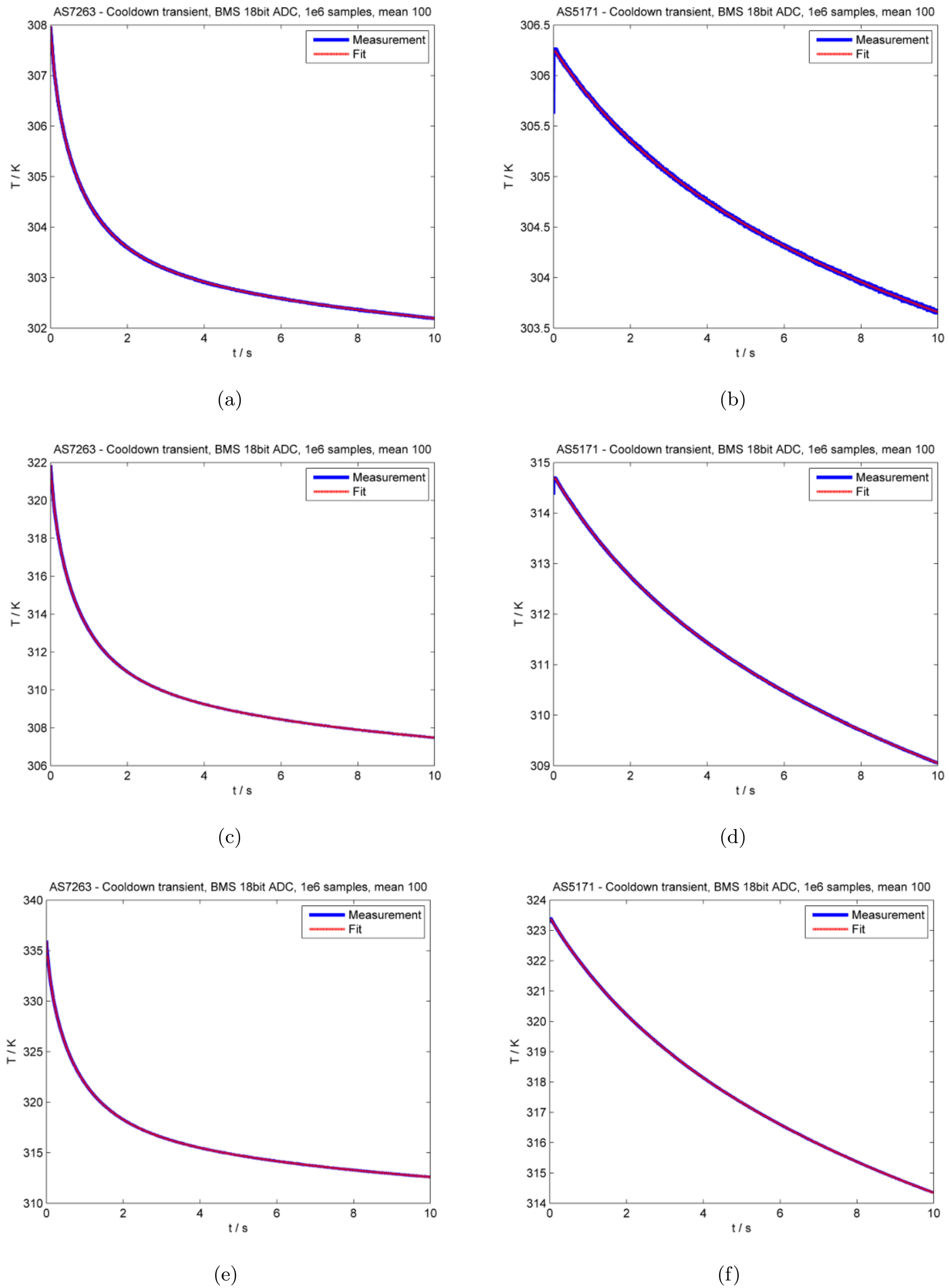

Figure 69: Cooldown transients for the one diode (first row), two diode (second row), and three diode heat configuration (third row). Left column: OLGA package. Right column: SiP package.

9.3 Computational Fluid Dynamics Simulations

As stated above, simple attempts to include natural convection by fluid dynamics simulations did not converge. For a high quality statement on the impact of natural convection and, hence, for reasonable results for an optimized parameter set using the method of this work, this approach would need further examination. Still, concepts for convergence, like auxiliary sweeps of the air viscosity would be needed and resources for the increased computational costs need to be provided.

9.4 Measurement Concepts

For a more complete picture of thermal transport in microelectronics packaging, more diverse measurement concepts need to be set up. Temperature measurements on various vertical levels of the package would give a more detailed picture. For this purpose multi-die packages, built from the materials under investigation, could be fabricated.

9.5 Thermal Property Measurements

Besides the concept of inverse modeling of materials parameters, direct measurements of the properties need to be made. Differential scanning calorimetry (DSC) measurements were performed, to obtain temperature dependent specific heats. Ever if samples of the used materials are available, their processing has significant influence on their properties. Especially the thermal conductivity strongly depends on the geometry of the material, for example when processed as thin films. Therefore, measurement concepts like laser flash, guarded heat flow, transient plane source or time-domain thermoreflectance methods need to be considered and appropriate samples need to be provided.

9.6 Thermal Interface Resistances

Since papers show that the influence of interfaces to the overall thermal resistance can be substantial, concepts for calculations on its effect can be made. Molecular dynamics simulations rely on the chosen potentials, and for first principle calculations, the phonon density of states needs to be known. Both require knowledge of the exact materials composition or rather elaborate measurement concepts like inelastic neutron scattering. Generally, sparse information on materials chemical compositions hinder additional approaches of thermal behavior calculations. Multilayered test samples of the materials of interest can be made for estimating interface resistances. Due to the high number of interfaces within the mold compound, thermal experiments for different filler configurations could be set up.

10 Conclusion

This work tries to give a better insight into thermal transport in microelectronics packaging. An approach of inverse modeling of materials parameters by fitting simulations to experimental results could optimize thermal conductivites within a reasonable range. These results are pretty consistent over five different heat configurations for both devices. Still, they only represent the optima closest to the initial supplier values. The parameters are very sensitive to small deviations in the steady state temperature. This comes along with high deviations in the ambient temperature of the controlled environment and, therefore, high sensitivity of the results to diode calibrations. Inverse modeling of specific heat values did not succeed. This can be due to too simplified models, but primarily to inproper inclusion of natural convection effects which have a major influence on simulation results. A big hurdle was temperature conditioning and measurement. It is a challenging task to provide a stable environment with a balanced temperature over the whole experimental setup and to measure it reliably within small ranges. Approaches only using radiative heating and a small measurement chamber could be more useful than approaches relying on convective transfer like commercial climate chambers.

The optimized models include many simplifications, like perfect contacts, planar interfaces, perfect solder joints and large simplifications in the PCB structure. Also, the influence of interfaces to heat transport is not included. These can have a significant impact on the thermal impedance, especially in compound materials that have many interfaces with a small overlap in the phonon density of states, like the encapsulation of the SiP package. As a consequence, these models cannot fully represent the thermal behavior of the device. Still, they help to identify the components most important for heat transport - namely the mold compound and the substrate, precautions to take for future finite elements simulations, and give a good first picture of heat transport within the devices. The heat flux in both devices is dominated by the path through die and die attach adhesive to the lead frame while heat conduction through the wire bonds plays a minor role for steady state temperatures.

For improvement of the thermal behavior of packages, experiments on different materials compositions would need to be done. Since packaging is not done in-house, this is a difficult task. Still, the focus of packaging technology goes increasingly towards gaining knowledge on materials properties, and thermal transport will become an increasingly important part of the game.

11 Appendix

11.1 Temperature Dependent Thermal Properties

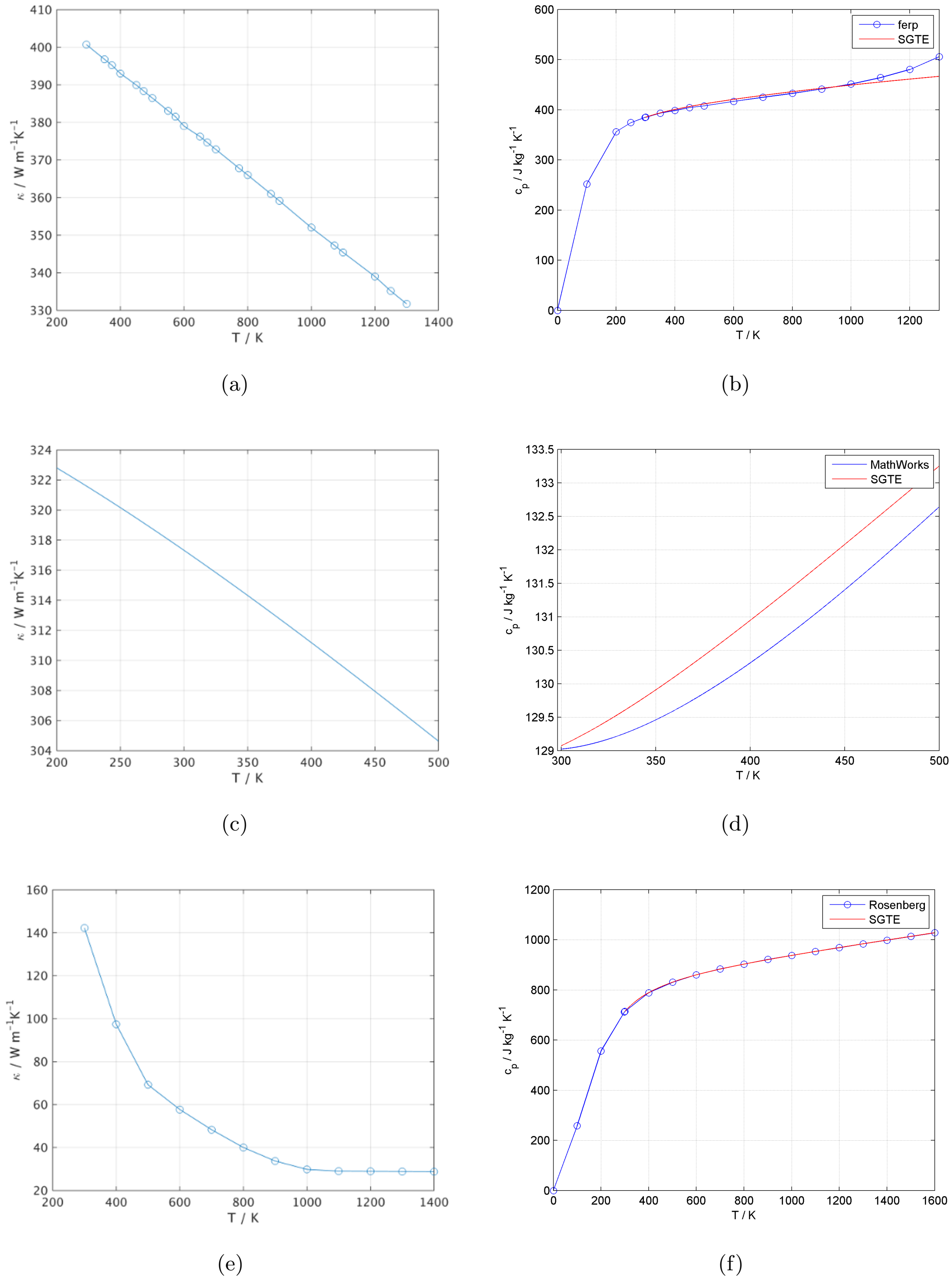

Figure 70: Temperature dependent thermal properties. Specific heat values out of literature and calculated values using SGTE values for the Gibbs energy [52]. (a) Cu thermal conductivity [36] (b) Cu specific heat [37] (c) Au thermal conductivity [35], (d) Au specific heat [35], (e) Si thermal conductivity [36] (f) Si specific heat [38]

11.2 Transient Response MatLab Code

The following code was written to calculate the integral difference for the specific heat optimization. The function ”curveintersect” used in line 61 was coded by Sebastian Hölz and can be found at MathWorks File Exchange.

```
1  function [out] = trapzsect(t,f,t0,f0,t_min,t_max)
2  % trapezoidal integral between two intersecting discrete
      functions with different lengths
3  % all input vectors are column vectors
4
5  t = t'; f = f'; t0 = t0'; f0 = f0';
6
7  if t_min > t(2) && t_max < t(end-1) && t_min > t0(2) && t_max <
      t0(end-1)
8      % set values below t_min and above t_max to 0. Interpolate
          function to t_min and t_max:
9      t_min_ind = t<=t_min;
10     t_edit_h = t(max(t_min_ind.*[1:numel(t)])+1);
11     t_edit_l = t(max(t_min_ind.*[1:numel(t)]));
12     t(t_min_ind) = 0;
13     t(max(t_min_ind.*[1:numel(t)])) = t_min;
14     t(max(t_min_ind.*[1:numel(t)])-1) = t_min-0.001*t_min;
15     f_edit_h = f(max(t_min_ind.*[1:numel(t)])+1);
16     f_edit_l = f(max(t_min_ind.*[1:numel(t)]));
17     f(t_min_ind) = 0;
18     f_low_val = f_edit_h-(f_edit_h-f_edit_l)/(t_edit_h-t_edit_l)
          *(t_edit_h-t_min);
19     f(max(t_min_ind.*[1:numel(t)])) = f_low_val;
20
21     t0_min_ind = t0<=t_min;
22     t0_edit_h = t0(max(t0_min_ind.*[1:numel(t0)])+1);
23     t0_edit_l = t0(max(t0_min_ind.*[1:numel(t0)]));
24     t0(t0_min_ind) = 0;
25     t0(max(t0_min_ind.*[1:numel(t0)])) = t_min;
26     t0(max(t0_min_ind.*[1:numel(t0)])-1) = t_min-0.001*t_min;
27     f0_edit_h = f0(max(t0_min_ind.*[1:numel(t0)])+1);
28     f0_edit_l = f0(max(t0_min_ind.*[1:numel(t0)]));
29     f0(t0_min_ind) = 0;
30     f0_low_val = f0_edit_h-(f0_edit_h-f0_edit_l)/(t0_edit_h-
          t0_edit_l)*(t0_edit_h-t_min);
31     f0(max(t0_min_ind.*[1:numel(t0)])) = f0_low_val;
32
33     t_max_ind = t>=t_max;
34     t_edit_l_ = t(max((t_max_ind-1)*(-1).*[1:numel(t)]));
```

```
35      t_edit_h_ = t(max((t_max_ind-1)*(-1).*[1:numel(t)])+1);
36      t(t_max_ind) = 0;
37      t(max((t_max_ind-1)*(-1).*[1:numel(t)])+1)= t_max;
38      t(max((t_max_ind-1)*(-1).*[1:numel(t)])+2) = t_max+0.001*
           t_min;
39      f_edit_l_ = f(max((t_max_ind-1)*(-1).*[1:numel(t)])+1);
40      f_edit_h_ = f(max((t_max_ind-1)*(-1).*[1:numel(t)])+2);
41      f(t_max_ind) = 0;
42      f_high_val = f_edit_l_+(f_edit_h_-f_edit_l_)/(t_edit_h_-
           t_edit_l_)*(t_edit_h_-t_max);
43      f(max((t_max_ind-1)*(-1).*[1:numel(t)])+1) = f_high_val;
44
45      t0_max_ind = t0>=t_max;
46      t0_edit_l_ = t0(max((t0_max_ind-1)*(-1).*[1:numel(t0)]));
47      t0_edit_h_ = t0(max((t0_max_ind-1)*(-1).*[1:numel(t0)])+1);
48      t0(t0_max_ind) = 0;
49      t0(max((t0_max_ind-1)*(-1).*[1:numel(t0)])+1)= t_max;
50      t0(max((t0_max_ind-1)*(-1).*[1:numel(t0)])+2) = t_max+0.001*
           t_min;
51      f0_edit_l_ = f0(max((t0_max_ind-1)*(-1).*[1:numel(t0)])+1);
52      f0_edit_h_ = f0(max((t0_max_ind-1)*(-1).*[1:numel(t0)])+2);
53      f0(t0_max_ind) = 0;
54      f0_high_val = f0_edit_l_+(f0_edit_h_-f0_edit_l_)/(t0_edit_h_-
           t0_edit_l_)*(t0_edit_h_-t_max);
55      f0(max((t0_max_ind-1)*(-1).*[1:numel(t0)])+1) = f0_high_val;
56  else
57      disp('WARNING: t_min too low and/or t_max too high. Whole
           time range taken. Please define t_min > t(2) resp. t0(2)
           and t_max < t(end-1) resp. t0(end-2)')
58  end
59
60  % find intersections:
61  [t_intsect,intsect] = curveintersect(t,f,t0,f0);
62
63  % find corresponding indizes below and above intersections (each
        row corresponds to one intersection):
64  t_intsect = t_intsect(intsect~=0);
65  intsect = intsect(intsect~=0);
66
67  exit_var = 0;
68  if isempty(intsect)
69      f_int = trapz(t,f);
70      f0_int = trapz(t0,f0);
```

```
71      out = sum(abs(f_int-f0_int));
72      exit_var = 1;
73  end
74
75  if exit_var == 0
76
77      % for f:
78  f_mat = repmat(f,numel(intsect),1);
79  f_intsect_mat = repmat(intsect,1,numel(f));
80  t_mat = repmat(t,numel(intsect),1);
81  t_intsect_mat = repmat(t_intsect,1,numel(f));
82  t_ind = abs(t_mat-t_intsect_mat)==repmat(min(abs(t_mat-
       t_intsect_mat),[],2),1,numel(t));
83
84  [row,s] = find(sum(t_ind,2)~=1);
85  [k,l] = find(t_ind(row,:)==1);
86  col = l(numel(l)/2+1:end);
87  for i=1:numel(row)
88      t_ind(row(i),col(i))=0;
89  end
90
91  t_close = t_mat(t_ind);
92  t_t_diff = t_close - t_intsect;
93  t_ind_low = t_ind;
94  t_ind_low(t_t_diff>0,:) = circshift(t_ind(t_t_diff>0,:),-1,2);
95  t_ind_high = circshift(t_ind_low,1,2);
96      % for f0:
97  f0_mat = repmat(f0,numel(intsect),1);
98  f0_intsect_mat = repmat(intsect,1,numel(f0));
99  t0_mat = repmat(t0,numel(intsect),1);
100 t0_intsect_mat = repmat(t_intsect,1,numel(f0));
101 t0_ind = abs(t0_mat-t0_intsect_mat)==repmat(min(abs(t0_mat-
       t0_intsect_mat),[],2),1,numel(t0));
102 t0_close = t0_mat(t0_ind);
103 t0_t_diff = t0_close - t_intsect;
104 t0_ind_low = t0_ind;
105 t0_ind_low(t0_t_diff>0,:) = circshift(t0_ind(t0_t_diff>0,:),-1,2)
       ;
106 t0_ind_high = circshift(t0_ind_low,1,2);
107
108 % trapezoidal integration:
109 f_n_vec = repmat([1:numel(f)],numel(intsect),1);
110 f_ind_low = f_n_vec(t_ind_low);
```

```
111 f_ind_high = f_ind_low+1;
112 f0_n_vec = repmat([1:numel(f0)],numel(intsect),1);
113 f0_ind_low = f0_n_vec(t0_ind_low);
114 f0_ind_high = f0_ind_low+1;
115     % integral residual of intersection time-frame:
116 f_resid_left = (t_intsect-t(f_ind_low)')/2.*(intsect+f(f_ind_low)
       ');
117 f_resid_right = (t(f_ind_high)'-t_intsect)/2.*(f(f_ind_high)'+
       intsect);
118 f0_resid_left = (t_intsect-t0(f0_ind_low)')/2.*(intsect+f0(
       f0_ind_low)');
119 f0_resid_right = (t0(f0_ind_high)'-t_intsect)/2.*(f0(f0_ind_high)
       '+intsect);
120     % integration:
121 f_int(1) = trapz(t(1,1:f_ind_low(1)),f(1,1:f_ind_low(1)))+
       f_resid_left(1);
122 f0_int(1) = trapz(t0(1,1:f0_ind_low(1)),f0(1,1:f0_ind_low(1)))+
       f0_resid_left(1);
123 if numel(intsect)>1
124     for i=2:numel(intsect)
125         t_f_ind_high = t(f_ind_high)';
126         t0_f0_ind_high = t0(f0_ind_high)';
127         if t_f_ind_high(i-1) > t_intsect(i)
128             f_int(i) = (t_intsect(i)-t_intsect(i-1))/2.*(intsect(
                   i)+intsect(i-1));
129         else
130             if numel(f_ind_high(i-1):f_ind_low(i))>1
131                 f_int(i) = f_resid_right(i-1)+trapz(t(1,
                       f_ind_high(i-1):f_ind_low(i)),f(1,f_ind_high(i
                       -1):f_ind_low(i)))+f_resid_left(i);
132             else
133                 f_int(i) = f_resid_right(i-1)+f_resid_left(i);
134             end
135         end
136         if t0_f0_ind_high(i-1) > t_intsect(i)
137             f0_int(i) = (t_intsect(i)-t_intsect(i-1))/2.*(intsect
                   (i)+intsect(i-1));
138         else
139             if numel(f0_ind_high(i-1):f0_ind_low(i))>1
140                 f0_int(i) = f0_resid_right(i-1)+trapz(t0(1,
                       f0_ind_high(i-1):f0_ind_low(i)),f0(1,
                       f0_ind_high(i-1):f0_ind_low(i)))+f0_resid_left(
                       i);
```

```
141                 else
142                     f0_int(i) = f0_resid_right(i-1)+f0_resid_left(i);
143                 end
144             end
145         end
146     end
147     f_int(numel(intsect)+1) = f_resid_right(numel(intsect))+trapz(t
        (1,f_ind_high(numel(intsect)):end),f(1,f_ind_high(numel(intsect
        )):end));
148     f0_int(numel(intsect)+1) = f0_resid_right(numel(intsect))+trapz(
        t0(1,f0_ind_high(numel(intsect)):end),f0(1,f0_ind_high(numel(
        intsect)):end));
149
150     % summation of sectionwise area difference:
151     out = sum(abs(f_int-f0_int));
152
153     end
154     end
```

11.3 Keithley®, Vötsch® TCP/IP Communication

The climate chamber and the SourceMeters were addressed via TCP/IP using the National Instruments VISA environment. It is important to address the climate chamber as socket. The function structure is shown as followed. The Keithley command list to define voltage and current levels, compliances and readings can be found in the manual. The Python version used is v2.7.

```
1   import visa
2   rm = visa.ResourceManager()
3   var_in = u'\xb6'
4
5   # the Voetsch climate chamber needs to be adressed via TCP/IP as
        socket (SOCKET). temp needs to be input as unicode u'27.0' in degC
        :
6
7   def set_temp(temp):
8       votsch = rm.open_resource('TCPIP::localhost::7777::SOCKET',
            read_termination='\r')
9       write_in = u'11001'+var_in+u'1'+var_in+u'1'+var_in+temp+u'\r'
10      votsch.write(write_in, encoding='utf-8')
11      out = votsch.read()
12      print 'set_temp success '+out
13      votsch.close()
14      return 'Temperature setpoint at '+temp+u"\u00b0"+'C'
15
```

```
16 def get_temp():
17     votsch = rm.open_resource('TCPIP::localhost::7777::SOCKET',
           read_termination='\r')
18     write_in = u'11004'+var_in+u'1'+var_in+u'1'+u'\r'
19     votsch.write(write_in, encoding='utf-8')
20     out = votsch.read_raw().decode('ascii', 'ignore')
21     temp_read = out[1:3]+'.'+out[4:len(out)-1]
22     votsch.close()
23     print 'Current temperature at '+out[1:3]+'.'+out[4:len(out)-1]+u"
           \u00b0"+'C'
24     return temp_read
25
26 # the Keithley sourcemeter needs to be adressed via TCP/IP as
       instrument (INSTR). vlvl needs to be set as string '1':
27
28 def set_vlvl(vlvl):
29     keithley = rm.open_resource('TCPIP0::129.27.158.84::inst0::INSTR'
           )
30     keithley.write('smua.source.levelv = '+vlvl)
31     keithley.close()
32     return 'Keithley voltage level now set to '+vlvl+' V'
```

References

[1] Andrea Chen and Randy Lo. *Semiconductor packaging: materials interaction and reliability.* Boca Raton, FL: CRC Press, 2012. 198 pp. ISBN: 978-1-4398-6205-6.

[2] Hong Xiao and Society of Photo-optical Instrumentation Engineers. *Introduction to semiconductor technology.* OCLC: 801513077. Bellingham, Wash. (1000 20th St. Bellingham WA 98225-6705 USA): SPIE, 2012. ISBN: 978-0-8194-9093-3 978-1-62870-104-3. URL: `http://search.ebscohost.com/login.aspx?direct=true&scope=site&db=nlebk&db=nlabk&AN=858277` (visited on 08/10/2016).

[3] P.S. Chauhan. *Copper Wire Bonding.* OCLC: 859364173. New York, NY: Springer New York, 2014. ISBN: 978-1-4614-5761-9. URL: `http://nbn-resolving.de/urn:nbn:de:1111-20130920918` (visited on 08/10/2016).

[4] "Semitracks Monthly Newsletter". In: (Sept. 2012).

[5] F. P. Incropera. *Fundamentals of heat and mass transfer.* OCLC: 948548336. S.l.: John Wiley, 2016. ISBN: 978-1-118-98917-3.

[6] Charles Kittel and Siegfried Hunklinger. *Einführung in die Festkörperphysik.* 15., unveränd. Aufl. OCLC: 828662738. München: Oldenbourg, 2013. 754 pp. ISBN: 978-3-486-59755-4.

[7] Marc J. Madou. *Fundamentals of microfabrication: the science of miniaturization.* 2nd ed. Boca Raton: CRC Press, 2002. 723 pp. ISBN: 978-0-8493-0826-0.

[8] Terry M Tritt. *Thermal Conductivity: Theory, Properties, and Applications.* OCLC: 517845564. Boston, MA: Kluwer Academic/Plenum Publishers, New York, 2004. ISBN: 978-0-387-26017-4. URL: `http://site.ebrary.com/id/10145369` (visited on 08/10/2016).

[9] J. M. Ziman. *Electrons and phonons: the theory of transport phenomena in solids.* Oxford classic texts in the physical sciences. Oxford : New York: Clarendon Press ; Oxford University Press, 2001. 554 pp. ISBN: 978-0-19-850779-6.

[10] Peter Hadley. "Advanced Solid State Physics". Graz University of Technology, 2015.

[11] Amelia Carolina Sparavigna. "The Boltzmann Equation Of Phonon Thermal Transport Solved In the Relaxation Time Approximation - II - Data Analysis". In: (2016). DOI: `10.13140/RG.2.1.2026.4724`. URL: `http://dx.doi.org/10.13140/RG.2.1.2026.4724` (visited on 08/16/2016).

[12] Daniel P. Sellan. "Predicting Phonon Transport In Semiconductor Nanostructures using atomistic Calculations and teh Boltzmann Transport Equation". PhD thesis. University of Toronto, 2012.

[13] Arpit Mittal. "Monte-Carlo Study of Phonon Heat Conduction in Silicon Thin Films". PhD thesis. Ohio State University, 2009.

[14] H. R. Shanks et al. "Thermal Conductivity of Silicon from 300 to 1400°K". In: *Physical Review* 130.5 (June 1, 1963), pp. 1743–1748. ISSN: 0031-899X. DOI: `10.1103/PhysRev.130.1743`. URL: `http://link.aps.org/doi/10.1103/PhysRev.130.1743` (visited on 10/11/2016).

[15] Oct. 2016. URL: `http://hypertextbook.com/facts/2004/JennelleBaptiste.shtml`.

[16] Jinlong Ma, Wu Li, and Xiaobing Luo. "Examining the Callaway model for lattice thermal conductivity". In: *Physical Review B* 90.3 (July 14, 2014). ISSN: 1098-0121, 1550-235X. DOI: 10.1103/PhysRevB.90.035203. URL: http://link.aps.org/doi/10.1103/PhysRevB.90.035203 (visited on 08/10/2016).

[17] J. R. Hook, H. E. Hall, and H. E. Hall. *Solid state physics*. 2nd ed. The Manchester physics series. Chichester ; New York: Wiley, 1991. 474 pp. ISBN: 978-0-471-92804-1 978-0-471-92805-8.

[18] Tianli Feng and Xiulin Ruan. "Quantum mechanical prediction of four-phonon scattering rates and reduced thermal conductivity of solids". In: *Physical Review B* 93.4 (Jan. 6, 2016). ISSN: 2469-9950, 2469-9969. DOI: 10.1103/PhysRevB.93.045202. URL: http://link.aps.org/doi/10.1103/PhysRevB.93.045202 (visited on 10/11/2016).

[19] A. A. Maznev and O. B. Wright. "Demystifying umklapp vs normal scattering in lattice thermal conductivity". In: *American Journal of Physics* 82.11 (Nov. 2014), pp. 1062–1066. ISSN: 0002-9505, 1943-2909. DOI: 10.1119/1.4892612. URL: http://scitation.aip.org/content/aapt/journal/ajp/82/11/10.1119/1.4892612 (visited on 08/10/2016).

[20] E. T. Swartz and R. O. Pohl. "Thermal boundary resistance". In: *Reviews of Modern Physics* 61.3 (July 1, 1989), pp. 605–668. ISSN: 0034-6861. DOI: 10.1103/RevModPhys.61.605. URL: http://link.aps.org/doi/10.1103/RevModPhys.61.605 (visited on 08/10/2016).

[21] John C. Duda et al. "On the Assumption of Detailed Balance in Prediction of Diffusive Transmission Probability During Interfacial Transport". In: *Nanoscale and Microscale Thermophysical Engineering* 14.1 (Mar. 12, 2010), pp. 21–33. ISSN: 1556-7265, 1556-7273. DOI: 10.1080/15567260903530379. URL: http://www.tandfonline.com/doi/abs/10.1080/15567260903530379 (visited on 08/11/2016).

[22] Ganesh Balasubramanian and Ishwar K. Puri. "Heat conduction across a solid-solid interface: Understanding nanoscale interfacial effects on thermal resistance". In: *Applied Physics Letters* 99.1 (2011), p. 013116. ISSN: 00036951. DOI: 10.1063/1.3607477. URL: http://scitation.aip.org/content/aip/journal/apl/99/1/10.1063/1.3607477 (visited on 08/10/2016).

[23] Nuo Yang et al. "Thermal Interface Conductance Between Aluminum and Silicon by Molecular Dynamics Simulations". In: *Journal of Computational and Theoretical Nanoscience* 12.2 (Feb. 1, 2015), pp. 168–174. ISSN: 15461955, 15461963. DOI: 10.1166/jctn.2015.3710. URL: http://openurl.ingenta.com/content/xref?genre=article&issn=1546-1955&volume=12&issue=2&spage=168 (visited on 08/10/2016).

[24] Ho-Ki Lyeo and David G. Cahill. "Thermal conductance of interfaces between highly dissimilar materials". In: *Physical Review B* 73.14 (Apr. 3, 2006). ISSN: 1098-0121, 1550-235X. DOI: 10.1103/PhysRevB.73.144301. URL: http://link.aps.org/doi/10.1103/PhysRevB.73.144301 (visited on 08/10/2016).

[25] Ashutosh Giri et al. "Reduction in thermal conductivity and tunable heat capacity of inorganic/organic hybrid superlattices". In: *Physical Review B* 93.2 (Jan. 11, 2016). ISSN: 2469-9950, 2469-9969. DOI: 10.1103/PhysRevB.93.024201. URL: http://link.aps.org/doi/10.1103/PhysRevB.93.024201 (visited on 08/10/2016).

[26] Keij Fukushima, Yoshitaka Takezawa, and Tadafumi Adschiri. "Evaluation of Thermal Conductive Resistance at Organic–Inorganic Interface and Effect of Interfaces on Thermal Conductivity of Composite Materials". In: *Japanese Journal of Applied Physics* 52.8 (2013), p. 081601. URL: http://stacks.iop.org/1347-4065/52/i=8R/a=081601.

[27] Uri Lachish. *Thermoelectric Effect Peltier Seebeck and Thomson*. 2016. URL: http://urila.tripod.com/Thermoelectric.pdf.

[28] D. W. van Krevelen and K. te Nijenhuis. *Properties of polymers: their correlation with chemical structure: their numerical estimation and prediction from additive group contributions*. 4th, completely rev. ed. Amsterdam: Elsevier, 2009. 1004 pp. ISBN: 978-0-08-054819-7.

[29] M. O. Alam and C. Bailey, eds. *Advanced adhesives in electronics: materials, properties and applications*. Woodhead publishing in materials. OCLC: 743645602. Oxford: Woodhead Publ, 2011. 268 pp. ISBN: 978-1-84569-576-7 978-0-85709-289-2.

[30] Mou Kehn Malcolm Ng. "Computational Electromagnetics". National Chiao Tung University, Hsinchu, Taiwan, 2014.

[31] July 2016. URL: http://mathworld.wolfram.com/LagrangeInterpolatingPolynomial.html.

[32] Jian-Ming Jin. *The finite element method in electromagnetics*. Third edition. Hoboken. New Jersey: John Wiley & Sons Inc, 2014. 846 pp. ISBN: 978-1-118-57136-1.

[33] John Leonidas Volakis, A. Chatterjee, and Leo C. Kempel. *Finite element method for electromagnetics: antennas, microwave circuits, and scattering applications*. New York: IEEE Press, 1998. 344 pp. ISBN: 978-0-7803-3425-0.

[34] Peter Hadley. "Physics of Semiconductor Devices". Graz University of Technology, 2015.

[35] Inc. MathWorks. *COMSOL Multiphysics incl. Heat Transfer Module*. Version 5.2.

[36] *NIST-JANAF Thermochemical Tables*. Aug. 2015. URL: http://kinetics.nist.gov/janaf.

[37] Aug. 2015. URL: http://www-ferp.ucsd.edu/LIB/PROPS/PANOS/cu.html.

[38] H M Rosenberg. "The Thermal Conductivity of Germanium and Silicon at Low Temperatures". In: *Proceedings of the Physical Society. Section A* 67.9 (Sept. 1, 1954), pp. 837–840. ISSN: 0370-1298. DOI: 10.1088/0370-1298/67/9/312. URL: http://stacks.iop.org/0370-1298/67/i=9/a=312?key=crossref.9f2613f069bd785eb528b674b6a6bfa8 (visited on 08/11/2016).

[39] Jan. 2016. URL: http://www.makeitfrom.com/material-properties/Liquid-Crystal-Polymer-LCP.

[40] Jan. 2016. URL: http://www.msed.nist.gov/solder/NIST_LeadfreeSolder_v4.pdf.

[41] Jan. 2016. URL: http://www.neeinternational.com/pdf/NEE_app_note0908.pdf.

[42] K. Azar and J.E. Graebner. "Experimental determination of thermal conductivity of printed wiring boards". In: IEEE, 1996, pp. 169–182. ISBN: 978-0-7803-3139-6. DOI: 10.1109/STHERM.1996.545107. URL: http://ieeexplore.ieee.org/lpdocs/epic03/wrapper.htm?arnumber=545107 (visited on 08/11/2016).

[43] July 2016. URL: http://www.excellence-in-insulation.eu/site/fileadmin/user_upload/PDF/Thermal_insulation_materials_made_of_rigid_polyurethane_foam.pdf.

[44] U Jarfelt. "Thermal conductivity of polyurethan foam - best performance". 10th international symposium on District Heating and Cooling. Göteborg, 2006, Jan. 2006.

[45] J. Murphy. "Long Term Aging of Closed-Cell Foam Insulation". Foam Supplies, Inc., Houston, 2010.

[46] M. Thirumal et al. "Effect of foam density on the properties of water blown rigid polyurethane foam". In: *Journal of Applied Polymer Science* 108.3 (May 5, 2008), pp. 1810–1817. ISSN: 00218995, 10974628. DOI: 10.1002/app.27712. URL: http://doi.wiley.com/10.1002/app.27712 (visited on 08/11/2016).

[47] Bernhard Schrader and D. Bougeard, eds. *Infrared and Raman spectroscopy: methods and applications*. Weinheim ; New York: VCH, 1995. 787 pp. ISBN: 978-3-527-26446-9.

[48] Satyaprakash Sahoo et al. "Temperature-Dependent Raman Studies and Thermal Conductivity of Few-Layer MoS $_2$". In: *The Journal of Physical Chemistry C* 117.17 (May 2, 2013), pp. 9042–9047. ISSN: 1932-7447, 1932-7455. DOI: 10.1021/jp402509w. URL: http://pubs.acs.org/doi/abs/10.1021/jp402509w (visited on 08/11/2016).

[49] D S Moore and S D McGrane. "Raman temperature measurement". In: *Journal of Physics: Conference Series* 500.19 (May 7, 2014), p. 192011. ISSN: 1742-6596. DOI: 10.1088/1742-6596/500/19/192011. URL: http://stacks.iop.org/1742-6596/500/i=19/a=192011?key=crossref.b673b1a245e6f13a05b933d413f9fc3c (visited on 08/11/2016).

[50] V. Szekely and M. Rencz. "Thermal dynamics and the time constant domain". In: *IEEE Transactions on Components and Packaging Technologies* 23.3 (Sept. 2000), pp. 587–594. ISSN: 15213331. DOI: 10.1109/6144.868862. URL: http://ieeexplore.ieee.org/lpdocs/epic03/wrapper.htm?arnumber=868862 (visited on 08/11/2016).

[51] Vladimir Székely and Tran Van Bien. "Fine structure of heat flow path in semiconductor devices: A measurement and identification method". In: *Solid-State Electronics* 31.9 (Sept. 1988), pp. 1363–1368. ISSN: 00381101. DOI: 10.1016/0038-1101(88)90099-8. URL: http://linkinghub.elsevier.com/retrieve/pii/0038110188900998 (visited on 08/11/2016).

[52] A.T. Dinsdale. "SGTE data for pure elements". In: *Calphad* 15.4 (Oct. 1991), pp. 317–425. ISSN: 03645916. DOI: 10.1016/0364-5916(91)90030-N. URL: http://linkinghub.elsevier.com/retrieve/pii/036459169190030N (visited on 11/30/2016).

[53] David G. Cahill et al. "Nanoscale thermal transport". In: *Journal of Applied Physics* 93.2 (2003), p. 793. ISSN: 00218979. DOI: 10.1063/1.1524305. URL: http://scitation.aip.org/content/aip/journal/jap/93/2/10.1063/1.1524305 (visited on 08/10/2016).

[54] Patrick E. Hopkins. "Thermal Transport across Solid Interfaces with Nanoscale Imperfections: Effects of Roughness, Disorder, Dislocations, and Bonding on Thermal Boundary Conductance". In: *ISRN Mechanical Engineering* 2013 (2013), pp. 1–19. ISSN: 2090-5130. DOI: 10.1155/2013/682586. URL: http://www.hindawi.com/journals/isrn/2013/682586/ (visited on 08/10/2016).

[55] Guosheng Jiang, Liyong Diao, and Ken Kuang. *Advanced thermal management materials.* OCLC: ocn818786114. New York: Springer, 2013. 154 pp. ISBN: 978-1-4614-1962-4 978-1-4614-1963-1.

[56] Willy M. C. Sansen. *Analog design essentials.* OCLC: ocm65166635. Dordrecht, The Netherlands: Springer, 2006. 777 pp. ISBN: 978-0-387-25746-4.

[57] Behzad Razavi. *Design of analog CMOS integrated circuits.* International ed., [Nachdr.] McGraw-Hill series in electrical and computer engineering. OCLC: 846074136. Boston: McGraw-Hill, 2010. 684 pp. ISBN: 978-0-07-118839-5 978-0-07-118815-9.

[58] Kouichi Tanaka et al. "A molecular dynamics study on thermal conductivity of thin epoxy polymer sandwiched between alumina fillers in heat-dissipation composite material". In: *International Journal of Heat and Mass Transfer* 89 (Oct. 2015), pp. 714–723. ISSN: 00179310. DOI: 10.1016/j.ijheatmasstransfer.2015.05.080. URL: http://linkinghub.elsevier.com/retrieve/pii/S0017931015005748 (visited on 08/10/2016).

[59] James Hone. "Phonons and Thermal Properties of Carbon Nanotubes". In: *Carbon Nanotubes.* Ed. by Mildred S. Dresselhaus, Gene Dresselhaus, and Phaedon Avouris. Vol. 80. Berlin, Heidelberg: Springer Berlin Heidelberg, 2001, pp. 273–286. ISBN: 978-3-540-41086-7. URL: http://link.springer.com/10.1007/3-540-39947-X_11 (visited on 08/11/2016).

[60] Vladimir Székely and Albin Szalai. "Measurement of the time-constant spectrum: Systematic errors, correction". In: *Microelectronics Journal* 43.11 (Nov. 2012), pp. 904–907. ISSN: 00262692. DOI: 10.1016/j.mejo.2012.05.011. URL: http://linkinghub.elsevier.com/retrieve/pii/S0026269212001218 (visited on 08/11/2016).

[61] V. Szekely. "On the representation of infinite-length distributed RC one-ports". In: *IEEE Transactions on Circuits and Systems* 38.7 (July 1991), pp. 711–719. ISSN: 00984094. DOI: 10.1109/31.135743. URL: http://ieeexplore.ieee.org/lpdocs/epic03/wrapper.htm?arnumber=135743 (visited on 08/11/2016).

[62] Junwei Yang et al. "Thermal time-constant spectrum extraction method in AlGaN/GaN HEMTs". In: *Journal of Semiconductors* 36.8 (Aug. 2015), p. 084003. ISSN: 1674-4926. DOI: 10.1088/1674-4926/36/8/084003. URL: http://stacks.iop.org/1674-4926/36/i=8/a=084003?key=crossref.ae68fb3334b4394bda214b2d6ab6eb81 (visited on 08/11/2016).